STUDY OF CATION-DOMINATED IONIC-ELECTRONIC MATERIALS AND DEVICES

A DISSERTATION

PRESENTED TO

THE ACADEMIC FACULTY

BY

JORDAN D. GREENLEE

IN PARTIAL FULFILLMENT

OF THE REQUIREMENTS FOR THE DEGREE

DOCTOR OF PHILOSOPHY

SCHOOL OF ELECTRICAL AND COMPUTER ENGINEERING

GEORGIA INSTITUTE OF TECHNOLOGY

MAY 2014

Study of Cation-Dominated Ionic-Electronic Materials and Devices

Dr. W. Alan Doolittle
School of Electrical and Computer Engineering
Georgia Institute of Technology

Dr. A. Bruno Frazier
School of Electrical and Computer Engineering
Georgia Institute of Technology

Dr. Oliver Brand
School of Electrical and Computer Engineering
Georgia Institute of Technology

Dr. Faisal Alamgir
School of Materials Science and Engineering
Georgia Institute of Technology

Dr. William Hunt
School of Electrical and Computer Engineering
Georgia Institute of Technology

Date Approved: December 2013

To Cara, my parents, and my sister.

You have always been there for me.

You have supported, guided, and inspired me more than you will ever know.

ACKNOWLEDGEMENTS

First and foremost, I would like to thank my family for their unconditional love and support. My grandparents, mother, and father have all fostered my interest in math and science. Mom, I still remember when you sat me down after I earned a bag grade in spelling. You told me that as long as I got A's in my math and science classes, I'd be just fine. Dad, you always were my biggest fan at my soccer games and chess matches growing up. I know that will never change and I appreciate that so much. Sis, you're a source of inspiration for me, and I can always look to you to lift my spirits if I'm down. Cara, you have been the definition of a best friend - a constant source of encouragement, support, and inspiration throughout my PhD career. Without my family's love and support, I would not be where I am today.

I owe my thesis advisor, Dr. W. Alan Doolittle, a huge thank you for the time and effort he has put into my education. Without your support and constructive conversations, I would not be the scientist I am today. I also would like to especially thank Dr. Faisal Alamgir for his guidance and support.

I consider myself extremely lucky for the opportunity to work with some of the best scientists and engineers including Laws Calley, Josh Shank, Brendan Gunning, Brooks Tellekamp, Michael Moseley, Chloe Fabien, Jonathan Lowder, Daniel Billingsley, Cole Petersburg, and James Compagnoni.

I would like to thank my thesis committee for their guidance throughout my thesis defense. Finally, the NRC staff has been extremely helpful throughout my research, especially Gary Spinner, Jason Herrington, Claude Rooney, and Charlie Suh.

Table of Contents

List of Tables

List of Figures

List of Nomenclature

Å	Angstrom (10^{-10} meter)
ρ	resistivity
σ	conductivity
Ω	Ohm
μ	carrier mobility
μm	micron (10^{-6} meter)
AFM	atomic-force microscopy
Al	aluminum
Au	gold
C-V	capacitance-voltage
CCG	Cold Cathode Gauge
Cu	copper
DI	deionized
Eg	band gap energy
EIS	electrochemical impedance spectroscopy
eV	electron volt
FWHM	full width at half maximum
H2SO4	sulfuric acid
H2O2	hydrogen peroxide
HF	hydrofluoric acid
LD	laser diode
Li	lithium
$LiNbO_2$	lithium niobite
$LiNbO_3$	lithium niobate
LPEE	Liquid Phase Electro-Epitaxy
MBE	molecular-beam epitaxy
Nb	niobium
Ni	nickel
RF	Radio Frequency
TCE	Trichloroethylene

Summary

The memristor is a two-terminal semiconductor device that is able to mimic the conductance response of synapses and can be utilized in next-generation computing platforms that will compute similarly to the mammalian brain. The initial memristor implementation is operated by the digital formation and dissolution of a highly conductive filament. However, an analog memristor is necessary to mimic analog synapses in the mammalian brain. To understand the mechanisms of operation and impact of different device designs, analog memristors were fabricated, modeled, and characterized. To realize analog memristors, lithiated transition metal oxides were grown by molecular beam epitaxy, RF sputtering, and liquid phase electro-epitaxy. Analog memristors were modeled using a finite element model simulation and characterized with X-ray absorption spectroscopy, impedance spectroscopy, and other electrical methods. It was shown that lithium movement facilitates analog memristance and nanoscopic ionic-electronic memristors with ion-soluble electrodes can be key enabling devices for brain-inspired computing.

CHAPTER 1: INTRODUCTION

For decades, the realization of Moore's law has been the driving force behind the digital era, with transistors shrinking at an astounding rate. However, many experts are now predicting that present-day computing devices will soon begin to approach performance limits due to excess heat and power consumption [1-3]. In fact, the International Technology Roadmap for Semiconductors (ITRS) has recently produced a white paper that calls for a change of the reliance on Moore's law for future computational advancement [4]. The ITRS argues that more capable devices are needed for computational advancement instead of purely expanding the number of transistors per unit area.

The discovery of a new semiconductor device, the memristor, could provide the capability needed for the advancement of computing. Because memristors are able to mimic the conductance response of synapses, they can be utilized in next-generation computation platforms that seek to compute similar to the mammalian brain. Despite being originally theorized by Chua in 1971 [5], the implementation of the memristor was not claimed until 2008 by HP labs [6].

The initial realization of a memristor consisted of a metal – oxide – metal structure where a highly conductive filament is formed and dissolved in the oxide. This filament, when formed, essentially shorts the metal contacts, the 'on' state, to dramatically decrease resistance. When the filament is dissolved, producing the 'off' state, the normal conductivity of the insulating oxide dominates the resistance of the device. While this digital mode of operation may be desirable in certain applications such as digital memory and digital logic, for neuromorphic computing applications, an

analog memristor is necessary to mimic the analog synapses in the mammalian brain. In this work, a new type of memristor that exhibits an analog response and does not rely on filamentary conduction is investigated. Like synapses in the brain, $LiNbO_2$-based analog memristors either exhibit an increase or decrease in resistance as a function of previously applied inputs to the device. An analog implementation of the memristor based on the sub-oxide $LiNbO_2$ can mimic both excitatory and inhibitory behavior in which resistance decreases/increases respectively with the applied stimulus time [7]. This complementary synaptic behavior is due to the ability to produce both n and p-type $LiNbO_2$ material, an uncommon property for semiconducting oxides. N-type memristors are fabricated with a near-stoichiometric level of lithium and are oxygen deficient creating an excess of donors. P-type memristors are grown with near stoichiometric oxygen content and are lithium deficient resulting in a surfeit of acceptors.

The aim of this work is to investigate novel memristive materials dominated by the movement of lithium ions in the crystalline lattice. This investigation involves the characterization of cation-based memristors and other associated devices. Additionally, to realize these memristive devices, the growth of lithiated transition metal oxides is explored. The advancements in the understanding of lithium-intercalated materials could enable key devices for future computational architectures based on mammalian brain-inspired computation.

1.1 Memristors

Originally theorized by Chua [5] as the missing 4th circuit element, the memristor relates magnetic flux to electric charge as shown in Figure 1.1. The first solid-state implementation classified as a memristor was developed at HP Labs [6] whereby a TiO_2 film was deposited between two platinum electrodes. Before this development, multiple two-terminal resistive switching devices based on metal oxides were discovered [8-16] but the connection of these devices to the memristor was not recognized. The TiO_2-based and related resistive switching devices operate in a digital regime, with a sudden change in resistance due to the formation and destruction of highly conductive filaments [17-20].

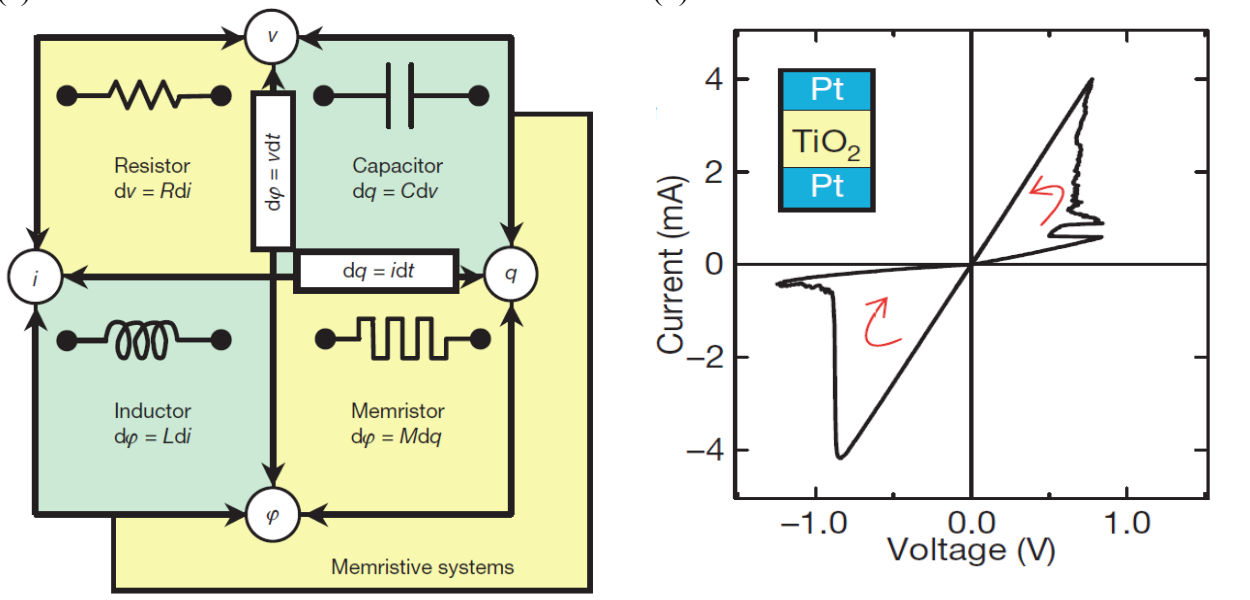

Figure 1.1: (a) The four fundamental 2-terminal devices and the fundamental relations between them (b) TiO_2-based memristor I-V curve [6].

Recent implementations of memristors [12] have depended on filamentary conduction paths to generate a digital change in resistance. The characteristic I-V curve of these filamentary memristors is shown in Figure 1.1. While this technology may have applications in digital memory, it is not ideal for neuromorphic computing, where a more gradual (analog) change in resistance is required in order to replicate the conductance response of synapses in the mammalian brain. Neuromorphic computing is a proposed next-generation computing solution to replace present-day computing devices which will soon begin to approach performance limits due to excess heat and power consumption [1]. In neuromorphic computing, calculations are performed using low-powered electrical devices inspired by biological neurons and synapses [21-23]. $LiNbO_2$-based memristors have a truly analog nature making them an ideal candidate for use as synapses in neuromorphic circuits. This analog nature also makes $LiNbO_2$-based memristors a natural fit to mimic ionic channels in the Hodgkin and Huxley model of the axon [24, 25]. Additionally, a recovery of the original resistance is observed after each period of the sinusoidal input despite the $LiNbO_2$-based memristor geometry being orders of magnitude larger in size than filament-based memristors.

This recovery of original resistance is a direct consequence of the mechanism used to change the resistance of the device - the drift of lithium atoms. This is a well-documented phenomenon in materials with similar structural characteristics to lithium niobite [26]. The lithium vacancies generated by the drift of lithium act as acceptors, so as lithium is moved through the memristor, areas of high and low resistances are formed.

Lithium niobite, $LiNbO_2$, is a suboxide of the more prevalent lithium niobate, $LiNbO_3$, and was originally investigated for its superconducting properties [27-38]. It

has also been investigated for potential applications as a battery cathode [29]. $LiNbO_2$ has a layered lithium-intercalated structure much like commercial lithium ion battery cathode materials that facilitates the rapid movement of lithium and its usefulness as a battery and memristive material [39, 40].

To date, lithium niobite has been synthesized three different ways. First, solid state reactions between Li_2CO_3, Li_3NbO_4, Nb_2O_5, and Nb have produced single-phase $LiNbO_2$ [38]. In this solid state reaction, NbO was obtained by mixing stoichiometric amounts of Nb_2O_5 and Nb in an evacuated quartz tube and heating it for 70 hours at 1100° C. Li_3NbO_4 was produced by mixing Li_2CO_3 and Nb_2O_5 in an alumina crucible at 900° C for 50 hours. The two precursors produced, Li_3NbO_4 and Nb_2O_5, were then mixed and heated at 1050° C for 50 hours in an evacuated quartz crucible to produce $LiNbO_2$ [38].

A second route to the growth of $LiNbO_2$ is via a mix of $LiBO_2$, $NaBO_2$, LiF, and Nb_2O_5 [35]. After mixing, the powder constituents are placed in a graphite crucible and melted. After the growth constituents are melted, ions in the melt are deposited electrically.

Finally, thin films of crystalline $LiNbO_2$ have been grown by molecular beam epitaxy using an oxy-halide growth chemistry [39]. For the growth of $LiNbO_2$, lithium combines with niobium (V) chloride and oxygen in the correct ratios to produce the desired phase. Lithium is used to getter the Cl and forms LiCl which subsequently desorbs from the growth surface at elevated growth temperatures (above 800° C). Unfortunately, this growth chemistry is not as straightforward as traditional materials grown by molecular beam epitaxy such as GaAs which is a line compound. As shown in

Table 1.1, there exist multiple reactions in this growth chemistry, many of which are energetically favorable. Depending on which of these many reactions occur, multiple phases composed of species with different oxidation states can be grown using the same precursors. Achievable phases using the metal halide growth chemistry include Nb_2O_5, NbO_2, NbO, Li_3NbO_4, $LiNb_3O_8$, and $LiNbO_3$.

The fully-oxidized phase diagram for the Nb_2O_5 + Li_2O system is shown in Figure 1.2. Even for the fully oxidized system there is a narrow range at 900 °C to grow pure single phase $LiNbO_3$. An error of just 1% in growth precursor delivery will result in the growth of a mixed phase instead of single phase $LiNbO_3$. Unfortunately, a phase diagram that includes sub-oxides does not exist for this system, but the precision necessary to obtain a single phase in the fully-oxidized system is an indication of the challenge associated with growing single phase material in the Li + Nb + O material system.

Table 1.1: Gibbs free energy change of halide-based $LiNbO_2$ growth reactions [39].

Reaction	ΔG at 900° C (kJ)
$NbCl_5(g)=Nb+2.5Cl_2(g)$	487
$NbCl_5(g)= NbCl_4(g)+0.5Cl_2(g)$	70
$NbCl_5(g)= NbCl_3(g)+Cl_2(g)$	380
$2NbCl_5(g)+2.5O_2(g)= Nb_2O_5+5Cl_2(g)$	-416
$2NbCl_5(g)+ 5O_2(g)= Nb_2O_5+5Cl_2(g)$	-1298
$10Li(g)+ 5Cl_2(g)= 10LiCl(g)$	-3610
$2NbCl_5(g)+10Li(g)+2.5O_2(g)= Nb_2O_5+10LiCl(g)$	-4025
$2NbCl_5(g)+10Li(g)+ 5O(g)= Nb_2O_5+10LiCl(g)$	-4908
$10Li(g)+ 2NbCl_5(g)=2Nb+10LiCl(g)$	-2114
$4LiCl+ O_2(g)=2Li_2O+2Cl_2(g)$	395
$4LiCl+ 2O(g)=2Li_2O+2Cl_2(g)$	-42
20Li+10NbO=10Li2O+10Nb	-1295
$20Li+5NbO_2$=10Li2O+5Nb	-1512
$20Li+2Nb_2O_5$=10Li2O+5Nb	-1651

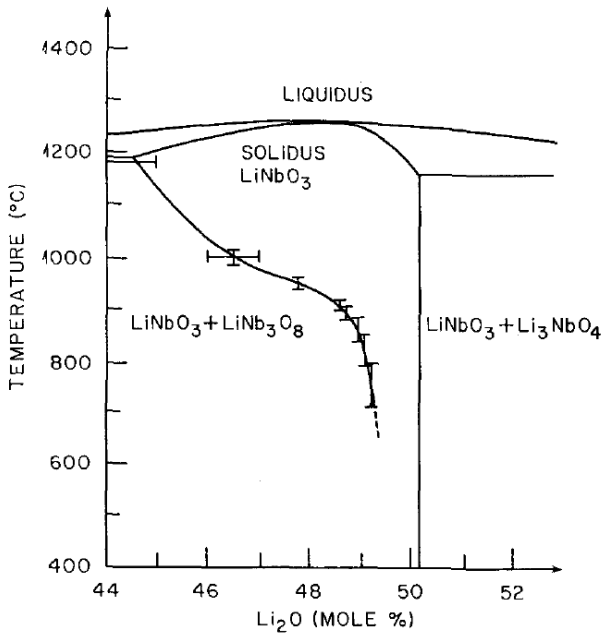

Figure 1.2: Phase diagram of the existence of $LiNbO_3$ using Li_2O and Nb_2O_5 [41].

1.2 Significant Memristive Devices

Filamentary Digital Memristor

The first memristor implementation claimed was the HP Labs digital resistive switch which consists of a TiO_2 layer deposited between two Pt electrodes [6]. However, this memristive response is not unique to TiO_2 since many devices/materials have exhibited digital memristive behavior [10, 12, 14, 15, 17, 42-45]. The HP device is representative of most of the digital memristors in the literature and has two stable states which will be referred to as the conductive and insulating states. The present state of the device is determined by the previous inputs to the device in a limited sense. Unlike the memristor proposed by Chua, the present state of the memristor is not dependent on the entire integrated current history of the device. It is necessary to qualify the previous statement with a brief physical explanation of the digital memristor. The change of resistance in the device is facilitated by the formation of conductive filaments made of

Ti_nO_{2n-1} magnéli phases where n=4 or 5 [46] that form due to oxygen dopant drift [20, 47]. During the electroforming cycle wherein the filaments are created via a current limited breakdown, a dramatic increase occurs, which greatly enhances dopant drift [48, 49]. This oxygen drift can even damage the memristor contacts[50]. Evidence for the creation of filamentary conduction paths has been confirmed using high-resolution transmission electron microscopy [20], concurrent spatially-resolved x-ray absorption and electron diffraction [51], and conductive atomic force microscopy [52] among other methods.

The relevance of the physical operation of these digital memristors to the suggestion that these filament-based devices do not constitute a complete implementation of the original Chua-proposed memristor is based on the assertion that only a partial history of the current voltage characteristic affects the resistance. Consider the case where the digital memristor is in its high-resistance, insulating, state. If a bias is applied that drifts oxygen dopants to form a conductive filament, the resistance changes quickly to the conductive state. Next, if a bias is applied with the same polarity as the previous case, the resistance does not change significantly, since a filament has already formed and thus the resistance of the memristor would remain in the conductive state. In this second application of a bias, the resistance state has not changed. Therefore, the present state of a digital memristor is a function of a limited history of inputs to the device. Additional material systems have exhibited the same resistive switching behavior used to describe the digital memristor including ZrO_2 [53], $Pr_{.7}Ca_{.3}MnO_3$ [9], NiO [54], Nb_2O_5 [10], CeO_x [42], $SrTiO_x$ [45], Al_2O_3 [43], Ta_2O_5 [44], $SrZrO_3$ [10]. Because of the digital

nature of the filament-based resistive switch memristors, they are well-suited to digital logic [55, 56], digital memory [57], and reconfigurable circuit applications [58].

Ag/Si Graded Memristor

An analog memristor based on a mechanism similar to the filamentary resistive switch has been developed as shown in Figure 1.3 [59]. This analog memristor uses Ag particles co-sputtered with Si in a graded alloy and, just like the resistive switching devices, the metal/insulator transition is controlled with an applied bias. However, unlike the filamentary resistive switching memristor, a gradual resistance change is facilitated by the graded Ag doping, and a conduction front is formed instead of single conducting filaments. The Ag/Si analog memristor has demonstrated the ability to replicate basic synaptic functionality, suggesting that it as well as all of the analog memristors mentioned below, can be used in neuromorphic computing applications [59].

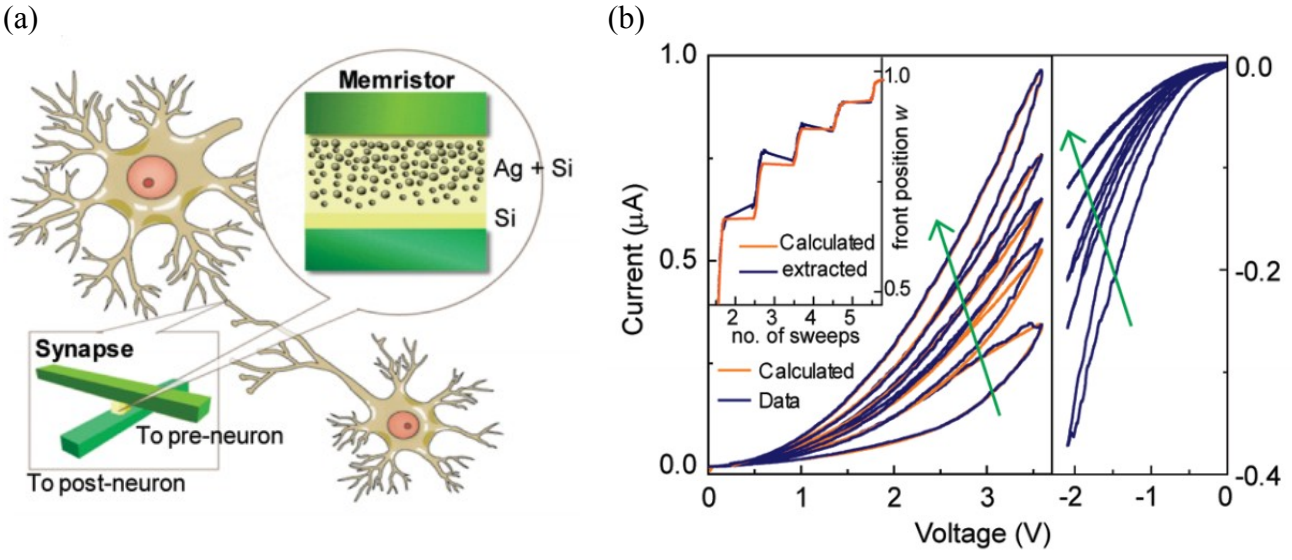

Figure 1.3: (a) Schematic of an Ag/Si graded memristor and corresponding (b) I-V curve [59].

Spintronic Memristor

Another solid-state analog memristor based on a semiconductor - ferromagnetic junction has been proposed and modeled [60, 61]. The junction allows electrons of one polarity of spin to enter the ferromagnetic layer while the opposite spin electrons are blocked. This blockage produces a cloud of electrons with the spin polarity that is blocked. As the applied voltage is increased, the current through the junction saturates as the electrons with a polarity that allows them to pass through the junction are blocked by the cloud of electrons with the blocking spin. Thus, the conductivity of the device is a function of the current that has previously passed through the device. The implementation of a viable spintronic memristor has been limited by the availability of suitable materials.

Organic Ionic-Electronic Memristor

An organic implementation of an analog memristor has also been demonstrated as shown in Figure 1.4 [62, 63]. A layer of polyaniline is reversibly modulated between an insulating reduced state and a conductive oxidized state which has been confirmed in both temporally and spatially using spatially-resolved Raman scattering [64]. The electrically active polyanaline layer is reversibly doped using either Li or Rb ions. In order to monitor both electronic and ionic currents, the device has three terminals, but two of the terminals are connected to ground. Thus, the device can ultimately be implemented with two terminals. The three terminal nature of the organic memristor was used to demonstrate the relationship between measured charge transfer and conductivity variation.

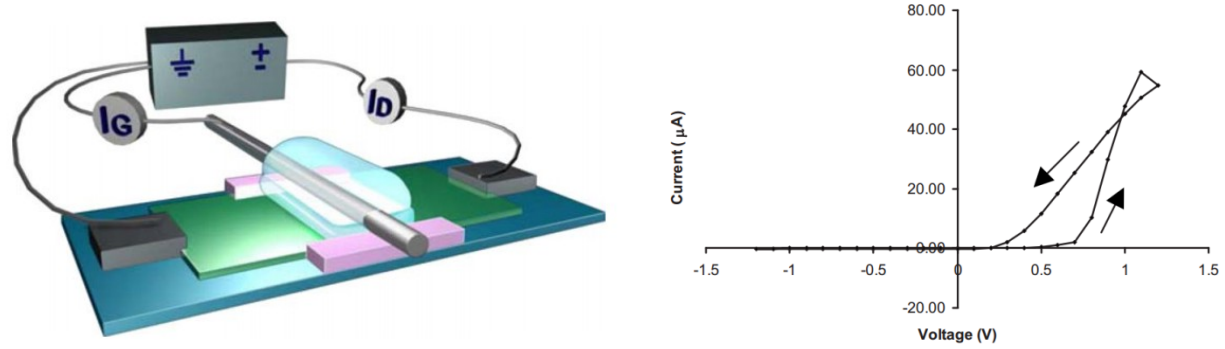

Figure 1.4: Schematic of an inorganic analog memistor (a) and corresponding I-V curve (b) [63].

Inorganic Ionic-Electronic Memristor

Another analog memristor based on dopant drift and diffusion was theorized in 1974 as an electrolytic cell with electrodes that effect the concentration of the electrolyte [65]. The cell appears as a resistor whose resistance is a function of the net current through the device. Additionally, as demonstrated by the memristor simulations described herein, a gradient in concentration of the ionic species in the electrolyte will change the doping profile and produce a change in resistance without the removal of ionic species.

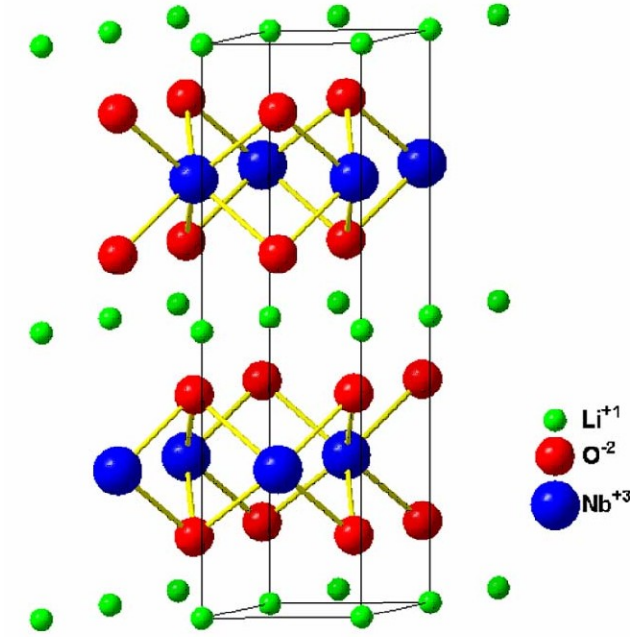

Figure 1.5: Crystal structure of $LiNbO_2$ which is composed of layers of niobium oxide with intercalated lithium between the layers [39].

Finally, a solid-state implementation of an ionic-electronic memristive device has been developed [7]. In this implementation, lithium ions drift due to an applied bias which results in a change in doping profile and thus a change in resistance. Lithium motion is facilitated with the layered structure of $LiNbO_2$ shown in Figure 1.5 and has been confirmed using nuclear magnetic resonance[28].

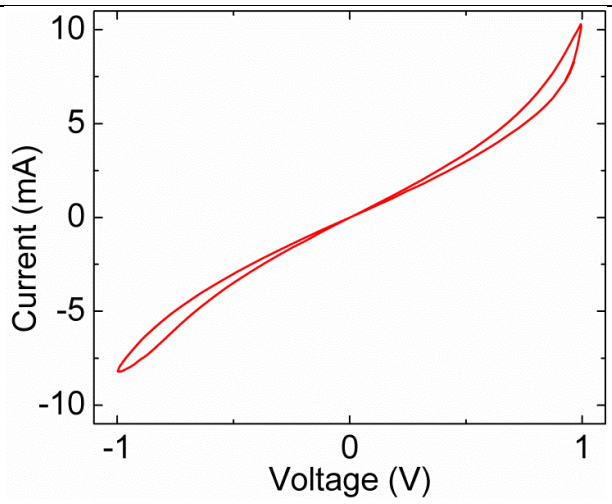

Figure 1.6: Analog $LiNbO_2$ Memristor I-V curve

Because of the large geometry, the lack of a set or reset voltage, and the independence of the memristance on scaling, it is theorized that the analog change in resistance observed in the lithium niobite memristor is due to the drift and diffusion of lithium which results in a (lithium) doping gradient and not a result of filamentary conduction. Analog functionality is shown in the I-V curve in Figure 1.6 which has is similar to Figure 4 from Chua's original active device implementation of the memristor [5]. Nickel contacts are used in this device because Ni does not readily alloy with lithium [66].

Finally, one of the first analog ionic memristor-like devices developed was termed a "memistor" and was not connected to Chua's original theorization of the memristor because the device had three terminals [67]. It is still worth noting this device since it is one of the first implementation of an analog device with a conductivity that depends on previous current inputs to the device. The memistor has a base WO_3 layer that is covered with a sandwich of SiO_2-Cr_2O_3-SiO_2 [67]. H^+ ions are injected from the Cr_2O_3 layer to

dope the WO_3 film resulting in an increase in conductivity. The memistor has a resistance state that spans orders of magnitude (10^5 to 10^9). Despite having promising analog functionality, the tungsten oxide-based memistor suffered from reliability issues because the constant cycling of H^+ ions produced gas pockets under the contacts, much like the oxide resistive switch, which lead to failure. It was theorized that the reliability of the memistor could be increased by doping the WO_3 film with metal ions instead of H^+ ions.

Beginning with Chua's original formulation, memristor research has witnessed many innovative advances as shown in Table 1.2. The WO_3-based memistor, although not connected to Chua's original idea, was one of the first devices to take advantage of dopant drift and diffusion to modulate the device resistance. Digital resistive switches exploit the same dopant drift and diffusion to create memristors well-suited to digital logic and digital memory applications. Analog memristors, including the Si/Ag graded doped memristors, the lithium-containing memristor, and the organic analog memristor, are a quickly-emerging class of devices that are capable of emulating synapses in the brain and could be a critical enabling circuit element for neuromorphic computing architectures.

Table 1.2: Significant memristive devices and their associated resistance modulation mechanisms.

Memristive Material System	Reference	Resistance Modulation Method
Silicon (original Demonstration)	[5]	Multiple Active Devices
Transition Metal Oxides (ex: TiO_2)	[6]	Filament Conduction
Ag/Si Graded Doping	[59]	Filament Conduction Front
Ferromagnetic-Semiconductor Junction	[60]	Spintronics
Electrolytic Cell	[65]	Electrolyte Species Removal
Analog Organic	[63]	Cation Drift and Diffusion
Analog Inorganic	[7]	Cation Drift and Diffusion

1.3 Neuromorphic Computing

From "the last of the great mathematicians" [68] to the inventor of the Palm Pilot [69], neuromorphic computing is an area that has generated a huge amount of interest in a wide variety of innovators. Neuromorphic computing is a biologically-inspired computational architecture that seeks to compute similarly to the brain with interconnected low-power synapses and neurons. The neuromorphic computing architecture is a proposed solution to replace present-day computing devices which will begin to approach performance limits due to excess heat and power consumption [2].

Neuromorphic computing has been recently gaining popularity amongst industry and funding agencies. The Defense Advanced Research Projects Agency (DARPA) has dedicated over $102.6 million toward the development of a neuromorphic computing system with 10 billion neurons and 100 trillion synapses [70]. The DARPA SyNAPSE program, which is will last through 2016 is expected to usher in the dawn of a new computing paradigm as shown in Figure 1.7. In addition to DARPA, companies such as IBM and Qualcomm are presently pushing into neuromorphic computing, further confirming its place as a commercially-viable technology [71-73].

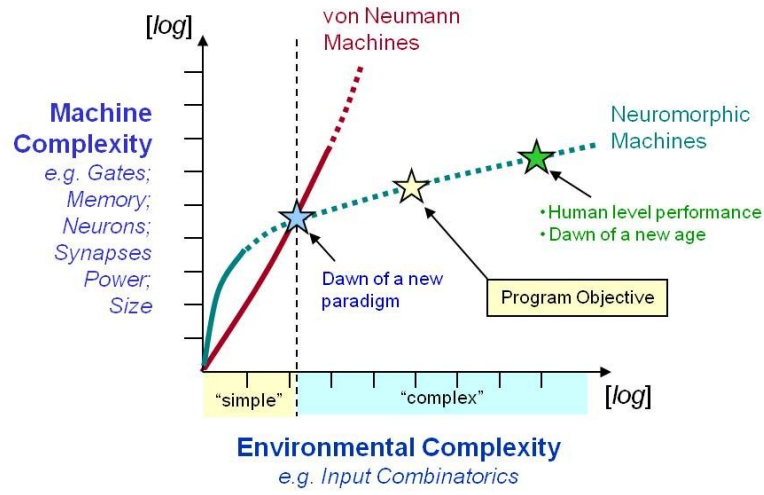

Figure 1.7: DARPA roadmap for neuromorphic computing machines [70].

Neuromorphic computing research has also increased in popularity in academia. As shown by Figure 1.8, the number of papers containing the phrase "neuromorphic computing" published each year on the INSPEC™ database has been increasing recently, with a nearly exponential rise in recent years.

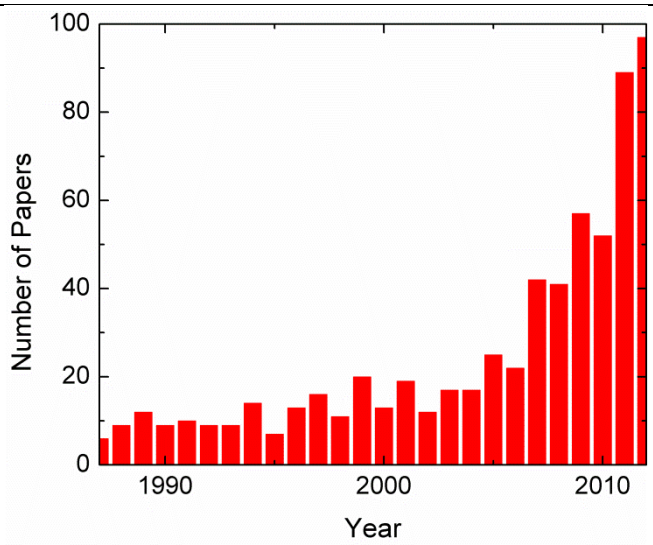

Figure 1.8: Number of papers containing the phrase "neuromorphic computing" on INSPEC™ Database published per year.

As scientific inquiry gains popularity and presses deeply into the realm of unknowns, a critical opposition can be expected. For example, at the University of Cambridge, there is a centre for the study of existential risk for those who recommend scientists exert caution when pushing forward neuromorphic computing or advanced artificial intelligence [74]. The researchers at the centre for the study of existential risk are worried about possible catastrophic risks associated with advancements in artificial intelligence and the possible implications of intelligent machines capable of furthering their own intelligence. It is always good to keep possible dangers of any new technology in mind, but the potential benefits of neuromorphic computing are abundant, so it is an area worthy of significant scientific investigation.

The potential benefits of hardware-based neuromorphic computing are widespread. Societal impacts of hardware neuromorphic computing implementations already include enabling sensors for those with disabilities. Neuromorphic vision sensors

and cochlear implants offer life-changing enabling technologies for those with vision and hearing disabilities [75-77]. Additionally, neuromorphic silicon-based vestibular implants have been developed for those with a potentially debilitating loss of balance [78, 79]. Brain-machine interfaces can use neuromorphic hardware and also promise to enhance functionality for both people with and without disabilities [80-82]. Brain-machine interfaces also have military defense applications, with cybernetic insects recently being controlled remotely to carry out intelligence missions [83]. Most neuromorphic implementations have been realized using silicon-based circuitry. A more natural implementation of these implementations would utilize ionic motion, similarly to the neurons and synapses in the brain.

The ionic-electronic based memristor is a key enabling device for neuromorphic computing because it exhibits a conductance response similar to that of a synapse using ionic motion. Recent neuromorphic implementations require multiple digital memristors per synapse and additional circuitry to encode the state of each synaptic weight [84]. Using multiple digital memristors to implement a single analog synapse will limit synaptic density, and this limitation indicates the necessity to develop and advance analog memristors which will not require extra circuitry to emulate synapses.

CHAPTER 2 : Investigation of the Analog Memristive Mechanism in $LiNbO_2$-based Memristors

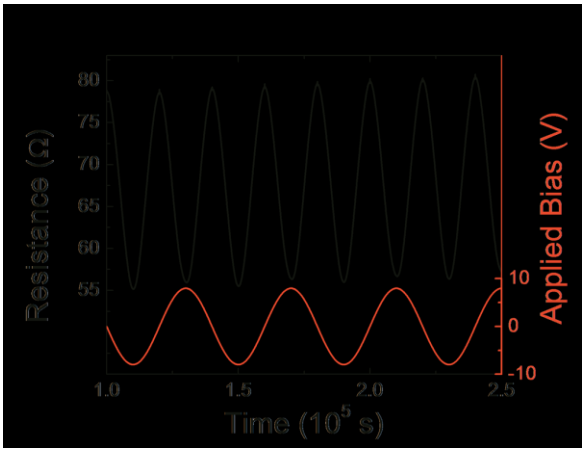

Figure 2.1: Resistance response of a p-type $LiNbO_2$ memristor to a sinusoidal input voltage demonstrates continuous resistance changes for a large range of input voltages.[85]

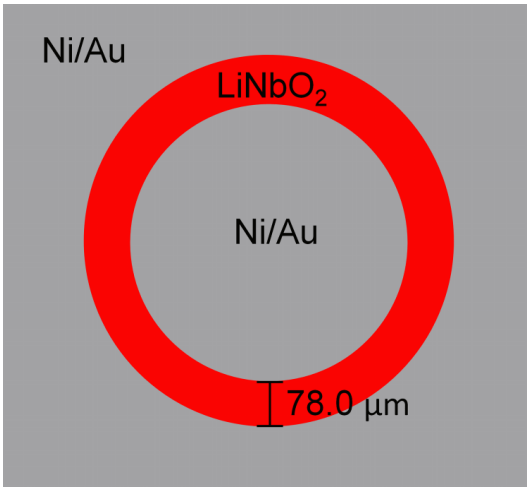

Figure 2.2: Schematic of an annular memristor. The spacing between electrodes is 78.0 µm and the electrode material is a 150 nm/ 50 nm Ni/Au metal stack.[85]

2.1 Introduction

In order to investigate the memristance mechanism in $LiNbO_2$ devices, analog $LiNbO_2$ memristors were used in an in situ X-ray absorption spectroscopy experiment. Analog memristors based on $LiNbO_2$ used in this investigation are implemented ranging in lateral dimensions of 50.0 µm to 0.5 cm. The analog nature of an annular $LiNbO_2$ memristor with a 78.0 µm device spacing is shown in Figure 2.1. A schematic of this device is shown in Figure 2.2. Nickel metal contacts are used to block lithium, and there is an expected accumulation of lithium at the $LiNbO_2$ - nickel interface [86]. With a sinusoidal voltage applied across the memristor, the resistance steady-state value changes, thus proving analog functionality. The voltages used to read the resistance values shown in Figure 2.1 are the same as those used to bias the device. In addition to

matching the analog nature of synapses in the brain, these memristors are complementary, meaning they can be grown as either n or p-type resulting in an analog decrease or increase, respectively, in resistance as a constant bias is applied [7]. This complementary resistance response is an attractive quality for neuromorphic computing applications since these $LiNbO_2$ memristors are capable of emulating both excitatory and inhibitory synapses.

$LiNbO_2$ is a lithium-intercalated, layered sub-oxide that has been investigated for superconducting and battery applications [27, 31]. Analog memristive $LiNbO_2$ thin films are grown using an oxi-chloride Varian Gen-II Molecular Beam Epitaxy (MBE) system on both Al_2O_3 and SiC substrates at a substrate temperature of 850° C [7, 39]. The precursors for the growth of $LiNbO_2$ include Li and $NbCl_5$ in conjunction with an oxygen plasma. Details of the growth and X-ray Diffraction (XRD) studies are found elsewhere [39], but in summary, single-phase, crystalline memristive $LiNbO_2$ films are grown providing a rapid lithium diffusion path along the layered plane. It is theorized that the analog functionality of $LiNbO_2$ memristors is due to the rapid drift and diffusion of lithium in the device, which is supported by impedance [7] and nuclear magnetic resonance spectroscopy [28]. However, direct physical evidence of the drift and diffusion of lithium dopants as the underlying memristive mechanism in $LiNbO_2$ memristors has not yet been shown.

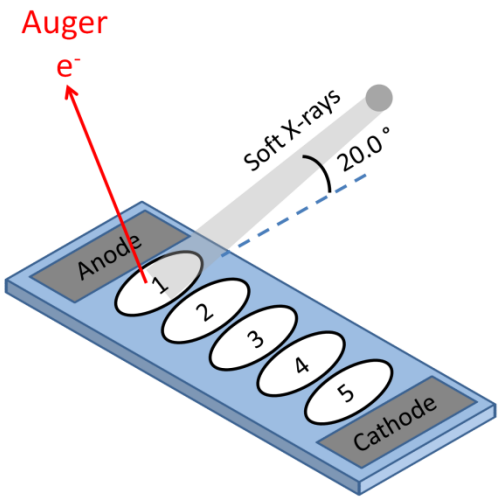

Figure 2.3: NEXAFS experimental setup. The incident X-ray beam irradiates the memristor at an angle of 20 degrees from the plane of the sample.

2.2 Experimental Setup

A detailed physical analysis of the analog resistance change mechanism in $LiNbO_2$ memristors provides insight into possible device modifications to improve both speed and non-volatility. Herein, the analog resistance change is investigated by probing empty electronic states using Near-Edge X-ray Absorption Fine Structure spectroscopy (NEXAFS). $LiNbO_2$ memristors are characterized using oxygen K-edge (O K-edge) NEXAFS in both the as-grown state and with a 2.0 V constant bias applied across the device. At the biased experimental condition, the current level is approximately 20 mA and the current density is .04 $\frac{mA}{\mu m^2}$. To determine spatial changes in the memristor as a function of applied bias, five regions are investigated with an approximate radius of 1.0 mm parallel to the flow of current through a 0.5 cm x 1.0 cm x 120.0 nm memristor. NEXAFS spectra are collected at the National Institute of Standards and Technology soft X-ray beam line U7A of the National Synchrotron Light Source at Brookhaven National

Laboratory. The incident X-ray beam irradiates the memristor at an angle of 20° from the plane of the sample as shown in Figure 2.3.

2.3 Determination of Memristive Mechanism in $LiNbO_2$ Analog Memristors

The normalized spectra with both the as-grown and biased states of the memristor are shown in Figure 2.4. There are five main structures exhibited in the O K-edge NEXAFS which are labelled by their orbitals in Figure 2.6. These structures are associated with hybridizations of O 2p orbitals with Nb 4d, 5s, and 5p orbitals. This interpretation is based on a similar lithium intercalated compound, $LiCoO_2$[87] and a niobium layered compound, NbS_2[88], which has trigonal prismatic coordination similar to that in $LiNbO_2$. A schematic density of states (DOS) for layered semiconductor compounds with trigonal prismatic symmetry similar to $LiNbO_2$ is shown in Figure 2.6. The lowest energy peak probed is attributed to the partially occupied A_1' (d_{z^2}) orbital and is labelled in Figure 2.6 [88]. It should be noted that, under the nominal $4d^2$ electron configuration for $LiNbO_2$, the A_1' orbital should be fully filled and would not appear in NEXAFS (no unoccupied DOS available). The fact that the A_1' is visible suggests it is not fully occupied and the remaining electron density is shared with other orbitals. The second lowest energy peak is attributed to the higher energy sub-band from the split of the t_{2g} level of the niobium d-bands, E' (d_{xy} ; $d_{x^2-y^2}$). The subsequent higher energy peak is attributed to the E" (d_{yz} ; d_{xz}) orbital and is expected to be completely empty in stoichiometric $LiNbO_2$ where Nb has a formal 3+ oxidation state and thus a $4d^2$ electron configuration. The two highest-energy peaks, which should be fully empty, are assigned

to the transitions to hybridized states of oxygen 2p and Nb 5sp (s, p_z, p_x, p_y) orbitals [89].

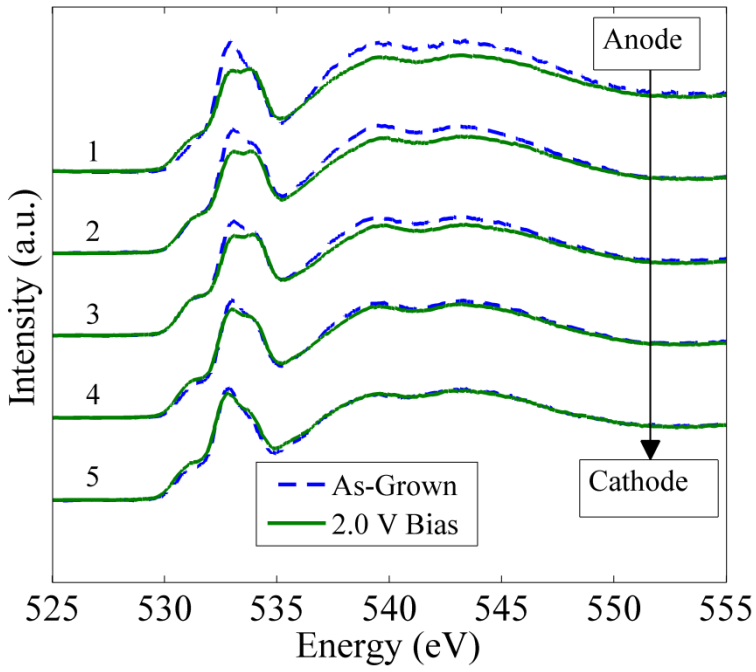

Figure 2.4: Normalized NEXAFS spectra of an as-grown (blue) and 2.0 V biased (green) $LiNbO_2$ memristor. Five regions are collected spatially oriented in parallel with the flow of current with a soft X-ray beam of approximately 1.0 mm in radius. The spectra labeled "1" shown at the top of the figure are collected closest to the anode of the device while the spectra at the bottom labeled "5" are collected close to the cathode of the device. The three spectra in the middle are equally spaced between the anode and cathode. Each plot is normalized to a step edge of 1.0.[85]

The as-grown spectra subtracted from the biased spectra are shown in Figure 2.6 to highlight small changes in the absorption spectra. From the difference spectra in Figure 2.6, it is clear that as a bias is applied across the memristor, there is a spatial trend in the O K-edge NEXAFS peaks. Specifically, peaks corresponding to the d_{z^2}, d_{yz}, and d_{xz} orbitals show a change in the relative DOS that goes through a minimum near the

center of the polarized memristor, while peaks corresponding to the d_{xy}, $d_{x^2-y^2}$, s, p_z, p_x, and p_y orbitals show a monotonic increase in relative DOS going from the anode to the cathode. This spatial trend is in response to the drift of lithium ions in the layered material. As a positive bias is applied to the anode of the memristor, lithium ions drift towards the grounded cathode. As these lithium ions drift toward the cathode, they leave behind an uncompensated electron in the anodic region. Going from the anode to the cathode, there is a distinct difference in the NEXAFS spectra of the d_{xy}, $d_{x^2-y^2}$, s, p_z, p_x, and p_y orbitals between the biased and as-grown memristor. This difference in the biased and as-grown spectra diminish until it reaches its lowest point at the cathode.

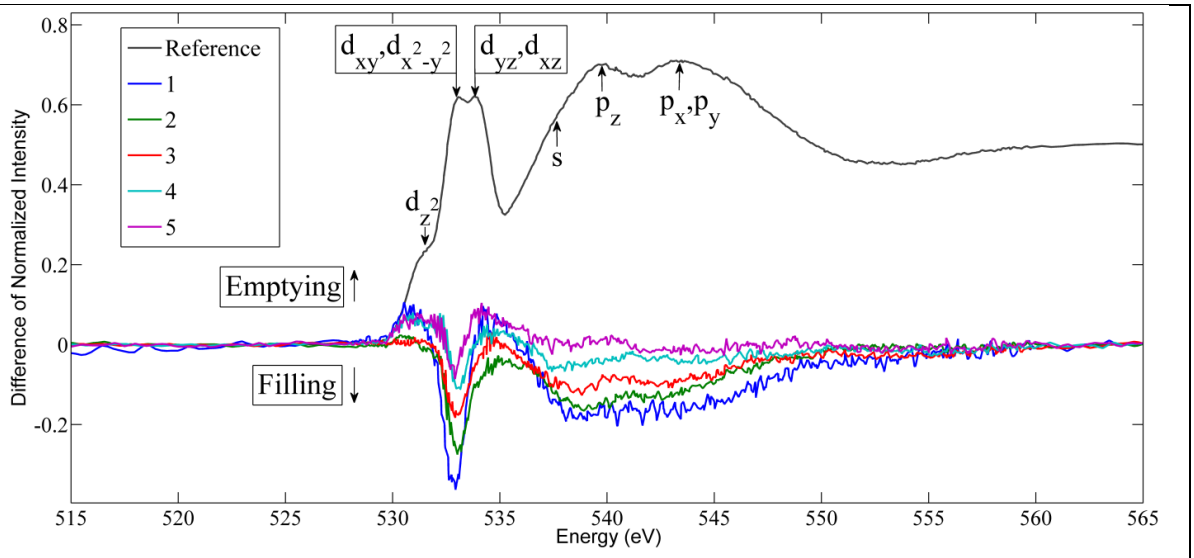

Figure 2.5: Difference NEXAFS spectra of a biased and as-grown $LiNbO_2$ memristor. The difference spectra are collected to determine spatial changes in the $LiNbO_2$ memristor as a function of applied bias where region 1 is closest to the anode and region 5 is closest to the cathode of the device. A reference spectrum (position 4 biased) is included for comparison.[85]

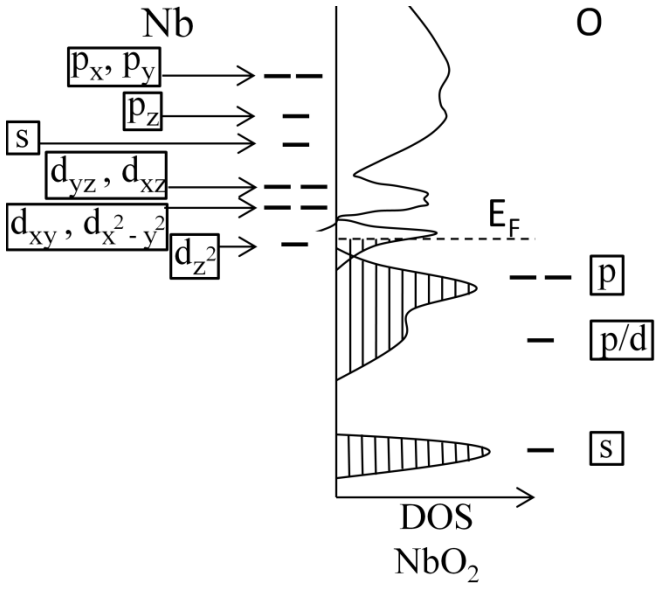

Figure 2.6: Schematic effective density of states distribution for layered trigonal prismatic semiconductors. The dominant contributions of atomic states to the electronic bands are shown with filled states represented by dashed lines. After Jaegermann and Tributsch [89] modified for actual shape determined from the NEXAFS spectrum of $LiNbO_2$.[85]

The epitaxial nature of the film implies that the distortion in the c-axis versus a-plane bonds will obey the Poisson relationship implying opposite trends. The s, p_z, p_x, and p_y orbitals are fully empty, thus the changes in these peaks are not the result of electronic transitions but rather the asymmetric strain and its associated distortion in the crystalline lattice. This asymmetric strain as a function of lithium concentration has been confirmed by XRD studies [29]. We expect this symmetry effect to affect all orbitals. Additionally, the d_{z^2}, d_{xy}, $d_{x^2-y^2}$, d_{yz}, and d_{xz} orbitals have contributions from both structure and electronic transitions. The trends in the d_{z^2}, d_{yz}, and d_{xz} orbitals are very similar to each other since they both have z-axis contributions, whereas the d_{xy} and

$d_{x^2-y^2}$ orbitals, which show a different trend, represent only x-y plane contributions to the DOS. The net negative charge that remains from the lithium ions that are drifted away at the anode has an overall effect of decreasing the DOS of the d_{xy} and $d_{x^2-y^2}$ orbitals (plot 1 of Figure 2.6), and this relative decrease itself becomes less prominent towards the cathode (plots 2-5 in Figure 2.6) supporting the idea of the memristance mechanism is dominated by the drift of lithium. Although the d_{xy}, $d_{x^2-y^2}$, s, p_z, p_x, and p_y orbitals show similar trends spatially across the memristor, the changes are more pronounced in the d_{xy} and $d_{x^2-y^2}$ orbitals simply because both the symmetry distortion effects and the effect of decreased unoccupied DOS in the x-y plane are additive. The most dramatic change in the orbitals with x-y plane contributions correspond to the area adjacent to the positively biased contact due to the greatest coulombic repulsion being exerted on the lithium ions in that area.

Unlike the d_{xy}, $d_{x^2-y^2}$, s, p_z, p_x, and p_y orbitals, the d_{z^2}, d_{yz}, and d_{xz} orbitals contain z-axis projected DOS, and show a net increase in the unoccupied DOS at the anode of the memristor. This effect decreases gradually towards the cathode. However, we are not able to observe this trend fully since the asymmetric strain distortion effects (which increase the DOS going from the anode to the cathode) dominate from plots 3-5 in Figure 2.6. The resulting effect is a minimum in the difference DOS for the d_{z^2}, d_{yz}, and d_{xz} orbitals in the area of the memristor located between the anode and cathode.

X-Ray Absorption Spectroscopy studies of $LiNbO_2$ investigating the change of the Nb-L_{III} edge as a function of lithium concentration find that as lithium is extracted from the crystal structure, two higher energy peaks are created. It was expected that the deintercalation of lithium from the material should result in the emptying of the d_{z^2} orbital, and thus a lower energy peak would emerge. Instead, these two higher energy peaks are attributed to a distortion in the Nb-O trigonal symmetry. In contrast, the O K-edge study of $LiNbO_2$ presented herein suggests that the growth of the peaks corresponding to the E' orbitals as lithium is drifted away results from a significant portion of the charge in $Li_{1-x}NbO_2$ (where $x>0$) is compensated by oxygen which is in agreement with theoretical investigations [33].

The results discussed herein suggest that the memristive response in $LiNbO_2$ memristors is facilitated similarly to that in the filamentary digital memristors. That is, the underlying mechanism for the resistance modulation is the drift and diffusion of ions in the crystalline lattice. Specifically, the $LiNbO_2$ memristor relies on the drift and diffusion of lithium while the digital memristors rely on oxygen drift. The main differences between the two different types of memristors are the permanence in memory and the analog or digital nature of the memristors. The rapid drift of oxygen ions in filamentary metal oxide based memristors is due to a thermal effect where the mobility of oxygen is amplified under application of a bias adequately high to produce substantial localized Joule heating [48]. When the state of the memristor is to be probed, the power applied to the device is sufficiently low to avoid a state change in the memristor. In the case of the $LiNbO_2$ memristor, lithium ions move through the layered crystal structure to produce a spatially graded profile of lithium and thus the analog $LiNbO_2$ memristor does

not rely on filamentary conduction. This lack of a thermally-activated filamentary memristive mechanism gives the $LiNbO_2$ memristor a truly analog response. Because the diffusion coefficient of the lithium ions producing the memristive response is not thermally amplified, the memory of a $LiNbO_2$ memristor has a greater level of volatility than that of a thermally-activated digital memristor. This volatility could be utilized in neuromorphic computing applications, since the device intended to be simulated using the memristor, the synapse, exists with both long and short term memory in the brain. Additionally, since there is now evidence that the modulation of resistance in these devices is facilitated by the movement of lithium, future devices with varying memory permanence could be designed around the storage of lithium ions through the use of an electrolyte [90].

2.4 Conclusions

In conclusion, the memristive mechanism of analog $LiNbO_2$ memristors is investigated by an *in situ* O K-edge NEXAFS study. The memristance effect in the $LiNbO_2$ film is attributed to the movement of lithium, which is shown to have a concentration gradient in a biased $LiNbO_2$ memristor. This gradual movement and eventual graded concentration profile of lithium is responsible for both the analog and volatile nature of the $LiNbO_2$ memristor. Although similar to memristors that rely on filamentary conduction in that vacancies are responsible for the resistance modulation, the gradual change in resistance sets the $LiNbO_2$ memristor apart in a new class of analog memristive devices void of conductive filaments. This filament-free mechanism should provide benefits in scaling and manufacturing in addition to being more directly applied to neuromorphic computing in a fashion analogous to mammalian brains.

CHAPTER 3 : Comparison of Interfacial and Bulk Ionic Motion in Analog Memristors

3.1 Impedance Spectroscopy and Digital Memristive Devices

TiO_2-based and related resistive switching devices operate in a digital regime, with a sudden change in resistance due to the formation and destruction of highly conductive filaments [17-20]. This formation or elongation of the conductive filament occurs predominately at the interface of the oxide and contact metal interface. This resistive switching mechanism in digital memristors has been investigated using impedance spectroscopy [54]. The impedance of an amorphous NiO film was probed in both highly resistive and conductive states. A circuit model fit to the impedance spectra of a digital memristor can be described by a resistor (5.49×10^4 Ω) in parallel with a capacitor, or a constant phase element, in the high resistance state as shown in Figure 3.1. In the low resistance state, an additional low resistance resistor (3.2 Ω) is added in parallel to the high resistance circuit model. This additional low resistance resistor is consistent with a conductive filament forming and shorting the memristor contacts to create a low resistance state. The capacitance in the digital memristor, no matter its state, remains the same value which indicates that the digital switching behavior is due to a filament-controlled NiO matrix [54].

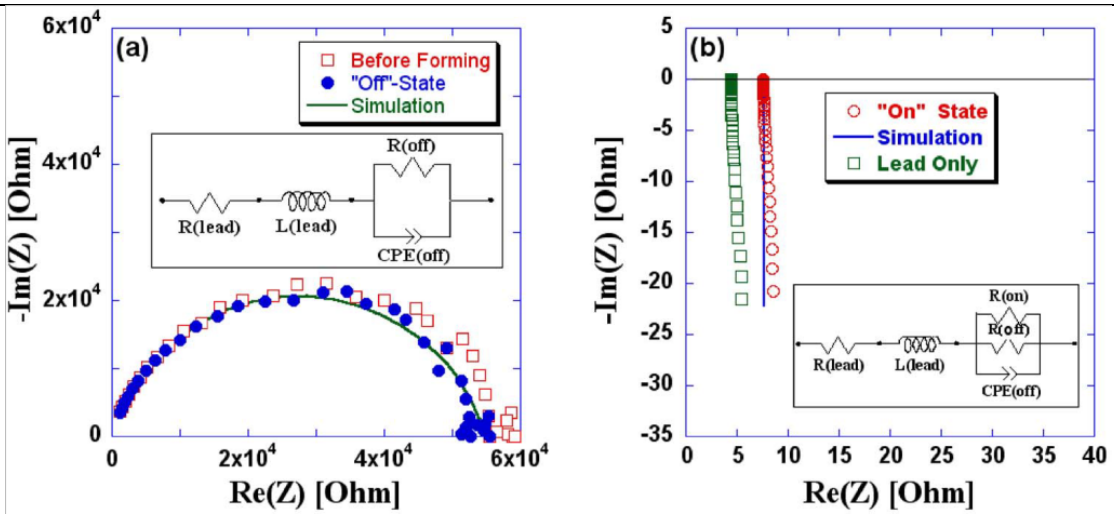

Figure 3.1: Impedance spectra of an atomic layer deposited digital memristor (a) before forming and in the "off" state and (b) in the "on" state. [54]

The digital change in resistance characteristic of the filamentary conduction in TiO_2 based memristors is absent in memristors based on the lithium-intercalated layered material, $LiNbO_2$ [7]. The lack of a digital resistance response (thus an analog response) is due to the movement of lithium atoms in the crystalline lattice similar to the movement of lithium in layered battery cathode material [85]. This analog resistance change is investigated herein by a combination of AC and DC methods, potentiodynamic electrochemical impedance spectroscopy (PDEIS) [91].

In addition to the memristor, the existence of two circuit elements, the meminductor and memcapacitor, were later theorized [92]. In the theorization, it was asserted that meminductance and memcapacitance can result from a system where the dynamical behavior of ions and electrons depend on the history of the system even at very short timescales [92]. $LiNbO_2$-based analog memristors are shown herein to exhibit both meminductive and memcapacitive behavior depending on the frequency of the applied AC signal, and this behavior is characterized by PDEIS.

At low frequencies, it is shown that the $LiNbO_2$-based devices demonstrate an inductive response as shown in Figures 3.3 and 3.4. As the bias and the spatial ionic distribution in the device is changed, the inductive response changes, thus indicating that the coupled electronic-ionic inductive response of the device presented herein is indeed a meminductor at frequencies below ~150 kHz. At higher frequencies, a capacitive response is demonstrated. As the bias across the device changes, the spatial ionic distribution changes. The change in capacitance shown in Figures 3.3 and 3.4 is due to this change in spatial ionic distribution and thus confirms the memcapacitive response of the device presented herein for frequencies above ~150 kHz.

3.2 Analog Cation-based Memristor Operation

The analog $LiNbO_2$-based memristor is composed of a molecular beam epitaxy (MBE) grown [7, 39] thin film (120 nm thick) of $LiNbO_2$ with a Ni/Au metal stack in an annular pattern as shown in Figure 3.2. The electrical resistance of the contacts is negligible compared with the electronic resistance of the device.

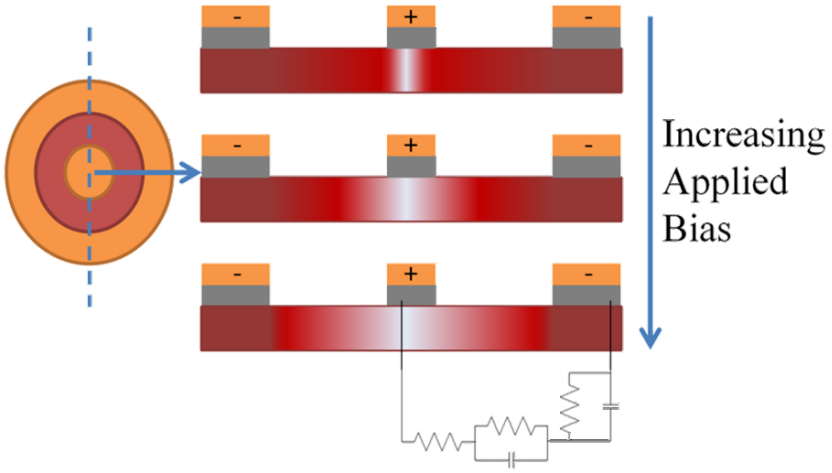

Figure 3.2: Schematic of an $LiNbO_2$ memristor. As an increasing DC bias is applied across the device, a greater number of lithium dopants drift from the positively biased anode to the cathode.[93]

By applying a DC bias across the two annular contacts, in direct analogy to a battery, lithium is drifted from the positively-biased contact (the anode) to the grounded contact (cathode). In the area closest to the anode, lithium vacancies are created which results in a highly conductive region. At the cathode, there is an accumulation and eventually plating of lithium [86, 94] resulting in an overall removal of lithium from the device. This accumulation and plating of lithium corresponds with an overall increase in conductivity of the p-type $LiNbO_2$ [36, 85].

Because the annular memristive device is asymmetric, interfacial and bulk effects can be distinguished. Specifically, there are two concentric ring interfaces with different diameters. As a positive bias is applied to the center contact (as shown in Figure 3.2), lithium is drifted towards the interface with a larger diameter. When a negative DC bias is applied to the center contact with respect to the outside contact, lithium is drifted

towards the smaller ring. Because the diameter, and thus the interfacial area, of the smaller ring is about half that of the larger ring (177 μm vs. 333 μm), as lithium is drifted towards the smaller ring, it will experience a constricted flow. The opposite is true in the case of drifting lithium to the larger ring interface. The asymmetric device operation is investigated herein by PDEIS.

3.3 Experimental Setup

Single phase, crystalline $LiNbO_2$ was grown in an oxi-chloride MBE system with evaporated growth constituents Li and $NbCl_5$ in conjunction with an oxygen plasma source [39]. After growth, samples were cleaned in deionized water, patterned with photoresist, and a Ni/Au metal stack was deposited on the $LiNbO_2$ film. Metal contacts were patterned in an annular structure with a separation of 78.0 μm between contacts. All $LiNbO_2$ devices analyzed were grown directly on sapphire substrates and thus the substrate has no electrical contribution to the measurements. Impedance measurements were collected using an Agilent 4294A High Precision Impedance Analyzer. The oscillation amplitude was fixed at 5 mV and impedance spectra were collected in a logarithmic frequency sampling from 40 Hz to 30.4 MHz.

Electrochemical Impedance Spectroscopy (EIS) is effective in a wide range of applications including battery cathode [95] and digital memristor characterization [54]. In EIS, the frequency of an input sinusoidal voltage (current) signal is varied, and the phase and magnitude of the resulting current (voltage) is analyzed. For potentiodynamic EIS (PDEIS), multiple EIS measurements are performed at varying DC biases.

3.4 Electrochemical Impedance Spectroscopy of $LiNbO_2$ Memristors

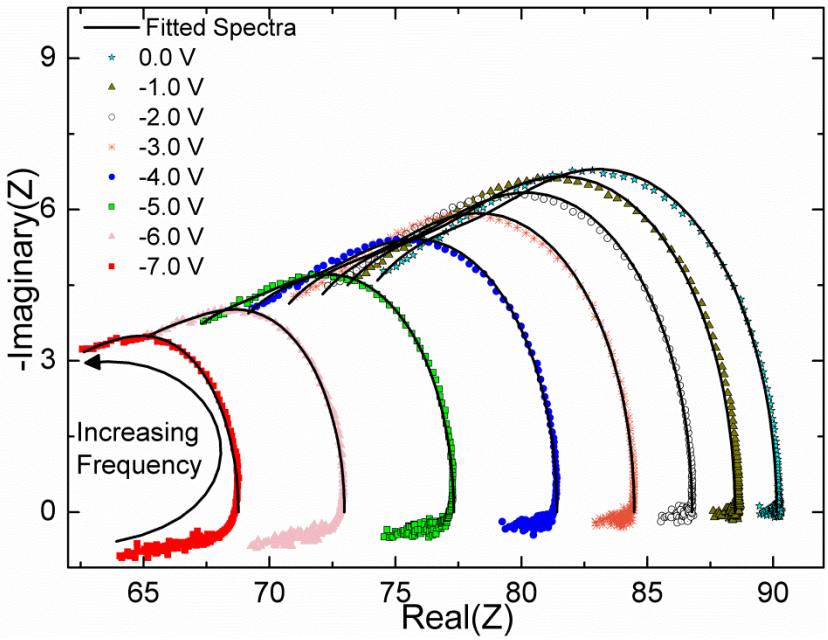

Figure 3.3: Negative Potentiodynamic Electrochemical Impedance Spectroscopy data from an $LiNbO_2$ memristor. DC biases ranging from -7.0 to 0.0 V are shown with 1.0 V steps.[93]

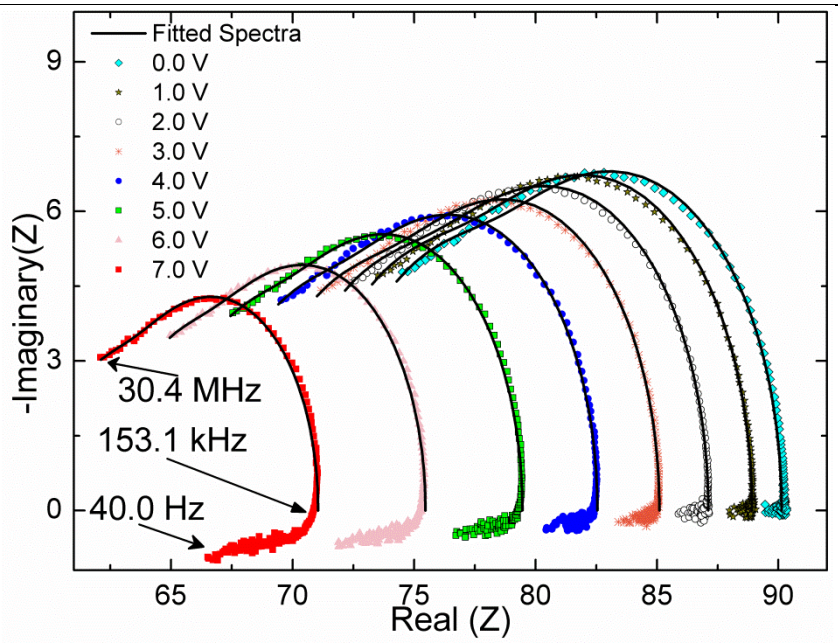

Figure 3.4: Positive Potentiodynamic Impedance Spectroscopy data from an $LiNbO_2$ memristor. DC biases ranging from 0.0 to 7.0 V with 1.0 V steps are shown.[93]

PDEIS was used to monitor the impedance response of an analog memristor as a function of DC bias. PDEIS spectra were taken at DC Biases from -7.0 V to 7.0 V in 1.0 V steps as shown in Figures 3.3 and 3.4. The impedance data excluding the low frequency inductive tail was fit to the circuit model shown in Figure 3.5 using the Levenberg-Marquardt algorithm implemented in the EIS Spectrum Analyzer software suite [96-98]. Since the system is highly overdetermined, having over 80 data points per bias selection and only 5 fitted unknowns, the error resulting from the fit is extremely low. Maximum single data point errors were 1.26% for resistances and 5.73% for capacitances while the average errors over all data points were only 0.39% for resistances and 1.95% for capacitances. Error bars are included in Figure 3.9 for the capacitances. Error bars are not included for the resistances shown in Figures 3.7 and 3.8 since the error bars do not appear on the scales of the figures.

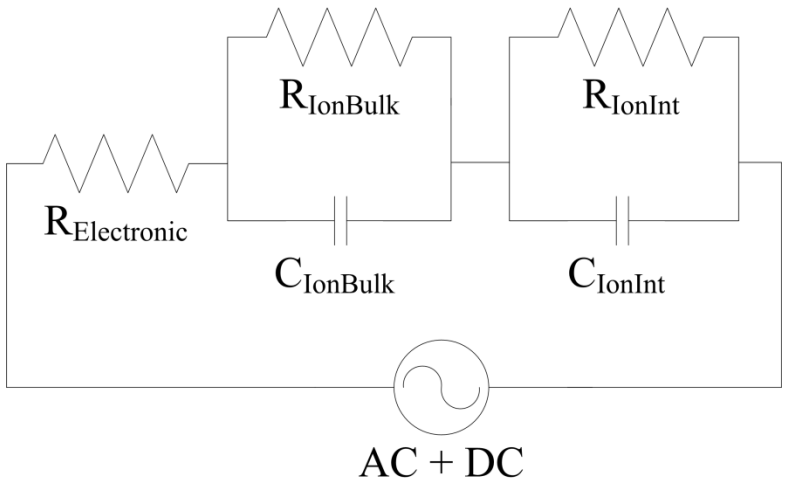

Figure 3.5: Circuit model for the potentiodynamic electrochemical impedance spectroscopy data shown in Figures 3.3 and 3.4.[93]

As the DC bias is increased, at low frequencies (40 Hz - ~ 150 kHz) there is an increase in the real component of impedance as frequency is increased. This resistance trend is opposite to the decrease in DC resistance found with increased DC bias. The resulting low frequency impedance is inductive as shown in Figures 3.3 and 3.4 and becomes increasingly inductive as the magnitude of the DC bias is increased. The inductive nature of this low frequency impedance is attributed to a net ionic current opposite to that of the applied electric field. Ionic current opposite to that of the applied electric field is attributed to diffusion relaxation. Because the inductance of the device depends on a coupled ionic-electronic dynamic response, the $LiNbO_2$ device exhibits the behavior of a meminductor [92].

A coupled ionic - electronic simulation accounting for both drift and diffusion of electrons, holes and ions describing the movement of ions in a 2.0 μm device with a 0.1 V DC bias applied across an analog memristor has been developed, and the spatial and temporal ionic response is shown in Figure 3.6. Initially, the lithium concentration is homogeneous at 70% of the stoichiometric level in the simulated device. As a constant bias is applied across the device, the lithium concentration becomes non-linear. Finally, at steady state, the concentration profile of lithium is linear and is the result of ionic drift and diffusion balance. The steady state DC balance of drift and diffusion of lithium is unbalanced by the applied low frequency AC voltage allowing diffusion to relax the accumulation of lithium back to lower concentrations. Indeed, within a cycle, at the instant in time of the zero AC electric field, ion current is already flowing due to diffusion relaxation resulting in an ionic current leading the AC electric field. This creates a leading ionic current in the opposite direction of the drift field, i.e. ionic

inductance. Since this observed ionic inductance results from ionic diffusion, we cannot rule out the possibility that this diffusion includes diffusion from the plated out lithium underneath the electrode. Both lithium accumulation and the plated lithium concentrations on the nickel electrode will be greater at higher DC biases making the ionic inductance increase with magnitude of DC bias. Figures 3.3 and 3.4 show that at frequencies greater than 150 kHz, the imaginary component of impedance begins to change quickly, indicating that lithium atoms are no longer able to track the applied sinusoidal voltage which results in the capacitive impedance response. When the impedance is dominated by capacitive effects, the data can be fit with a five component model similar to the model used for battery cathodes [99].

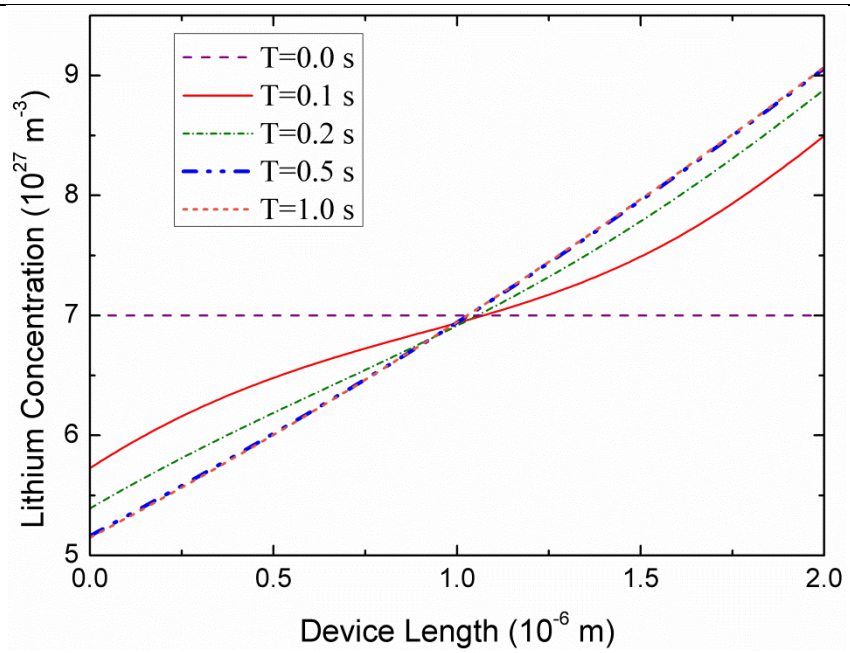

Figure 3.6: Temporal and spatial response of lithium concentration under the application of a 0.1 V bias in a coupled ionic-electronic simulation.[93]

The circuit model used to fit the potentiodynamic impedance spectroscopy data includes two resistor/capacitor parallel combinations ($R_{IonBulk}||C_{IonBulk}$ and $R_{IonInt}||C_{IonInt}$)

in series with a third resistor, $R_{Electronic}$ as shown in Figure 3.5. The model used to attribute physical meaning to the aforementioned circuit elements is adapted from the cathode portion of a battery structure [99]. The resistor $R_{Electronic}$ is added to the battery structure model to account for the bulk semiconductor resistance and is not seen in a battery structure because the use of an electrolyte blocks electronic current. $R_{IonBulk}$ and R_{IonInt} are attributed to interfacial and bulk ionic resistance. $R_{IonBulk}$ and R_{IonInt} have corresponding capacitances, $C_{IonBulk}$ and C_{IonInt} that describe the phase offset between lithium motion and the applied sinusoidal voltage in the bulk and at the interface, respectively. The measured C_{IonInt} interfacial capacitance will result from two separate, but electrically indistinguishable series connected capacitors $C_{IonIntInner}$ and $C_{IonIntOuter}$ corresponding to the inner and outer electrode-semiconductor interfaces.

A simple parallel combination of a single resistor and capacitor in series with the bulk resistance was not used to fit the $LiNbO_2$ analog memristor impedance spectroscopy data due to severe errors and a disagreement in shape between the circuit model and the impedance data. Likewise, a constant phase element, which was used to describe the impedance response of NiO digital memristor, was not used here to describe the impedance response of the $LiNbO_2$ analog memristor because the capacitance in MBE grown $LiNbO_2$ memristors is not dominated by the lack of long-range order unlike the amorphous NiO digital memristor [54].

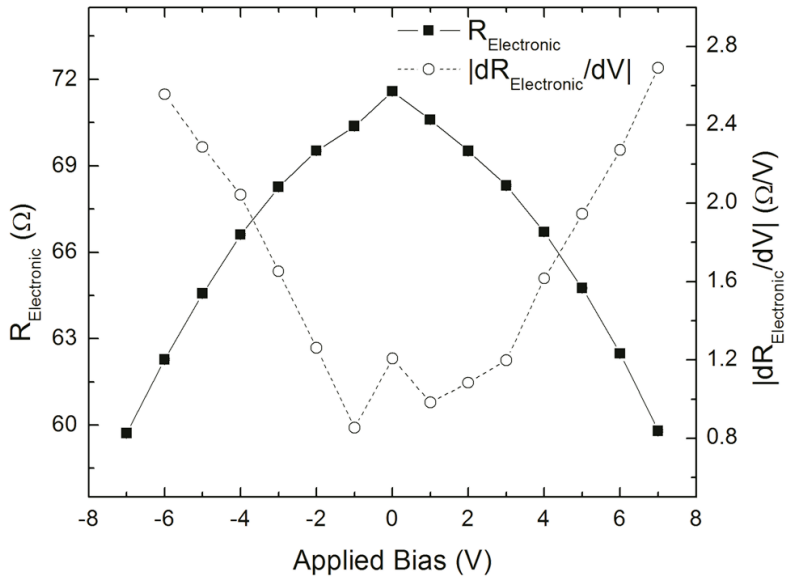

Figure 3.7: Bulk electronic resistance ($R_{Electronic}$) as a function of applied DC bias as extracted from the PDEIS data and fit to the model shown in Figure 3.5.[93]

The bulk resistance, $R_{Electronic}$, is plotted as a function of DC bias in 3.7. The resistance of $R_{Electronic}$ decreases as the magnitude of the DC bias increases. This change in bulk resistance due to the application of a DC bias can be explained by the movement of lithium in the device as a function of DC bias. At low biases, a small amount of lithium is shifted in the bulk of the device, resulting in a small change in bulk resistance. As the DC bias is increased, higher concentrations of lithium are driven to the cathode - semiconductor interface which results in an even larger change in resistance. The relative rate of resistance change increases as the magnitude of the applied DC bias is increased as shown in Figure 3.7. This increased rate of resistance change is attributed to the increased plating or intercalation of lithium into the nickel electrode at higher DC biases.

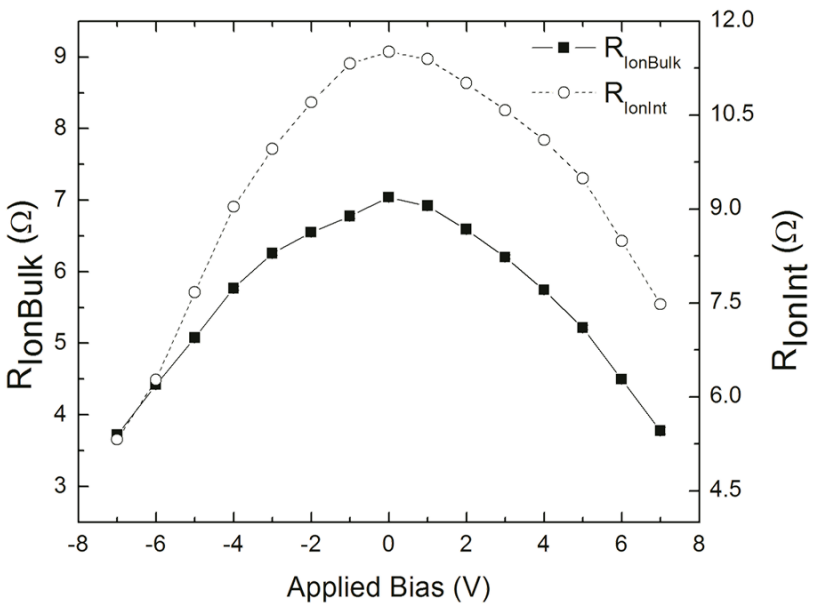

Figure 3.8: Bulk ionic resistance ($R_{IonBulk}$) and interfacial ionic resistance (R_{IonInt}) as a function of applied DC bias. As the magnitude of the DC bias is increased, lithium is drifted towards the cathode, resulting in a decrease in both the bulk and interfacial ionic resistance. Because the device is asymmetric, the interfacial ionic resistance changes more at negative biases due to the constrictive flow effect of the annular structure and the resulting increased accumulation of lithium at the electrode with a smaller diameter.[93]

The bulk ionic resistance, $R_{IonBulk}$ shown in Figure 3.8 exhibits the same trend as the bulk electronic resistance. That is, the bulk electronic current decreases as the magnitude of the applied bias increases. The change in the bulk ionic resistance is theorized to be due to the increased amount of lithium ions drifted under the application of an increasing electric field. As more lithium is drifted, it likely is plating or intercalating into the metal electrode at an increasing rate increasing the number of Lithium vacancies and thus increasing the ion mobility. This plating and/or intercalation is responsible for the increase in the bulk ionic current and thus a decrease in bulk ionic resistance.

Like the two bulk resistances, the interfacial ionic resistance, R_{IonInt}, decreases as

the magnitude of the applied bias increases as shown in Figure 3.8. Unlike the two bulk resistances, the interfacial effects of a larger and smaller interface area due to the different sized concentric radial interfaces are clearly evidenced in the interfacial ionic resistance as an asymmetric resistance response centered around zero bias. As a positive bias is applied on the outer ring with respect to the inner ring, ionic current crowding is experienced at the smaller diameter electrode interface that is not seen when the reversed bias is applied. The increase in ionic current is realized by a decrease in ionic interfacial resistance as seen in Figure 3.8.

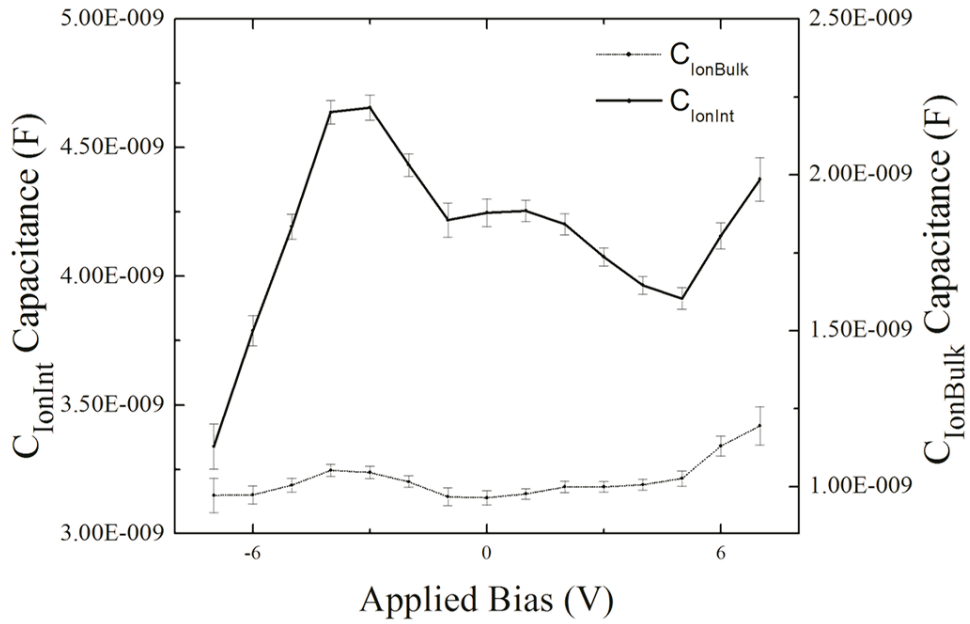

Figure 3.9: Bulk capacitance (CIonBulk) and interfacial capacitance (CIonInt) as a function of DC bias. The bulk capacitance, $C_{IonBulk}$, is relatively flat throughout the entire DC bias range. There is a slight increase in the bulk capacitance at the higher positive DC biases which is attributed to more lithium being driven towards the larger diameter ring.[93]

$C_{IonBulk}$, as shown in Figure 3.9, is attributed to the bulk ionic capacitance and shows little change over the range of DC biases applied across the analog memristor. The relatively small changes in the bulk ionic capacitance indicate that over the range of lithium concentration changes occurring in these measurements, there is little overall

change in mobility of lithium in the bulk. Given there is a rather large change in electronic resistance $R_{Electronic}$ in the bulk of the device, the actual lithium concentration change in the bulk would likely be substantial but not great enough to result in an ion mobility change. This is in contrast to the results above for the interfacial ionic capacitance C_{IonInt} where the lithium concentration changes are large enough to affect the interfacial ionic capacitance and thus the interfacial ionic mobility.

C_{IonInt} is a measure of the inability of ions to follow the electric field creating a phase offset. Thus, the interfacial capacitance, C_{IonInt}, provides a method for qualitatively examining the change in lithium ionic mobility at the $LiNbO_2$ - nickel interface as a function of bias. The complex changes in C_{IonInt} versus bias are attributed to the interplay between the lithium-depleted and lithium-rich interfaces. The two different area interfaces swap ionic capacitance dominance at opposite DC bias polarity resulting in different net ionic capacitance. In between these two endpoints, the capacitance is a complex mixture of these two capacitances.

The sharp drop in capacitance of C_{IonInt} at biases lower than -4.0 V is attributed to the increased accumulation of lithium at the smaller diameter metal - semiconductor interface. Because lithium is being driven from a larger contact interface to a smaller contact interface, a constrictive flow effect will take place, thus allowing a greater accumulation of lithium. As lithium accumulates, lithium crowding and a lack of available lattice sites will lead to reduced mobility and thus lower ionic capacitance [100]. This change in ionic capacitance based on the lithium concentration profile in the device is the basis for the assertion that $LiNbO_2$ devices exhibit memcapacitive behavior. The memcapacitive and meminductive responses will act as parasitic losses and set both

the upper and lower frequency response limits for the ionic programming of neuromorphic devices. Future efforts will explore the scaling of devices and how these parasitic losses affect the temporal response of nanoscale $LiNbO_2$ analog memristors.

3.5 Conclusions and Implications on Future Devices

The analog resistance change in an $LiNbO_2$ memristor is characterized by PDEIS. Additionally, it is shown that the $LiNbO_2$ devices exhibit analog memristive behavior and can exhibit memcapacitive and meminductive responses at certain frequency ranges. The PDEIS data suggests that the change in resistance of an analog $LiNbO_2$ memristor under the application of a DC bias is due to the drift of lithium atoms and thus a redistribution of dopants in the device. Additionally, it is shown that with increasing electric fields in the device, there is a larger resistance change and the majority of this resistance change occurs at the metal - semiconductor interface. Larger resistance changes have been shown herein to depend on higher electric fields and the dominance of interfacial properties on the operation of the $LiNbO_2$ analog memristor. The dominance of resistance response on electric field and interfacial properties suggest that the fabrication of analog memristors with negligible bulk dimensions will enhance analog memristor functionality.

CHAPTER 4 : Halide-based MBE of epitaxial metals and epitaxial oxides

4.1 Introduction

It is theorized that the performance of the most common device used in computation, the silicon transistor, will soon be dominated by parasitic resistance [1]. New materials and devices will be crucial in continuing to move computational speeds forward. The growth of both epitaxial oxides and metals that have the capability to satisfy the demands for next-generation computing applications is needed and has been demonstrated using a metal-halide growth chemistry.

Epitaxial metals grown using this chemistry include Nb, Fe, Ni, and Co. In addition to being an easily-implemented layer in an oxide stack or a contact metal for an oxide film, these epitaxial metals find applications as superconducting thin films [2], graphene seed layers [3], and in spintronic electronic applications [4].

Epitaxial oxides grown using the metal-halide chemistry include $LiNbO_2$ and $LiNbO_3$. $LiNbO_2$ is an obscure lithium-intercalated material [5] that has been investigated for its superconducting properties [6] and has a layered metal-oxide framework. This layered crystal structure facilitates the rapid movement of lithium ions and ultimately the memristive response of devices fabricated using $LiNbO_2$. The movement of lithium ions under the application of an electrical bias creates both lithium-rich and lithium-deficient areas separately in a device. Because lithium vacancies act as acceptors [7], the doping profile is simultaneously modulated as the lithium concentration profile is changed due to

the application of a bias across the memristor. This mechanism is investigated using impedance spectroscopy.

The fully-oxidized member of the Li + Nb + O family, $LiNbO_3$, is nearly lattice-matched to $LiNbO_2$ (0.2921 nm compared to 0.2987 nm for $LiNbO_3$ [8]), and is heavily researched because it is the linchpin for optical communication networks and various surface acoustic wave devices [9]. $LiNbO_3$ is used in these networks as an optical modulator, and the majority of these $LiNbO_3$ optical modulators are implemented using bulk $LiNbO_3$. It is preferable, if proven feasible, to use high-quality epitaxial $LiNbO_3$ in these applications to improve both high frequency performance, lower voltage drive and provide for increased integration.

The details of the metal halide growth chemistry are described elsewhere [10], but in general, the chemistry relies on a series of chemical reactions to form both the epitaxial metals and oxides. Primarily, lithium getters chlorine from the metal chloride species to produce both LiCl and the metal species. At elevated substrate temperatures (850°C), LiCl then desorbs from the growth surface. Optionally, under the application of an oxygen plasma, the metal species then oxidize. Depending on the metal incorporation rate and oxygen partial pressure at the growth surface, different oxidation states of the metal species can be achieved.

If an oxygen source is not initiated during the growth, and only lithium and the metal-halide sources are used, the growth will result in an epitaxial metal film.

Transition metals with low vapor pressures are difficult to deliver in MBE. Traditionally, MBE growth of these transitional metal oxides with low vapor pressure constituents has relied on metal organic precursors or evaporation via electron-beam

heating. Neither is an ideal solution. Metal organic molecular beam epitaxy growth of transition metal oxides experiences difficulties with pre-reaction and carbon contamination. Electron-beam heating to deliver refractory metals results in growth fluxes that are less stable than those using a lower temperature thermal cell.

An alternative approach described herein utilizes a chloride-based chemistry to produce growth level fluxes. At temperatures commonly used in MBE (30-700° C), stable beam equivalent pressures of ~10^{-6} Torr BEP are achievable, and unlike the metal organic solution, hydrogen and carbon contamination is not introduced with the growth constituents.

In addition to using easily controllable growth temperatures for transition metal growth constituents, the metal-halide based MBE approach can be implemented using only one source port on the MBE system to deliver multiple high vapor pressure metal-halide sources. Many heated sources can be connected via mass flow controllers which then feed into the growth chamber through a manifold facilitating robust expansion capability.

A third advantage to the use of the metal-halide vapor delivery system is that, with proper valve positioning, the sources can be recharged without opening the MBE chamber. After reloading the metal halide source materials, only a small source chamber needs to be baked out instead of the entire MBE system, thus reducing down time when reloading growth sources.

4.2 Experimental setup

Epitaxial Nb, Co, Fe, and Ni were grown on sapphire (006) substrates by MBE in a heavily modified Varian GEN II system using $NbCl_5$, $CoCl_2$, $FeCL_2$, and $NiCl_2$ as the

metal-halide sources respectively. Li was the chlorine getter constituent used in the growth of the epitaxial metals and is delivered from a modified valved cracker source. Epitaxial $LiNbO_2$ and $LiNbO_3$ were grown on 1 cm x 1 cm and 2" sapphire (006) and SiC (004) substrates. $NbCl_5$ was used as the metal halide source for these oxides and lithium was used to both getter the Cl and incorporates into the film. The active oxygen for the growth of the oxides was provided by an oxygen plasma source operating at 400-500 watts and 0-2 sccm. XRD studies were performed using a Philips PW3040 Pro MRD XRD system, and impedance spectroscopy measurements were performed using an Agilent 4294A precision impedance analyzer.

4.3 Growth of epitaxial metals

The metals Nb (Figure 4.1), Co (Figure 4.2), Fe (Figure 4.3), and Ni (Figure 4.4) have been grown epitaxially using the metal-halide growth chemistry discussed herein. The growth of these epitaxial metals proves that the metal-halide growth chemistry has the capability to produce a vast array of materials containing traditionally difficult to control transition metal growth constituents.

All metals were grown on (006) sapphire with Nb (Figure 4.1) and Co (Figure 4.2) demonstrating Pendellosung fringes, indicating the growth of a smooth film. Normal MBE growth fluxes (in the range of ~10^{-6} Torr) for $NbCl_5$, $CoCl_2$, $FeCl_2$, and $NiCl_2$ are attained approximately at temperatures of 90°C when fed through a heated ¼ inch stainless tube which acts as a flow restrictor and 400°C, 375°C, and 500°C respectively from standard effusion cells. In all cases, the temperatures required for growth-

Figure 4.1: XRD data for a (110) Nb layer grown on an (006) sapphire substrate [7].

Figure 4.2: XRD data for a (111) Co layer grown on an (006) sapphire substrate [7].

Figure 4.3: XRD data for a (110) Fe layer grown on an (006) sapphire substrate [7].

Figure 4.4: XRD data for a (111) Ni layer grown on an (006) sapphire substrate [7].

level fluxes using metal sources are more than twice those used in the evaporation of the metal halide species, and in the most extreme case (Nb), the metal source requires a temperature 24 times higher than that of the metal halide species for growth-level fluxes. By comparison, normal MBE growth fluxes for Nb, Co, Fe, and Ni metal species are attained approximately at the temperatures of 2000°C, 1500°C, 900°C, and 1000°C respectively. These elevated temperatures are very difficult to attain in an oxide system due to oxidation of the heated tantalum filaments.

While the flexibility of the metal-halide chemistry described herein has been demonstrated by the growth of the transition metals Nb, Co, Fe, and Ni, this growth chemistry is not limited to the delivery of the aforementioned metals. Any metal with a halide precursor can be integrated into this growth system. The ability to deliver a wide range of metals with stable fluxes that were traditionally difficult to control will open the door to a new generation of high-quality epitaxial materials. Additionally other group one elements could be used as needed to provide flexibility in substrate growth temperature by providing volatile chlorine getter species at lower temperatures than currently allowed for LiCl.

4.4 Growth of epitaxial oxides

In addition to metals, two functional oxides, $LiNbO_2$ and $LiNbO_3$, have been epitaxially grown from metal-halide precursors. Epitaxial $LiNbO_3$ has been grown previously by RF sputtering [11], MBE (using an e-beam source for niobium) [12], chemical beam epitaxy [13], and excimer-laser ablation [14]. In this work, we report the growth of high quality $LiNbO_3$ on both sapphire (Figure 4.5) and SiC (Figure 4.6) substrates with a best demonstrated XRD rocking curve FWHM of 150 arcseconds. Since $LiNbO_3$ is the fully oxidized combination of Li + Nb + O, films are grown with a large overpressure of oxygen to reduce oxygen vacancies. $LiNbO_3$ is a high-κ dielectric, can be used as an optical modulator, and is proposed to be used as a gate dielectric for a transistor made from its lattice-matched semiconducting sub-oxide counterpart, $LiNbO_2$.

Figure 4.5: XRD data for a (006) $LiNbO_3$ layer grown on an (006) sapphire substrate [7].

Figure 4.6: XRD data for a (006) $LiNbO_3$ layer grown on an (004) SiC substrate [7].

Semiconducting $LiNbO_2$ has been grown on both sapphire (Figure 4.7) and 4H SiC (Figure 4.8) substrates. SiC has a very small lattice mismatch of 2.8% to $LiNbO_2$ (0.2987 nm compared to 0.3073 nm for SiC) $LiNbO_2$ is grown by controlling the ratio of Nb to O incorporation in the film. The FWHM of the XRD rocking curves for both

$LiNbO_2$ grown on SiC and sapphire shows excellent film quality, with a FWHM of 540 arcseconds and 190 arcseconds, respectively. In addition to being a semiconductor, $LiNbO_2$ has a lithium intercalated metal-oxide layered framework [15] that facilitates the rapid movement of lithium ions.

4.5 $LiNbO_2$ memristors

The rapid movement of lithium in $LiNbO_2$ films facilitates the memristance response in devices fabricated from the material. A memristor is a device whose resistance depends on previous input to the device and emulates the synapses in the brain. Many implementations of memristors [16-18] have only been able to replicate digital excitatory functionality of synapses, but the proposed material herein, $LiNbO_2$, can facilitate complementary analog memristance. That is, the material can be grown as either n or p-type (an unusual property for oxides) and have a corresponding analog resistance increase or decrease free of discontinuities due to an applied stimulus respectively as shown in Figure 4.9. The analog nature of $LiNbO_2$ memristors is demonstrated in Figure 4.10 where a sinusoidal input results in a continuously changing resistance response.

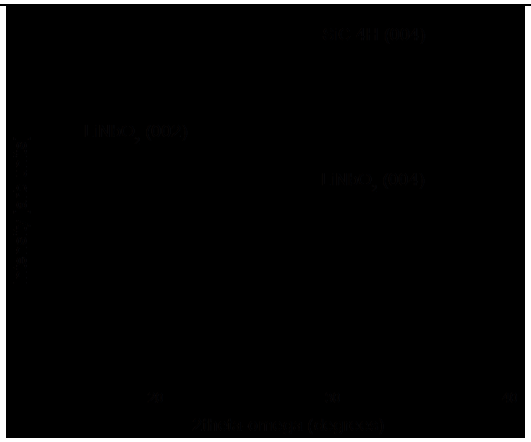

Figure 4.8: XRD data for an (002) $LiNbO_2$ layer grown on an (004) SiC substrate [7].

Figure 4.7: XRD data for an (002) $LiNbO_2$ layer grown on an (006) sapphire substrate [7].

The rapid lithium movement in $LiNbO_2$ memristors has been characterized by electrochemical impedance spectroscopy [19], which is a method used to determine the impedance response of a device with a small sinusoidal voltage applied at a range of frequencies. Figure 4.11 shows impedance spectroscopy data obtained from a frequency

range of 40 Hz to 10 MHz. The applied signal in the impedance data has a 5 mV amplitude. At low frequencies, lithium ions are able to track the applied sinusoidal voltage, and there is no phase offset. Thus the imaginary component of the impedance is low. At increasing frequencies, the lithium ions are no longer able to track the applied sinusoidal signal. This creates an offset between the applied signal and the resulting ionic current which is realized as an increase in the imaginary component of the impedance response. This offset reaches its climax at 6.6 MHz, and at higher frequencies, the imaginary component in the impedance data begins to decline. The physical mechanism behind this decline in the imaginary component of impedance is the frequency of the applied AC signal is so high that the ions no longer have a chance to respond, and thus the ionic current decreases.

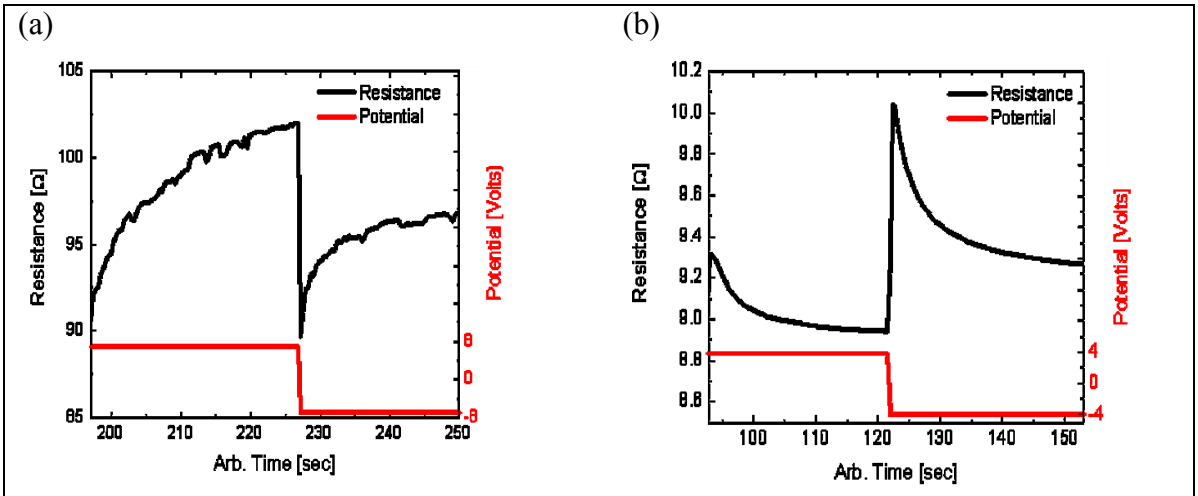

Figure 4.9: $LiNbO_2$ memristors demonstrate both n-type (left) and p-type (right) operation which allow memristances that have complementary behavior (increasing/decreasing resistance with applied voltage) [7]

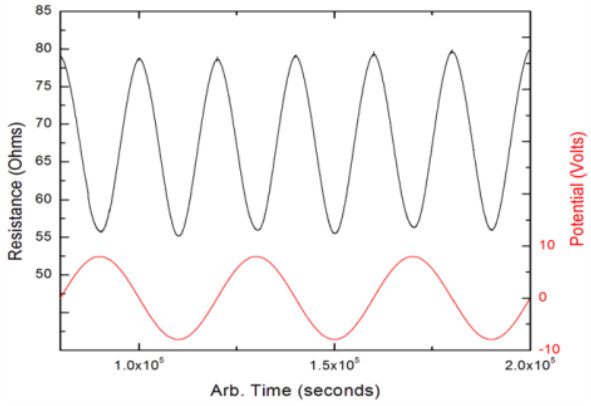

Figure 4.10: Resistance response of an $LiNbO_2$ memristor to a sinusoidal input voltage demonstrates continuous resistance changes for a large range of input voltages, proving analog operation [7].

An equivalent circuit based on the Randles model has been used to fit the impedance spectroscopy data [19]. The equivalent circuit consists of a resistor in series with a resistor and capacitor in parallel as shown in Figure 4.12. The first resistor in series (R1 in Figure 4.12) is theorized to represent the bulk electronic conductivity of the film. The bulk electronic conductivity is represented by R1 because this resistance is where the semicircular impedance response would cross the real axis if the measurement were taken to higher frequencies where the ionic contribution is negligible. At high frequencies, the impedance of the capacitor in the equivalent circuit approaches 0, and the lithium is no longer able to track the applied sinusoid. At this sufficiently high frequency, current is primarily electronic, i.e. due to electrons and holes and not ions. The resistor in parallel (R2 in Figure 4.12) represents the resistance due to the change in doping profile at the $LiNbO_2$-metal interfaces of the memristor, analogous to that of the charge transfer at the electrode interface in batteries [19]. The capacitor (C1 in Figure 4.12) represents the charge separation induced by the phase offset between the applied sinusoidal voltage and the resulting current. The capacitance value extracted from the fit

to the Nyquist data in Figure 4.11, 1.48 nF, indicates an equivalent ion current of 0.1 mA for the small drive voltage of 5 mV AC. This is approximately 87 A/cm^2 for the annular ring electrode device used herein, a remarkably high ion current density made possible by the single crystal nature of the epitaxial film.

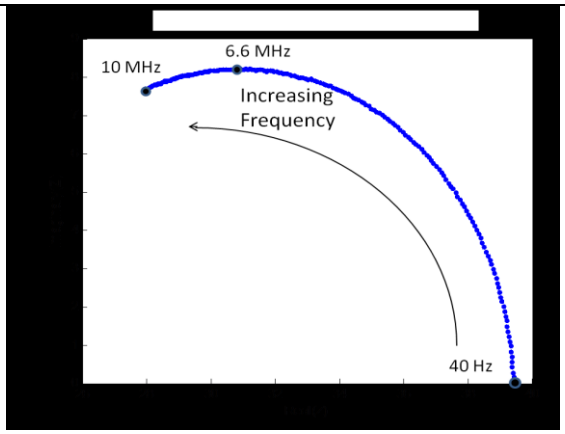

Figure 4.11: Impedance spectroscopy data for a $LiNbO_2$ memristor. An equivalent circuit is used to fit this data (Fig. 13) which breaks the memristor into discrete circuit elements [7].

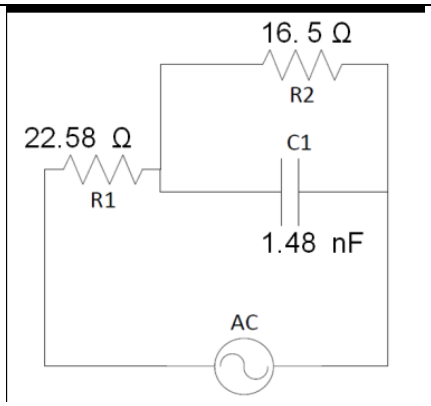

Figure 4.12: Equivalent circuit fit to impedance spectroscopy data taken from an $LiNbO_2$ memristor. R1 represents the bulk conductivity, R2 represents the interfacial resistance, and C1 represents the phase offset between the applied sinusoidal voltage and resulting current [7].

In comparison, $LiCoO_2$ batteries fit to the Randles equivalent circuit experience relaxation frequencies below 10 kHz [20] and charge transfer resistances of greater than

300 Ω [21] while $LiNbO_2$ electrodes exhibit relaxation frequencies around 6.6 MHz and charge transfer resistances of less than 20 Ω. This feature alone may make $LiNbO_2$ single crystal material useful for rapid charge/discharge battery applications, although it is important to remember that the $LiCoO_2$ measurements were done on a complete battery cell while the measurements described herein were completed on the $LiNbO_2$ cathode material alone.

4.6 Summary and Conclusions

We have developed and demonstrated a metal-halide growth chemistry implemented in a novel oxide MBE system that is capable of delivering transition metals using standard (and lower) MBE source temperatures. This technology allows one to deliver fluxes of low vapor pressure transition metals that were previously delivered in MBE using metal organics or a less thermally stable electron-beam source. The transition metals Nb, Co, Fe, and Ni have been epitaxially grown on (006) sapphire substrates using chloride precursors. The range of metals grown proves the versatility of the metal-halide growth chemistry. This list of epitaxial metals is by no means comprehensive, and any metal with a chloride precursor can be equivalently implemented.

In addition to epitaxial metals, the growth of epitaxial oxides has been demonstrated with the assistance of an oxygen plasma (PA-MBE). Epitaxial (006) $LiNbO_3$ has been demonstrated on both sapphire and SiC substrates with a full width at half-maximum XRD rocking curve of 150 arcseconds. Insulating $LiNbO_3$ is lattice matched to semiconducting $LiNbO_2$, and will be investigated in the future as a high- κ

dielectric for a transistor stack of the two materials. Epitaxial $LiNbO_2$ has also been demonstrated on both SiC and sapphire substrates with a best demonstrated FWHM XRD rocking curve of 190 arcseconds. Devices made from $LiNbO_2$ films show a memristive response due to the rapid motion of lithium in the crystal lattice. Because they exhibit a similar resistance response to synapses, $LiNbO_2$ memristors will be investigated in the future for computational architectures that seek to compute similarly to the human brain.

With the ability to grow both epitaxial metals and functional oxides using the same growth chemistry, multiple stacks of latticed-matched materials can be grown to keep pace with the increasingly complex electronic materials demands.

CHAPTER 5 : Liquid Phase Electro-Epitaxial Growth of $LiNbO_2$

5.1 Introduction

The MBE-based growth chemistry discussed in Chapter 4 is extremely versatile, and could result in some very fascinating heterostructures for use in ionic-electronic devices. However, its versatility and ability to produce multiple phases of materials requires exact control over each growth parameter is required if a single-phase growth is preferred. In attempts to provide a more repeatable growth method for $LiNbO_2$, a Liquid Phase Electro-Epitaxy (LPEE) growth chemistry was investigated.

Lithium intercalated transition metal oxides have played a critical role in the advancement of energy storage technologies [101]. Their layered structure facilitates the repeatable removal and replacement of lithium in the crystalline lattice. Although lithium removal results in minor lattice phase changes, no major crystal structural changes occur if the amount of lithium removed from the crystal is restricted. For example, 50% of the lithium can be reversibly removed from $LiCoO_2$ without phase change [102]. Thus, this material system, particularly $LiCoO_2$ and related compounds, has been an area of intense research for battery applications.

Not all lithium intercalated layered transition metal oxides have received the same level of interest. A layered sub-oxide of $LiNbO_3$, $LiNbO_2$, has been minimally investigated. Although $LiCoO_2$ and $LiNbO_2$ are both layered transition metal oxides, $LiCoO_2$ is of the $R\bar{3}m$ space group and $LiNbO_2$ is of the $P6_3/mmc$ space group [103, 104]. This difference in crystal structure results in dramatically different electrical

behavior. $LiCoO_2$ is electronically resistive exhibiting room temperature resistivity of over 10^{11} ohm-cm yet allows for ion conduction [105]. Contrarily, $LiNbO_2$ was first synthesized by researchers attempting to create $Li_4Nb_3O_8$[27] and later investigated for its ionic [28, 29], superconducting [30, 31, 35], and memristive properties [85, 93]. The ionic properties of $LiNbO_2$ were investigated in an electrochemical battery cell and through nuclear magnetic resonance (NMR) investigations [29, 31]. It was determined that $LiNbO_2$ can reversibly cycle lithium in the crystal structure and is superconducting with a T_c of 5.5 K [29, 31, 35]. Additionally, $LiNbO_2$-based devices were shown to exhibit memristive, meminductive, and memcapacitive responses [93].

Memristive devices were originally theorized by Chua in 1971, with both meminductive and memcapacitive devices being later theorized [5, 92]. The first memristive device claiming the implementation of Chua's theorized device utilized a TiO_2 layer deposited between two Pt metal electrodes [6]. The memristive response of the TiO_2-based memristor depends on the creation and destruction of a conductive filament [20]. In contrast to the first memristive devices, $LiNbO_2$-based memristors utilize the movement of lithium and the resulting creation and destruction of electronic states [85]. Lithium motion in $LiNbO_2$-based memristors is an analog (continuum of resistance values) process which is important for neuromorphic computing architectures that seek to compute similar to the mammalian brain with an interconnect of emulated synapses and neurons [85].

Initially, $LiNbO_2$ was synthesized using a mixture of powders of Li_2O and NbO_2. This reaction yields $LiNbO_2$, $LiNbO_3$, and Li_3NbO_4 [27]. Single phase $LiNbO_2$ was later synthesized using a mixture of Li_3NbO_4 and NbO powders [29]. Subsequently, single

crystals of $LiNbO_2$ were synthesized by the electrolytic reduction of fused salts where a mixture of $NaBO_2$, LiF, $LiBO_2$, and Nb_2O_5 was used [34, 35]. Finally, thin films of epitaxial $LiNbO_2$ were grown by molecular beam epitaxy using an oxy-halide growth chemistry using Li, $NbCl_5$, and O as growth constituents [7, 39]. In the present study, a method for the growth of $LiNbO_2$ crystals by an electrolytic reduction method, liquid phase electro-epitaxy (LPEE) is introduced. Liquid phase electro-epitaxy is a method used to grow crystals that utilizes an electric current to initiate and sustain layer growth. The electric current used in LPEE facilitates the electro-migration of the growth constituents to the substrate and allows for the formation of sub-oxides without the need for vacuum environments common to all previous implementations [106]. The method described herein differs from previous electrolytic reduction methods by using fewer growth constituents, and thus reducing the number of contaminants in the resulting $LiNbO_2$ crystals. The deposited crystals were investigated by X-ray diffractometry, X-ray photoelectron spectroscopy, and secondary ion mass spectrometry (SIMS).

5.1 Experimental Procedures

$LiNbO_2$ crystals were grown using an electrolytic reduction method in a $LiBO_2$ (99.9%) flux. The flux allows Nb_2O_5, which has a high melting point of 1530° C, to become molten at readily achievable growth temperatures below 1000° C. Compared to previously used flux constituents, the LPEE-based growth method presented herein include only Nb_2O_5 (99.9%) and $LiBO_2$ (99.9%), a marked change from previous methods used to grow crystalline $LiNbO_2$, which include both $NaBO_2$ and LiF as part of

the growth constituent makeup. The molar ratio of $LiBO_2$ to Nb_2O_5 used was 15 : 1 and is similar to the chemistry used in the growth of $LiTiO_2$ [107].

A nitrogen glove box environment was used throughout the growth of $LiNbO_2$ crystals, and the humidity and temperature of the glove box were measured using an Omega Engineering iTHX-SD. For all experiments, the humidity was measured at 0.0% (lower than the resolution of the measuring apparatus) while the temperature in the glovebox was less than 60° C. A cylindrical graphite crucible (ID = 1.42", height = 3.06") was used as the anode and Nb foil or crystalline SiC electrodes were used as the cathode. The graphite crucibles were first cleaned with trichloroethylene, acetone, and methanol. After cleaning, the crucibles were baked out at 1050° C for 30 minutes before use. After baking the crucible, $LiBO_2$ and Nb_2O_5 powders were mixed and melted at 910° C for 30 minutes. The temperature of the furnace was then lowered to 900° C. After the furnace temperature stabilized at 900° C for 30 minutes, the Nb foil (or SiC) electrode was lowered into the melt, and a constant positive potential was applied across the electrodes. Potentiostatic control was used to achieve a constant composition and oxidation state of the $LiNbO_2$ crystals [108]. Voltages used during the deposition were 1.1 V and 1.8 V for Nb and SiC cathodes respectively. Different voltages are required by the Nb and SiC cathodes due to differences in the electrochemical voltages between the graphite anode and the respective cathode in the borate electrolytic flux. After cooling, The $LiNbO_2$ crystals were separated from the borate flux using ultrasonification in a water bath at room temperature.

The surface morphology of the $LiNbO_2$ crystals was characterized by atomic force microscopy (AFM, Veeco AFM). X-ray Photoelectron Spectroscopy (Thermo K-

alpha XPS) and secondary ion mass spectrometry (IONTOF Time-of-Flight SIMS) were used to determine relative chemical composition, and the crystal structure was examined using a Phillips Xpert MRD X-ray Diffraction system. Electrical characterization of the memristors fabricated using the LPEE-deposited $LiNbO_2$ crystals was performed using a Keithley 2400 source meter.

5.3 Results and Discussion

Figure 5.1: Image of typical self-nucleated $LiNbO_2$ crystals measuring from 1.0 to 2.0 cm (left to right) laterally.

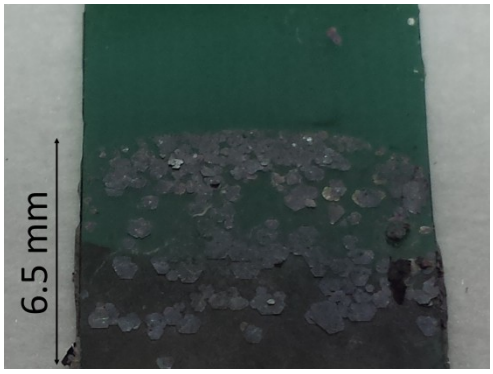

Figure 5.2: Image of $LiNbO_2$ crystals grown on a crystalline SiC substrate.

The growth of both bulk crystals and seeded thin films were attempted. Very large plate-like $LiNbO_2$ crystals attached to the niobium foil cathode were evident after etching the borate flux in water. Figure 5.1 shows as-grown $LiNbO_2$ crystals with lateral dimensions up to 2.0 cm while Figure 5.2 shows as-grown $LiNbO_2$ crystals seeded on a SiC substrate after 10 minutes of growth. Attempts at thicker seeded growths were hampered by the loss of epitaxial crystalline alignment, possibly due to the very high growth rates used herein. The thicknesses of the as-grown self-nucleated crystals were about 250 μm for growths lasting 26.7 hours. The thickness of the crystals grown on the seeded SiC for only 10 minutes were between 5 and 9 um. Although the samples are rough to the naked eye and macroscopic step edges are present in the crystals, the flat portions of the crystals, typically ~1-10 μm wide, are very smooth as shown in the AFM data in Figure 5.3 with an RMS roughness of the $LiNbO_2$ crystal of 1.67 nm. This flat microstructure likely results from the inherent layered crystal structure of $LiNbO_2$.

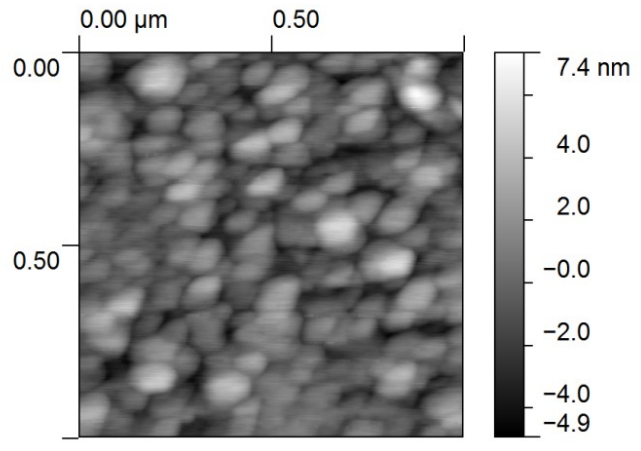

Figure 5.3: AFM image of LPEE grown $LiNbO_2$. As-grown crystals have macroscopic steps and smooth areas with an RMS roughness of 1.67 nm.

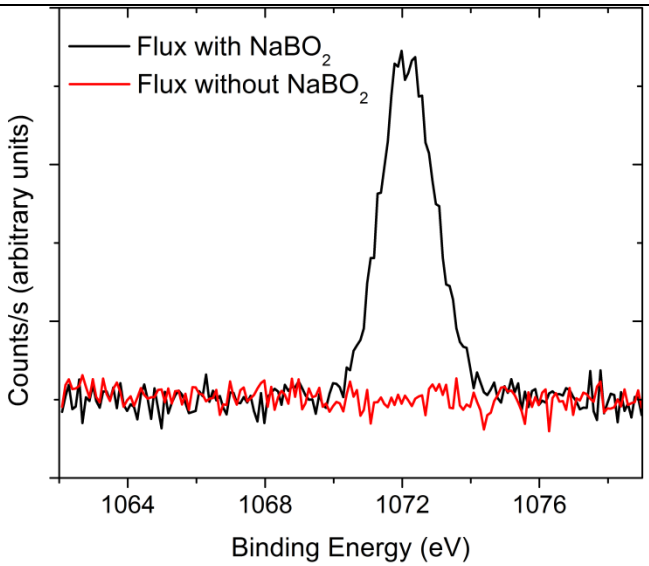

Figure 5.4: XPS spectra of $LiNbO_2$ crystals grown with and without a sodium bearing flux. The Na-containing flux results in the unwanted incorporation of Na into the crystalline lattice.

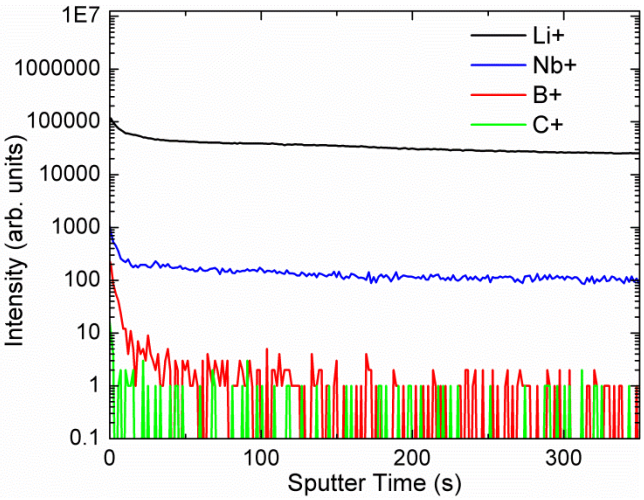

Figure 5.5: SIMS depth profile of a LPEE-grown $LiNbO_2$ crystal. C and B are detected on the surface but not in the bulk of the crystal.

The $LiNbO_2$ crystals grown using the method described herein have minimal contamination as demonstrated by XPS and SIMS. The XPS spectra shown in Figure 5.4

indicate that the crystals contain no Na impurities within the detection limits of XPS. Contrarily, as shown in the XPS data of figure 5.4, crystals grown with a flux including $NaBO_2$ and LiF exhibit Na contamination. $NaNbO_2$ is energetically favorable to form in this chemistry and thus, it is preferable if contamination is to be avoided, to use a flux without elements that can readily incorporate into the crystal [109, 110]. Crystals grown from a LiF and $NaBO_2$-containing flux contain 9.2 atomic % of Na and 4.4 atomic % of F as determined by XPS.

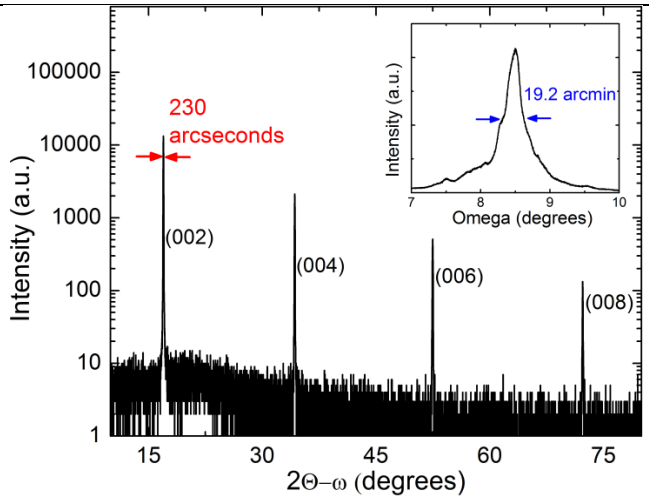

Figure 5.6: XRD double crystal diffraction scan and XRD rocking curve (inset) showing the single orientation and single phase of an LPEE-grown freestanding $LiNbO_2$ crystal.

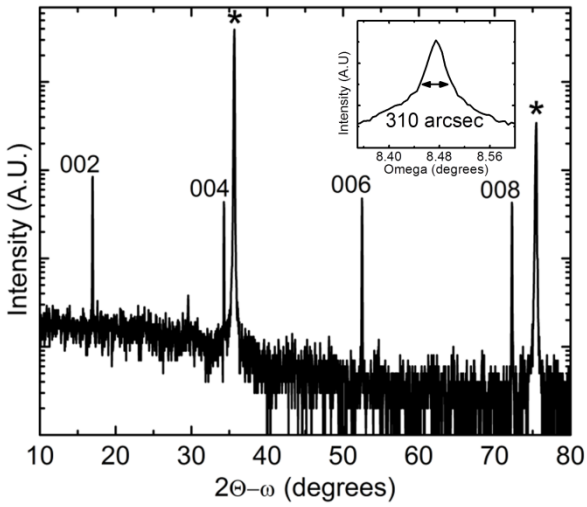

Figure 5.7: XRD double crystal diffraction scan where LiNbO2 peaks are labeled and *-labeled peaks are from the c-axis oriented SiC substrate. The XRD rocking curve (inset) is also included. The seeded LPEE growth of LiNbO2 results in a single orientation and single phase $LiNbO_2$ crystal.

Removing the possible sources of Na contamination leaves B and C as other possible contaminants from the boron-containing flux and the graphite crucible respectively. These contaminants were not observed in XPS so they were investigated using SIMS and, as shown in Figure 5.5. After sputtering the surface of the $LiNbO_2$ crystal, the intensity of the B and C signals drop below the detection limit.

In addition to having smooth surfaces and undetectable levels of contaminants, the LPEE-grown $LiNbO_2$ crystals are of high quality structurally. As shown by the XRD symmetric scan in Figure 5.5, the full-width at half-maximum for the double crystal diffraction scan (two-theta omega scan) is 230 arcseconds, indicating a high level of c-spacing uniformity in the LPEE-grown $LiNbO_2$ crystals. Furthermore, only the (000X) peaks are detected in the double crystal diffraction scan, indicating that the crystals are both single phase and contain only one orientation. The rocking curve for a unseeded

free-standing LPEE-grown $LiNbO_2$ crystal is shown in the inset of Figure 5.6, with a FWHM of 19.2 arcmin.

In attempts to provide seeded growth, $LiNbO_2$ has also been grown on SiC using the LPEE method. 6H SiC has a lattice constant of 3.07 Å is similar (%5.3) to $LiNbO_2$ at 2.905 Å [104, 111]. The symmetric XRD double crystal diffractogram for $LiNbO_2$ grown heteroepitaxially on SiC is shown in Figure 5.7. (0001) oriented $LiNbO_2$ grows on (0001) oriented SiC and is consistent with previous reports of heteroepitaxial growth of $LiNbO_2$ on SiC performed by molecular beam epitaxy [7, 39]. The seeded growth of $LiNbO_2$ on SiC results in an improved crystal quality as shown in the inset of Figure 5.6 but unfortunately does not result in planar coalesced films. The full width at half-maximum of the XRD rocking curve is 310 arcsec, a marked decrease compared to the freestanding EELPE-deposited $LiNbO_2$ crystals.

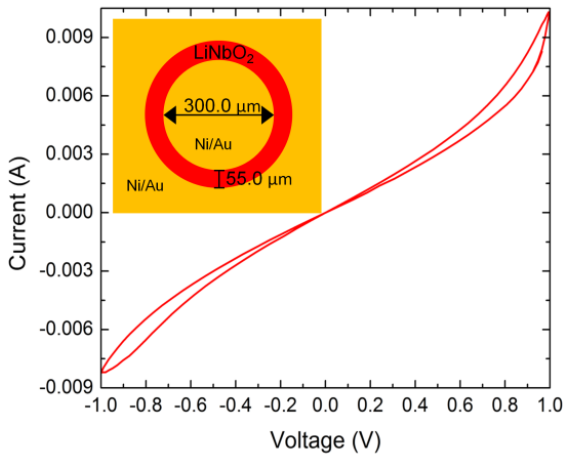

Figure 5.8: Characteristic memristive I-V hysteresis loop for an LPEE-grown $LiNbO_2$ memristor. (inset) The device structure consists of an annular geometry with an Ni/Au metal stack.

After the chemical purity and structural quality of the LPEE-grown $LiNbO_2$ were confirmed, electrodes were deposited onto the surface to electrically characterize the memristive properties of the $LiNbO_2$. Unlike most other published memristors, $LiNbO_2$ is memristive even at large geometries due to the ease of motion of the Li and the impact Li-vacancies have on electronic properties [85]. An annular electrode pattern was used to confine ionic motion as shown as an inset in Figure 5.8. The inner dot of the structure has a diameter of 300 micrometers while the spacing between the inner dot and outer ring is 55 microns. The I-V curve of the memristive device is shown in Figure 5.7. Hysteresis is present in the I-V curve indicating that the memristor exhibits memory, although it is short term memory and thus a volatile device [85]. Volatile memristors have been shown to mimic the ion channel conductances of a neuron and thus have important applications in neuromorphic computing [112, 113].

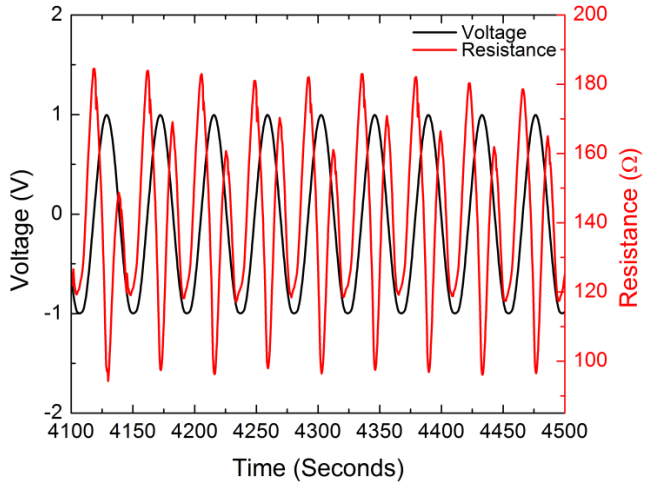

Figure 5.9: The resistance response of an LPEE-grown $LiNbO_2$ memristor under the application of a 25 mHz sinusoidal voltage.

The volatility of the $LiNbO_2$ memristor is due to the underlying memristance mechanism and was first exhibited on MBE-grown $LiNbO_2$ memristors [93]. As lithium is drifted in the $LiNbO_2$ crystalline lattice under the application of an applied voltage, lithium vacancies are created at the positively biased anode and destroyed at the grounded cathode. Lithium vacancies act as electronic acceptors, so the applied bias results in a redistribution of the doping profile in the $LiNbO_2$ memristor. This change in doping profile results in the memristance response in $LiNbO_2$-based devices [7, 85, 93, 114].

The resistance response of an LPEE-grown $LiNbO_2$ memristor under the application of an AC sinusoidal voltage with a frequency of 25 mHz is shown in Figure 5.9. The device structure of the volatile analog memristor is shown in Figure 5.8. The asymmetry of the device contacts and interfacial area results in different amounts of lithium accumulated at each of the contacts as the polarity of the applied bias is differed, which has been investigated both theoretically and experimentally [93, 114]. Because the amount of lithium accumulated at each contact is different, the resistance changes on the rising and falling edges of the applied sinusoidal voltage also vary.

5.4 Conclusions

In conclusion, the LPEE growth of $LiNbO_2$ crystals is demonstrated to be a promising synthesis method for future neuromorphic computing applications. Compared to previously utilized chemistries, which include $NaBO_2$, the growth chemistry demonstrated herein can synthesize crystalline $LiNbO_2$ without Na contamination. By using only Nb_2O_5 and $LiBO_2$ as growth constituents, self-nucleated bulk and SiC-seeded $LiNbO_2$ crystals have been synthesized. The material grown in this research shows

promise for future ionic-electronic devices including the volatile memristor demonstrated herein.

CHAPTER 6 : In Situ Investigation of the Channel Conductance of a $Li_{1-x}CoO_2$ ($0 < x < 0.5$) Ionic-Electronic Transistor

6.1 Introduction

Presently, the majority of neuromorphic computing implementations utilize either digital or analog silicon devices to emulate biological phenomena resulting from the movement of ionic species in the brain [21, 115]. Because the neuromorphic computing architecture seeks to compute using low-powered devices inspired by biological neurons and synapses, a more natural neuromorphic realization would utilize engineered ionic-electronic devices.

Devices that exploit the interaction between ionic and electronic properties of materials have been investigated for decades. Early research in this area was conducted by fabricating a traditional metal-oxide-semiconductor field effect transistor (MOSFET) without a gate metal [116]. Upon submerging the MOSFET device into an ion-containing aqueous solution, a double layer of charge builds on the solution-oxide interface which interacts with the built-in oxide-silicon double layer thereby modulating channel charge. More recently, ion-gated thin-film organic transistors were demonstrated to improve upon the specific capacitance of traditional organic transistors through the use of an ionic double layer capacitance [117, 118].

Despite decades of research on devices that exploit the interaction between ions and electrons, the feasibility of using battery materials in ionic-electronic devices has received minimal investigation. The conductivity of $LiCoO_2$, a common battery cathode

material, has been shown to change as a function of lithium content in the layered structure of sintered powder pellets, and the extraction and reinsertion of lithium into the material is reversible [119-121]. This change in conductivity, however, has only been studied *ex situ*, so the analog nature of the resistance change in $LiCoO_2$ as a function of lithium has yet to be investigated.

It is important to understand the resistance response of $LiCoO_2$ as a function of lithium content because $LiCoO_2$ could have important neuromorphic computing and memory applications. Like synapses and neurons in the brain, ionic-electronic devices based on $LiCoO_2$ operate by controlling the movement of ions. Ionic electronic transistors based on $LiCoO_2$ thin films are expected to satisfy the neuromorphic computing low-power requirement. Contrarily, devices that rely on an ionic-electronic double layer of charge to induce an electric field in the channel of a transistor operate in an inherently power-intensive operation regime because a constant bias must be applied to modulate the channel conductivity. The channel of the ionic-electronic transistor demonstrated herein modulates conductivity by the intercalation and deintercalation of lithium providing for a static channel resistance change without a DC gate bias. Charge compensation in lithium deficient $LiCoO_2$ creates electronic holes, increasing the conductivity of the material [87, 122, 123]. This hole formation mechanism has also been shown in thin-film RF (radio frequency) sputter deposited $LiCoO_2$-based batteries [124]. Because no power is required to maintain the deintercalated lithium ions near the gate electrode and thus modulate the conductivity of the channel of the transistor, this regime for ionic-electronic transistor operation is inherently low power.

A three-terminal ion-intercalated device termed a memistor, similar to that presented herein, has been demonstrated that uses a thin film stack of WO_3, SiO, and Cr_2O_3 [67]. The conductivity of the WO_3 layer changes as a function of the amount of H^+ injected from the Cr_2O_3 layer. The SiO layer acts as an electron blocking layer and decreases the volatility of the memistor. Unfortunately, after approximately 25 cycles, the reversibility of the memistor deteriorates significantly due to the repeated formation and dissolution of hydrogen gas which ultimately ruptures the aluminum gate electrode [67].

In contrast, thin film batteries utilizing RF Sputtered $LiCoO_2$ cathodes have shown good capacity retention (about .0003% capacity loss per cycle) after thousands of cycles when discharged to ~$Li_{0.5}CoO_2$ [94, 125-127]. Furthermore, when discharging beyond 50%, (Li_xCoO_2 where $x < .5$), thin film batteries utilizing RF sputtered thin film $LiCoO_2$ cathodes exhibit less than a .02% capacity loss per cycle which is significantly better than traditional composite powder cathodes [128]. Lithium insertion and removal results in a resistance change in the ionic-electronic transistor channel, and thus the repeatability of the resistance change will be dependent on the capacity loss as the $LiCoO_2$ thin film is cycled. Because the capacity loss in batteries that utilize RF sputtered $LiCoO_2$ thin film cathodes is minimal, RF sputtered $LiCoO_2$ is an ideal candidate for robust three terminal ionic-electronic transistors.

6.2 Experimental Setup

A schematic of a $LiCoO_2$ ionic-electronic transistor is shown in Figure 6.1. The as-grown device schematic is shown in Figure 6.1(a) and an electrochemically deintercalated ionic-electronic transistor schematic is shown in Figure 6.1(b). As a positive bias is applied on the electrode submerged in electrolyte, lithium ions are driven

through the electrolyte and deposit on the gate metal, thus operating in a similar fashion to lithium-ion batteries. The removal of lithium from the $LiCoO_2$ material results in a more conductive channel through Li-vacancy acceptor compensation similar to other lithium intercalated transition metal oxides [85, 129, 130]. As in a lithium battery, once lithium is removed from the $LiCoO_2$ in the ionic-electronic transistor channel described herein, no power is required to keep the deintercalated lithium separated from the $LiCoO_2$. Hence, the $LiCoO_2$ based ionic-electronic transistor has a distinct advantage over traditional MOSFETS and other ionic-electronic transistors because the $LiCoO_2$-based transistor does not require power to maintain a certain channel conductance.

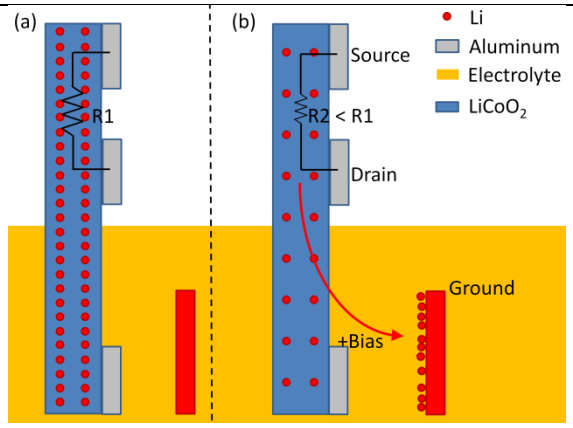

Figure 6.1: Schematic illustration of the $LiCoO_2$-based ionic-electronic transistor. Initially, the $LiCoO_2$ is fully lithiated resulting in a resistive channel between the source and drain (a). As lithium is electrochemically removed, the channel resistance decreases as lithium vacancies, acceptors, are created (b).

The $LiCoO_2$ ionic-electronic transistor material was deposited using an RF-sputterer on a 1 cm x 1 cm c-axis oriented sapphire substrate that was cut in half after deposition. The deposition parameters used were 150.0 Watts of RF power at 10.0 mTorr of pressure with an $Ar:O_2$ mix of 45:5 and adapted from previous research [126, 131].

After deposition, the film was annealed in an O_2 environment for 2 hours at 700° C. Raman Spectroscopy was performed on the sample to confirm the high-temperature phase of $LiCoO_2$ as shown in Figure 6.2. The characteristic E_g and A_{1g} Raman bands for high temperature $LiCoO_2$ are located at 486 cm^{-1} and 596 cm^{-1} respectively [132]. Electrochemical measurements were carried out with an Arbin BT2000 on an electrochemical cell with lithium reference and counter electrodes. The $LiCoO_2$ conductivity measurements were carried out with a Solartron 1287. This deposition method is known to produce columnar polycrystalline films and as such the change in resistance could be limited by shunting grain boundary conduction [94, 105].

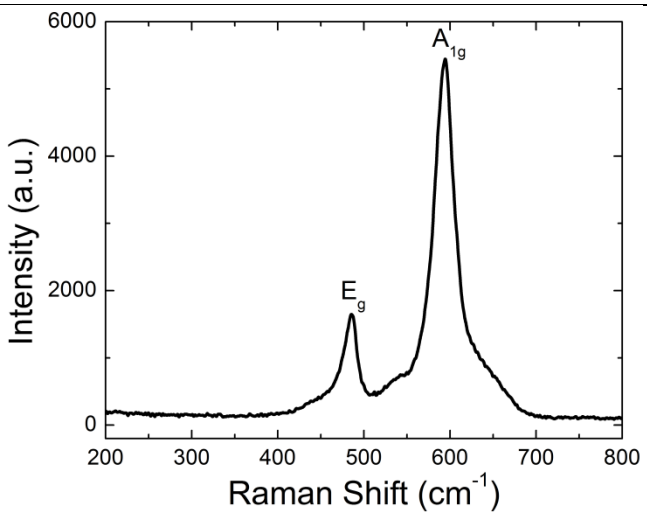

Figure 6.2: Raman spectrum of the sputtered thin film $LiCoO_2$ thin film used in the ionic-electronic transistor. The characteristic E_g and A_{1g} Raman bands for high temperature $LiCoO_2$ are located at 486 cm^{-1} and 596 cm^{-1} respectively.

A schematic for the experimental setup is shown in Figure 6.1. Approximately 3.5 mm of the $LiCoO_2$ thin film was submerged in the liquid electrolyte while the conductivity was measured on the top of the film which was not exposed to the electrolyte. This experimental setup was used to avoid measuring both ionic and

electronic conductivity, which would have been the case if the entire sample were submerged. The drawbacks of this approach are the large dimensions and the resulting slow temporal response. This experiment is a proof of viability and future nanoscale neuromorphic devices will have a faster temporal response.

6.3 Ionic-Electronic Transistor Operation

The operation of the ionic-electronic transistor presented herein can be separated into two different sections: an electrochemical gating mechanism similar to a microbattery and the ionic-electronic transistor channel that exhibits an electronic conductivity change based on the concentration of lithium in the $LiCoO_2$ [90, 126]. The electrochemical mechanism occurs in the lower part of the $LiCoO_2$ thin film emerged in an electrolyte consisting of equimolar ethylene carbonate and dimethyl carbonate with 1M $LiPF_6$ salt (Novolyte), while the electronic section consists of two aluminum parallel electrodes deposited at the top of the film not in contact with the electrolyte [133]. While drift fields dominate the insertion and extraction of Li from and to the electrolyte, Li diffusion dominates the ionic conductivity of the region between the two ionic-electronic transistor channel parallel electrodes. The linear arrangement of contacts prevented the delithiation current from adding to the current across the unsubmerged contacts. This enables the measurement of conductivity while simultaneously removing lithium from the entire film through the submerged electrode.

Lithium in the electrochemical section of the ionic-electronic transistor was intercalated and deintercalated from the $LiCoO_2$ thin film by varying the electrochemical cell voltage between the $LiCoO_2$ thin film and a lithium electrode as shown in Figures 6.3 and 6.4. Voltage steps are applied as shown in Figures 6.3 and 6.4. In between the

voltage steps, the open circuit voltage of the battery cell was monitored for 600 seconds to ensure charging/discharging. Thus, the electrochemical cell voltages in Figures 6.3 and 6.4 are the applied voltages when the voltage is being applied to the microbattery and measured open circuit voltage otherwise (at the end of each voltage step). During the experiment shown in Figure 6.3, approximately 50% of the lithium was removed while the material contains approximately stoichiometric levels of lithium at the end of the lithiation experiment shown in Figure 6.4. The electronic conductivity of the $LiCoO_2$ thin film was monitored at the top of the film between two Al electrodes 0.3 mm apart, i.e. the ionic-electronic transistor channel. Initially, the resistance of the channel was 4.9 MΩ. A 5 mHz 1.0 V (peak to peak) triangle wave centered about 0 V was applied across the electrodes and the resulting current, which was used to calculate the resistance of the ionic-electronic transistor channel, was monitored every 2 seconds. Previous measurements on $LiCoO_2$ thin films with this small electric field indicated negligible conductivity change due to the drift of lithium in the memristive portion of the device implying all changes are due to the diffusion of Li to/from the electrochemical battery section. The linearity of the I-V curve shown in the inset of Figure 6.3 recorded during the relithiation of the $LiCoO_2$ thin film using a 1 V peak-to peak triangular wave confirms that the conductivity of the channel does not change due to the negligible electric field of the sensing voltage. The representative I-V curve shown in the inset of Figure 6.3 was measured 2.76×10^5 seconds into the relithiation experiment. Figures 6.3 and 6.4 show the electronic resistance during the same time period as the electrochemical voltage.

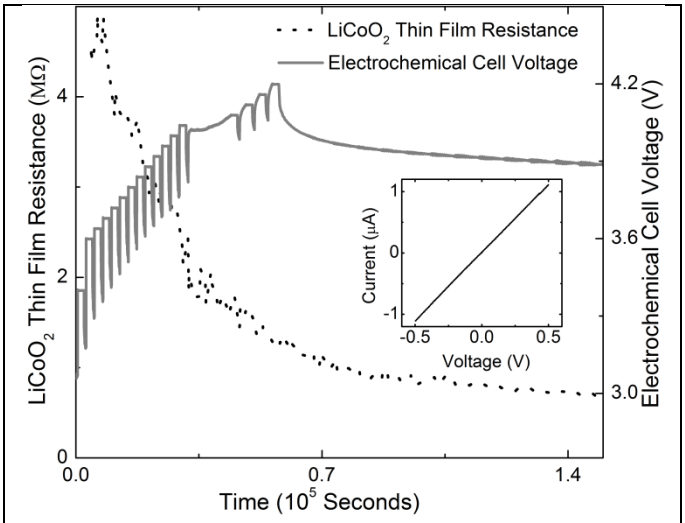

Figure 6.3: The resistance of a sputtered LiCoO2 thin film as it is being delithiated. As lithium is removed from LiCoO2, lithium vacancies which act as acceptors are created which decrease the resistance of the device channel. The inset shows a representative I-V curve of the ionic-electronic transistor channel.

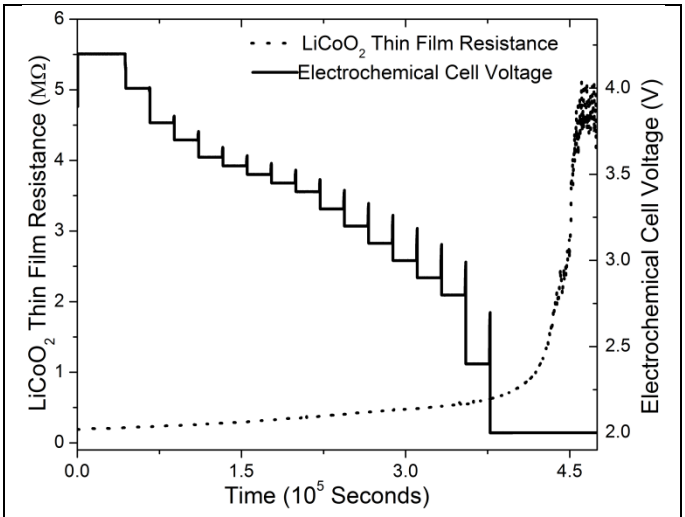

Figure 6.4: The resistance of a sputtered $LiCoO_2$ thin film as it is being lithiated. As the electrochemical cell voltage is lowered, $LiCoO_2$ is lithiated. This lithiation results in lithium vacancies being filled and the resistance of the device channel increases.

As shown in Figures 6.3 and 6.4, when lithium is removed from the material, the conductivity of the device increases by approximately an order of magnitude as approximately half of the lithium in the material is removed, and as lithium is replaced in the material, the conductivity of the device decreases by approximately an order of magnitude. This change is most dramatic at the beginning of the deintercalation or the end of the intercalation, which is consistent with previously reported *ex situ* conductivity measurements on $LiCoO_2$ as a function of lithium content [119, 134]. This dramatic change in conductivity as small amounts of lithium are removed from the fully lithiated $LiCoO_2$, or when added to a slightly lithium deficient material, have been previously attributed to the change in doping levels as lithium vacancies are created and filled whereas resistance changes due to excessive Li intercalation/deintercalation can result from structural changes. Unlike a battery, a $LiCoO_2$-based ionic-electronic transistor can operate with minimal amount of Li intercalation/deintercalation. This minimal amount of intercalation/deintercalation should increase the reliability lifetime dramatically longer than in a typical battery application because it will avoid the two-phase domain present in Li_xCoO_2 for $0.78<x<0.9$ [135]. Additionally, the sensitivity of the resistance change to Li content is highest and thus the device is most responsive at near stoichiometric Li concentrations.

Upon the initial deintercalation of lithium, voltage steps were applied between the $LiCoO_2$ thin film and the lithium electrode as shown in Figure 6.3 to slowly deintercalate lithium from the portion of the sample immersed in electrolyte. After applying 4.2 V, at 0.58×10^5 seconds, the electrochemical open circuit voltage and the ionic-electronic

channel resistance were simultaneously monitored to confirm that the channel resistance would not revert back to its initial resistance while there is no electrochemical gate voltage applied to the ionic-electronic transistor. The ability to maintain an analog state without an applied voltage should enable low-power neuromorphic operation. To realize an electronic change at the top of the sample where the electrical resistance was being monitored it was necessary for lithium ions from that part of the device to diffuse down to the portion of the device immersed in the electrolyte. Because of this lengthy diffusion path, there is an expected lag between the electrochemical and the electronic response in the $LiCoO_2$-based ionic-electronic transistor, causing a seemingly lengthy timescale. The initial drop in the electrochemical open circuit voltage after 0.58×10^5 s is due to the equilibration of lithium in the $LiCoO_2$ thin film and demonstrates this lengthy diffusion path. Faster temporal response can be achieved by scaling down the geometry of the $LiCoO_2$-based ionic-electronic transistor several orders of magnitude, undoubtedly increasing the resistance response and decreasing this diffusion length dramatically.

6.2 Conclusions

Several important discoveries have been made about the operation of an ionic-electronic transistor based on $LiCoO_2$. Primarily, the device should be optimally operated between the fully lithiated and ~10% delithiated levels. It was shown that the largest resistance change occurs at the initial deintercalation and final intercalation which agrees with previous investigations on the conductivity of $LiCoO_2$ as a function of lithium content. It was further discovered herein that this resistance change was not completely abrupt, and there is a sharp but continuous resistance response for $LiCoO_2$ in this lithium range, a finding that has not been previously shown since all electrical characterization

was performed *ex situ*. This finding has important device design implications for both neuromorphic computing and memory applications.

Although it is possible to implement neuromorphic computing elements using digital devices [136], devices to be used in neuromorphic computing architectures are more naturally implemented with analog devices. Analog devices are more applicable because the synapses and neurons in the brain are analog in nature [137].

A second possible application for this sharp but smooth resistance change investigated herein is in memory. Because there is a continuous resistance change that spans close to an order of magnitude, multiple bits could be stored using one three-terminal $LiCoO_2$ ionic-electronic transistor. Additionally, only a small amount (<10%) of lithium needs to be extracted to see the majority of this large change in conductivity of the material, so with smaller devices, little current extraction would be required to modulate the conductivity of the $LiCoO_2$ ionic-electronic transistor.

In conclusion, the ionic electronic response of $LiCoO_2$ is investigated by an ionic transistor structure. As lithium is removed and replaced into $LiCoO_2$, the resistance of the material changes in an analog nature, facilitating the use of ionic electronic devices based on $LiCoO_2$ for both neuromorphic computing and memory applications.

CHAPTER 7 : Radiation Effects on $LiNbO_2$ Memristors

7.1 Introduction

Neuromorphic computing is a promising field of research that has driven a wide variety of innovators of computational devices for the last century [21, 68, 69]. Neuromorphic computing is a biologically-inspired computational architecture that seeks to compute similarly to the brain with a network of low-power synapses and neurons and is valued for its robustness and minimal power consumption. For example, the loss of a few neurons in a mammalian brain leads to minimal loss of functionality making neuromorphic architectures attractive for harsh environments [21]. The neuromorphic computing architecture is a proposed solution to replace present-day computing devices which will begin to approach performance limits due to excess heat and power consumption [2].

The memristor, originally theorized by Chua [5], is a key enabling device for neuromorphic computing because it is able to replicate two of the main computational elements in the mammalian brain, the synapses and neurons [59, 112]. The memristor is the 4^{th} 2-terminal passive circuit element and complements resistors, capacitors, and inductors by relating flux-linkage to electric charge [5].

Currently, most memristive devices operate by creating and destroying a highly conductive filament. The first filamentary memristive device claimed was a TiO_2-based device, but filamentary memristors have been implemented using many different transition metal oxides and nitrides including CeO_x, Nb_2O_5, NiO, $Pr_{0.7}Ca_{0.3}MnO_3$, Al_2O_3, $SrTiO_x$, and

AlN, amongst others [14, 15, 17, 42, 43, 45, 138, 139]. The device structure for the majority of digital memristors includes a metal/oxide/metal stack where a conductive filament is reversibly created and destroyed with an applied bias [140]. This conductive nanoscopic filament is formed by the movement of oxygen or nitrogen ions which form a highly conductive sub-stoichiometric filament. The highly conductive filament then shorts out the two metal electrodes of the digital memristor and thus, results in a dramatic change in resistance. Filamentary memristors also can be operated as nano-batteries [141]. Observation of this filamentary behavior has been confirmed with transmission electron microscopy, atomic force microscopy, and infrared measurements [20, 48, 50]. In TiO_2-based filamentary memristors, intense Joule heating of around 665 K facilitates the rapid movement of oxygen, which creates a sub-oxide filament [142]. Unfortunately, this filamentary behavior results in devices that are inherently power-intensive. Filamentary memristors that exhibit analog properties, such as those based on TaO_x, require external current compliance circuitry to achieve analog states and voltages over a certain threshold to modulate the memristor's resistance state [143].

Neuromorphic implementations utilizing filamentary memristors attempt to replicate the analog nature of biological synapses through the use of complex timing schemes [84, 144]. This multi-memristor filamentary operation is not biologically-realistic, but can emulate a stepped variation of resistances. Filamentary memristors can be operated as analog devices, but the compliance current, and thus the power (I^2R) supplied to facilitate Joule heating, must be controlled, which requires additional external circuitry [143]. By designing a neuromorphic architecture using analog memristors to mimic mammalian synapses, more compact biologically-realistic computation can be achieved.

Analog memristors have continuously variable resistances that change with the applied voltage magnitude and the applied voltage duration. Computation in this architecture is performed by changing the conductance of memristive synapses based on the temporal duration and magnitude of the applied stimulus. Such analog memristors have been reported in an organic implementation and in $LiNbO_2$-based memristors [63, 85].

In previous work, the effects of radiation on digital memristive TiO_2-based devices have been investigated with a Monte Carlo simulation, and it was determined that protons and heavy ions can dramatically affect memristance performance. Specifically, oxygen vacancies induced by radiation result in a decrease in resistance, and displaced interstitial titanium and oxygen ions can reduce the mobility of oxygen vacancies. The effects of these two results on the I-V curve are two-fold. The decrease in resistance from the radiation-induced oxygen vacancies results in a counter-clockwise shift in the I-V curve, and the reduced oxygen mobility from the displaced ions results in a closing of the hysteresis loop in the I-V curve [145, 146].

Radiation effects on digital memristors have also been experimentally investigated. Proton irradiation introduces defects into TiO_2-based memristors, which increase the conductivity of the digital TiO_2-based memristors in the "off" state [145-147]. Additionally, proton irradiation caused significant variation in operating voltages and resistance values after doses ranging from 1.5 to 5 Grad(Si) in Cu-doped-HfO_2-based resistive switching devices [148]. ZrO_x/HfO_x stacks exhibited a change in current after 10 MeV proton irradiation before the filamentary conduction path was formed, but the devices exhibited negligible degradation after electroforming the filament [149].

In addition to proton studies, gamma radiation effects have been investigated in memristors. TiO_2-based memristors exhibit negligible degradation after total ionizing doses of 45 Mrad(Si) of ~1-MeV gamma radiation and 23 Mrad(Si) of 941-MeV Bi-ions [150]. Cu-doped HfO_2 resistive switching devices have also exhibited very few changes due to 3.6 x 10^5 rad(Si) gamma radiation [151]. Finally, gamma radiation has been shown to promote the implantation of Ag+ ions in Ag/Ge-Se based memristors, thereby changing the conductivity of the Ge-Se chalcogenide glass [152].

The effects of radiation on analog memristors have only been minimally investigated. Therefore, this research examines the effects of X-ray and proton radiation on $LiNbO_2$-based analog memristors for neuromorphic computing applications to be used in harsh environments.

Lithium niobite ($LiNbO_2$) is a lithium intercalated sub-oxide of the widely researched $LiNbO_3$, and is unusual in that it is extremely conductive in both n- and p-type varieties with resistivities ranging from a few 10^{-4} ohm-cm to 10^6 ohm-cm [7, 39]. Unlike the digital memristors which are made from high resistivity materials, the memristors reported herein are fabricated using highly conductive materials. N-type material is grown with stoichiometric lithium content and is deficient in oxygen. P-type material is grown with near stoichiometric or only slightly deficient oxygen content and is instead as-grown or electrically doped to have a deficiency of lithium. This high level of conductivity is augmented with the ability to move the dopants (lithium vacancies) over macroscopic distances in very short times similar to common battery materials. Since lithium vacancies act as acceptors, the motion of lithium in response to an electric field moves the dopants, creating areas of high and low doping and thus areas of low and high resistance [29, 33,

85]. This resistance change can be continuously increased or decreased, thus implementing an analog memristor well-suited for emulating excitatory and inhibitory mammalian synapses [7].

7.2 Experimental Setup

The $LiNbO_2$-based memristor used in this study has an annular geometric structure, which consists of an outer ring and an inner dot separated by 55 μm, as shown in the inset of Figure 7.1. The sample studied in this research is orders of magnitude larger than traditional memristors, but employs the same switching mechanism, and is therefore useful for basic studies. This structure was obtained using standard photolithographic patterning methods and a metallization lift-off. The electrodes used in this experiment include a stack of 1500 Å nickel deposited directly on the $LiNbO_2$ and 500 Å of gold on top of the nickel layer. Nickel was chosen as the electrode directly contacting $LiNbO_2$ because it is known to be lithium-blocking so incorporation of lithium into the metal contact is expected to be minimal [153].

Both electrical and crystallographic characterizations were performed on the $LiNbO_2$ analog memristor to determine the effects of the applied radiation. Ex situ electrical measurements on the memristive devices were carried out with a Keithley 2400 Source Meter and an Agilent 4294A High Precision Impedance Analyzer for the AC and Electrochemical Impedance Spectroscopy measurements respectively. In situ electrical measurements were carried out with an HP 4156B Semiconductor Parameter Analyzer. Crystallographic characterization was performed using a Philips XPert MRD X-ray Diffraction (XRD) system.

The radiation sources used in this study were a 10-keV X-ray source and Pelletron proton irradiator at Vanderbilt University. The X-ray irradiations were performed at a dose rate of 31.6 krad(SiO_2)/min, and devices were irradiated to doses up to 7.7 Mrad(SiO_2). Initially, the $LiNbO_2$ memristor was irradiated with a 4.2 Mrad(SiO_2) dose, but extensive characterization was not performed at this lower dose because no meaningful change was detected in the screening characterization. The Pelletron was operated at a proton energy of 1.8 MeV, and devices were irradiated to fluences up to 10^{14} cm^{-2}. In-situ electrical data were taken during both X-ray and proton irradiation. X-ray exposures were performed at the wafer level; proton irradiations were performed on unlidded packaged devices. This packaging resulted in considerable series resistance, so the post-irradiation electrical results are reported for both packaged and unpackaged devices. Unpackaged devices were directly probed, bypassing the package leads. During radiation, the $LiNbO_2$ memristor was grounded.

7.3 Results and Discussion

Changes in the memristive response of the $LiNbO_2$-based memristors due to the effects of radiation were determined by current-voltage (I-V), electrochemical impedance spectroscopy (EIS), and X-ray diffraction (XRD) analysis. Hysteresis in I-V curves is a characteristic of memristive systems as defined by Chua, who first theorized the existence of the memristor and memristive devices [5, 154].

To quantify repeatability before irradiation, the $LiNbO_2$ memristor was cycled 193 times, and the resistances recorded at both the maximum and minimum applied voltages were very reproducible. Resistances measured at the maximum voltage applied (1.0 V) had a mean of 98 ohms with a standard deviation of 2 ohms (2.0%), while the

resistances recorded at the minimum voltage applied (-1.0 V) had a mean of 120 ohms with a standard deviation of 3 ohms (2.3%).

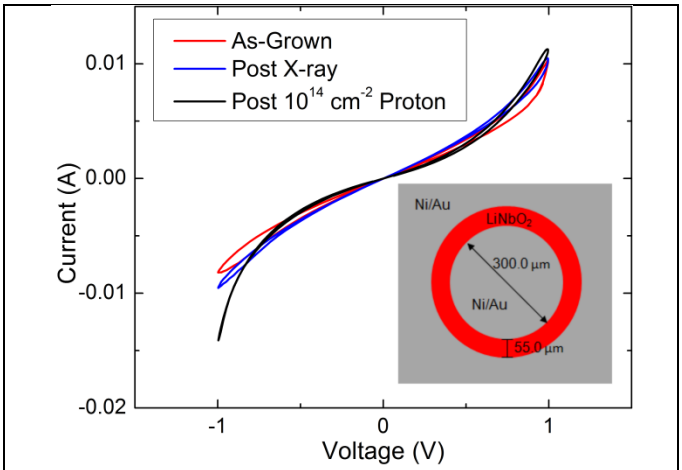

Figure 7.1: Characteristic hysteresis loops of an $LiNbO_2$ memristor both before and after irradiating the device. [155]

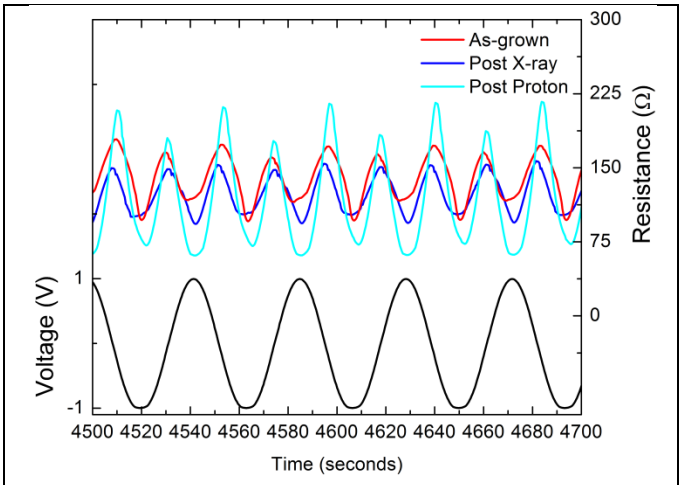

Figure 7.2: The resistance of the $LiNbO_2$ memristor as a 25 mHz sinusoidal voltage is applied. After irradiating the sample with X-rays, the change in resistance due to the application of the sinusoidal voltages is lower than the as-grown sample. However, after proton irradiation, the change in resistance has increased. [155]

As shown in Figure 7.1, the conductivity and the hysteresis present in the I-V curve change after irradiating the memristor with both 10-keV x-rays and 1.8-MeV protons. Before irradiation, the largest difference in the I-V hysteresis curve occurs at 0.926 V where currents of 8.53 mA and 7.26 mA are measured on the rising and falling voltage. This change in current corresponds to a hysteresis effect of 17.5% where the hysteresis effect is the current percent change at the voltage with the widest hysteresis. After a 7.7 Mrad(SiO_2) dose of X-ray radiation, the same voltage point resulted in currents of 9.27 mA and 8.27 mA. The post X-ray radiation hysteresis effect corresponds to a change of 12.1% in the current. After irradiating the analog $LiNbO_2$ memristor with protons, the I-V curve exhibits a maximum hysteresis effect at the same voltage of 9.8% with current values of 9.90 mA and 9.02 mA. The memory effect of the $LiNbO_2$ memristor at 25 mHz has decreased after irradiation. However, the hysteresis curves are taken at a constant excitation frequency and thus the speed of ion motion is not accounted for in these measurements. For example, this decrease in hysteresis could be due to increased lithium mobility, which would allow lithium ions to follow the applied sinusoidal voltage with less phase lag. In order to investigate the time dependence of this ion motion, the excitation frequency was varied using Electrochemical Impedance Spectroscopy (EIS).

Figure 7.2 shows the change in resistance as a 2 V peak-to-peak quasi-static sine wave operating at 25 mHz is applied across the memristor before and after irradiation. The range of the resistance measured under the application of the sinusoidal voltage before irradiating the memristor was from 97.1 Ω to 178.6 Ω, $\Delta R/R$ of 83.9%, where ΔR

is the difference in measured resistance and R is the minimum resistance. The range in resistance measured after X-ray irradiation was from 92.5 Ω to 149.2 Ω, a ΔR/R of 61.3%. However, after proton radiation, the range in resistance measured was from 61.3 Ω to 214.9 Ω, a ΔR/R of 250.6%. This enhanced resistance change in the proton irradiated $LiNbO_2$ memristor is attributed to the creation of defects that allow additional lithium motion pathways, including vertical motion, in the memristor. Vertical motion in a perfect crystalline $LiNbO_2$ material would normally be difficult because of the lack of channels for Li to move in the c-axis direction. If defects were introduced that created vertical motion pathways, Li ion motion could be enhanced both in and out of plane [156].

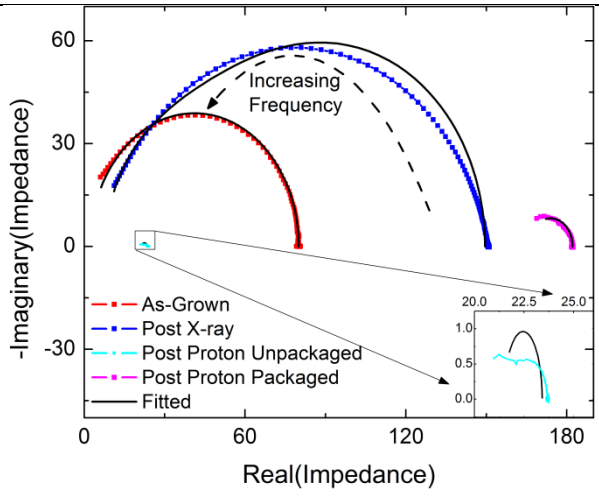

Figure 7.3: Electrochemical Impedance Spectroscopy measurements performed before and after irradiating the $LiNbO_2$ memristor. [155]

Electrochemical Impedance Spectroscopy (EIS) was performed to characterize the frequency response of ionic motion in the $LiNbO_2$ memristors before and after irradiation

as shown in Figure 7.3. EIS is a powerful technique largely used to characterize ionic motion in battery materials, and can separate out the conduction of ions and the phase lag of ions even in the presence of a highly conductive background electronic contribution [157]. Furthermore, interfacial vs bulk ion motion in analog $LiNbO_2$ memristors can be extracted [93]. In EIS, a sinusoidal voltage input of varying frequency is applied to the memristor. The resulting current phase offset and magnitude are acquired and analyzed by fitting the data to a model composed of circuit elements that correspond to physical phenomena [93].

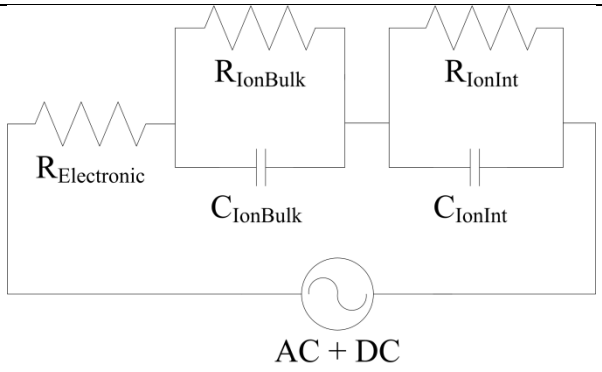

Figure 7.4: Circuit model used to describe $LiNbO_2$ analog memristor operation, which was adapted from a battery cathode model. The circuit model is composed of an electronic resistance and two resistors describing interfacial and bulk ionic resistances. A capacitor is in parallel with each ionic resistance, which describes the phase lag between the applied sinusoidal voltage and the resulting ionic current. [155]

The pre-irradiation and post-irradiation spectra were fit to a circuit model that describes analog memristor operation as shown in Figure 7.4. The analog $LiNbO_2$ analog memristor model was adapted from a battery cathode model [99]. In this model, the capacitances are not traditional electronic capacitances but are instead ionic capacitances

associated with the ionic phase lag between the applied sinusoidal voltage and the resultant ionic current. At low frequencies, there is no ionic current phase shift because the excitation frequency is low enough (<100 kHz) that the lithium ions can track the sinusoidal voltage. However, at higher frequencies, the excitation frequency is too high for the lithium ions to respond to the applied voltage and thus the measured phase offset between the applied voltage and the resulting current is due to an ionic phase offset. This phase offset is modeled with capacitors, and an increase in capacitance indicates that lithium conductivity has increased in the $LiNbO_2$ memristor, while a capacitance decrease would correspond to a decrease in lithium conductivity. The analog $LiNbO_2$ EIS circuit model includes a series combination of a resistor, a resistor in parallel with a capacitor, and a second resistor in parallel with a capacitor [93]. The resistors in parallel with the capacitors represent the in-phase ionic motion whereas the remaining unpaired resistor models the electronic (electron/hole) resistance [93]. A summary of the fitted circuit elements is included in Table I.

Before irradiation, the model previously developed for $LiNbO_2$ memristors gives a good fit to the EIS measured data as shown by the fitted spectra in Figure 7.3 [93]. However, after irradiation, this fit degrades with both X-ray and proton irradiation, especially for the unpackaged proton irradiated device. The degradation of the fit for the model traditionally used for $LiNbO_2$ memristors could be due to added ion motion pathways created by an increase in defects [156, 158].

In the as-grown sample, the bulk electronic resistance is negligible in comparison to the other resistances in the model. However, after X-ray irradiation, the bulk electronic resistance has increased. This increase in bulk electronic resistance is attributed to

activation of defects in the bulk, lowering electronic mobility, although the specific defect types have not yet been identified. Additionally, the bulk ionic capacitance increases while the bulk ionic resistance decreases. The decrease in ionic resistance and increase in ionic capacitance are consistent with an increase in lithium mobility. Thus, the lithium current is better able to follow the applied sinusoidal voltage. The enhanced ability of lithium to follow the applied sinusoidal voltage is attributed to an increase in defect density after the application of radiation. Defects are known to provide an additional diffusion path for lithium ions in a similar layered lithium metal oxide material, $LiCoO_2$ [156].

Finally, the interfacial ionic resistance and capacitance both increase after X-ray irradiation. The increase in interfacial capacitance is attributed to the same phenomenon as the bulk interfacial capacitance, increases in defect density. The introduction or activation of defects through radiation damage results in increased lithium diffusivity at the interface similarly to the bulk. The change in ionic interfacial capacitance is 22.4% comparable to 26.8% in the bulk. It is not yet clear that this change is statistically relevant but assuming it is significant, the lower change in ionic capacitance at the interface vs. the bulk could be attributable to an increase of lithium accumulation at the interface after radiation. The accumulation of lithium ions increases the ion diffusivity due to increased coulombic repulsion of charged ions and thus will compete against the electrical drift of ions resulting in the interfacial capacitance changing less than the bulk capacitance [159].

The ionic interfacial resistance dramatically increases after X-ray radiation exposure and follows the opposite trend of the ionic bulk resistance. This behavior is consistent with the hypothesis that the radiation-induced change in interfacial capacitance

is lower than that of the bulk ionic capacitance. As the diffusivity of lithium is increased due to radiation-induced defects, the concentration of lithium at the interface will reach higher levels for a given magnitude excitation, lowering the Li vacancy (dopant) concentrations near the interface. This increase in lithium concentrations will increase the ionic resistance due to coulombic repulsion and fewer vacancies for Li diffusion (lower ionic mobility) at the interface [93]. Fewer Li vacancies also result in an increase in electronic resistance. This increase in lithium concentration at the interface is opposite to the removal of Li atoms in the bulk, which results in higher ionic mobility (lower ionic

TABLE I
EIS FITTED CIRCUIT VALUES

Circuit Element	$R_{Electronic}$ (Ω)	R_{IonInt} (Ω)	$R_{IonBulk}$ (Ω)	C_{IonInt} (nF)	$C_{IonBulk}$ (nF)
As-Grown	0	13.1	67.0	0.237	0.123
Post X-ray	7.9	101.7	39.9	0.290	0.156
Post Proton	21.49	0.46	1.46	8.76	2.94

Table 7.1: EIS Fitted Circuit Values [155].

resistance) after irradiation. However, we should note that the oxidation of the contact by radiation-generated ozone may play a role in the ionic interfacial resistance changes with radiation [160]. This possibility will be examined in later studies.

After proton irradiation, the electronic resistance dominates the impedance response, indicating massive changes in electronic mobility, presumably due to defect

introduction. After proton irradiation, the bulk electronic resistance has increased by 172%, compared to the X-ray irradiated device. This bulk electronic resistance increase is attributed to crystalline damage in the $LiNbO_2$ crystal structure, which could result in a reduction in grain size and a corresponding increase in density of grain boundaries. Evidence of increased defect density will be discussed in the X-ray diffraction section of this research. The interfacial and bulk ionic resistances both decrease, indicating that lithium is more mobile in the crystal structure. Again, this is consistent with increased defect density and thus additional pathways for lithium motion in the analog memristor. The interfacial and bulk ionic capacitances both increased due to the application of proton irradiation. An increase in capacitance will result in a decrease in impedance, and thus is consistent with an increase in lithium mobility in the device.

Quantitative insight into ionic mobility can also be obtained from the impedance spectra using the relaxation frequency, the frequency at which the ionic movement begins to no longer be able to follow the excitation frequency. The relaxation frequency is found by the frequency at which the imaginary impedance is at a maximum in the Nyquist plot shown in Figure 7.3. The relaxation frequency for conductive ions is directly proportional to the ionic mobility as shown in Equation 7.1 where ε is the dielectric constant, q is the elementary charge, μ_i is the mobility of ions, n_i is the ion density, and f_i is the ionic relaxation frequency [161].

$$2\pi f_i = \frac{q\mu_i n_i}{\varepsilon} \tag{7.1}$$

The relaxation frequencies for the as grown, X-ray irradiated, and proton irradiated samples are 7.59×10^6, 2.13×10^7, and 8.63×10^7 Hz respectively. Thus, assuming all constants remained the same throughout the experiment, the mobility of

lithium ions in the analog $LiNbO_2$ memristor increased by 181% after X-ray irradiation and by 305% after proton irradiation.

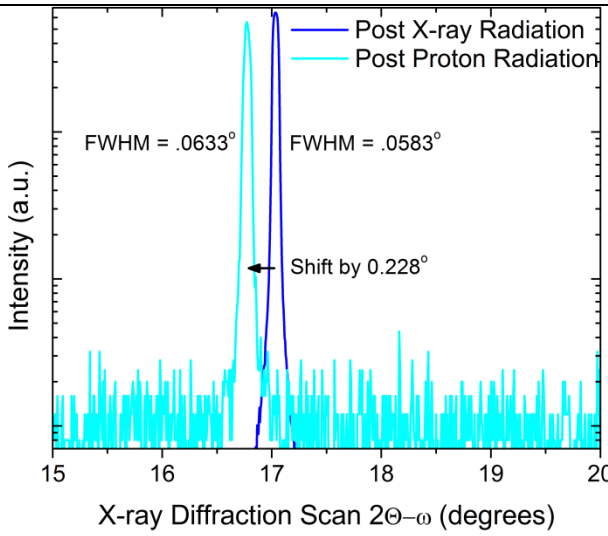

Figure 7.5: X-ray diffraction two-theta omega scan. The two-theta position for the (0002) $LiNbO_2$ peak has shifted by .228 degrees after proton irradiation, which indicates an increase in the c-spacing from 10.40 Å to 10.54 Å. [155]

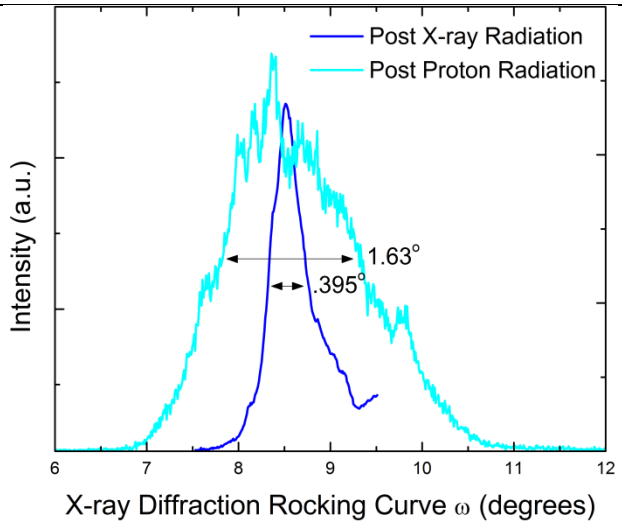

Figure 7.6: X-ray diffraction rocking curve. After proton irradiation, the $LiNbO_2$ crystal has been damaged, and is shown by the FWHM of the XRD rocking curve increasing by more than 400%. [155]

Proton irradiation is expected to cause displacement damage, and to investigate this displacement damage, X-ray diffraction analysis was performed to determine changes in the crystal structure. As shown in Figures 7.5 and 7.6, before proton irradiation, the full width at half-maximum (FWHM) of the rocking curve and two-theta omega scan were 0.395 and 0.058 degrees respectively. After proton irradiation, the FWHM of the rocking curve and two-theta omega scans have both increased to 1.63 and 0.063 degrees respectively. A broadening of the rocking curve and two theta omega scans is indicative of degradation in crystalline quality, so after proton irradiation, the $LiNbO_2$ has experienced damage. Additionally, the position of the (0002) $LiNbO_2$ peak has shifted in the two-theta omega scan by 0.228 degrees after proton irradiation. This shift in the two-theta omega scan is indicative of an unexpectedly large change in the c-spacing of the unit cell from 10.40 Å to 10.54 Å after proton irradiation. The c-spacing is the crystallographic height of the unit cell and represents the distance between the top and

bottom of 3 lithium layers in $LiNbO_2$. A larger c-spacing could facilitate the higher lithium mobility exhibited in the impedance spectra for the proton-irradiated sample and may be the result of hydrogen (proton) implantation. It has been shown that hydrogen insertion into lithium intercalated oxides with a similar structure to $LiNbO_2$ can cause distortion in the crystal [162].

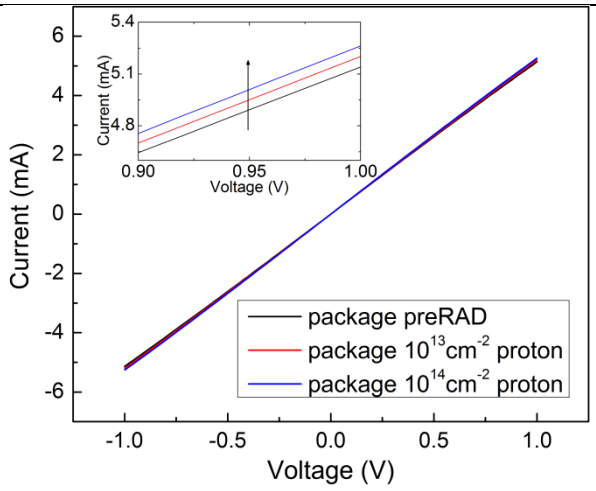

Figure 7.7: In situ I-V curves taken during the proton radiation portion of the experiment on the packaged $LiNbO_2$ memristor. The packaging introduces dominating series resistance, which hides the memristance effect. However, the in situ data reveals that the resistance of the overall packaged device decreases with increasing fluence. [155]

The decrease in structural quality in the $LiNbO_2$ memristor changed the electronic properties as seen in the I-V characterization in Figure 7.1. One of the changes includes an increase in conductivity, and this increase in conductivity was investigated during proton irradiation at different fluence levels. The I-V curves shown in Figure 7.7 are taken after the device was packaged. The packaging introduces extra series resistance, which dominates the resistance response and hides the memristance effect. This extra

parasitic resistance is due to the wires used in packaging the memristor and contact interfacial resistance introduced in the bonding of the wires to the device. A detailed examination of the positive voltage region of the curve, shown in the inset of Figure 7.7, indicates that during proton irradiation, the packaged memristor became more conductive and did so increasingly at higher proton fluences. This current change is easily resolved by the experimental setup, which has a resolution of 1 pA.

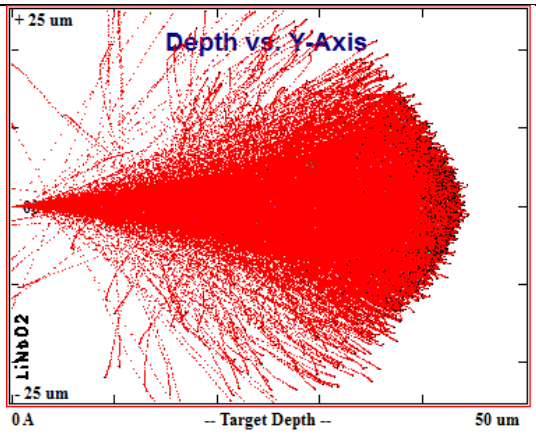

Figure 7.8: 1.8 MeV proton particles (10^5 protons) incident on an $LiNbO_2$ memristor, the projected range is 40.14 μm.[155]

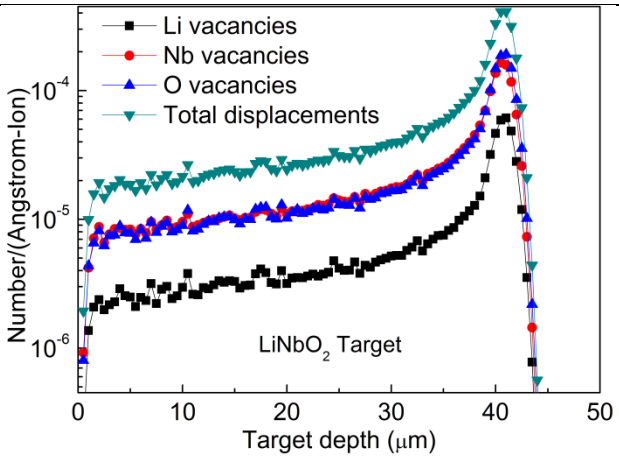

Figure 7.9: 1.8 MeV proton irradiation on an $LiNbO_2$ memristor introduces (a) lithium vacancies distribution (b) niobium vacancies distribution (c) oxygen vacancies distribution, and (d) total displacement damage distribution. [155]

Monte Carlo simulations of $LiNbO_2$ memristor proton irradiation were performed in the TRIM part of the SRIM software package. As shown in Figures 7.8 and 7.9, proton radiation can generate lithium, oxygen and niobium vacancies and displacement damage in the $LiNbO_2$ memristor. Figure 7.8 shows 1.8 MeV protons (10^5 ions) incident on the $LiNbO_2$ memristor. The projected range is 40.14 μm, much less than the total thickness of $LiNbO_2$ memristor (250 μm). For clarity, the thickness of the $LiNbO_2$ layer is set to 50 μm in the simulation. Fig. 7.9 shows the lithium, oxygen and niobium vacancies and displacement damage distributions in $LiNbO_2$ layer after proton irradiation. All the distribution peaks are located at the projection range. Oxygen vacancies are the most numerous followed by niobium vacancies and lithium vacancies. The TRIM simulation results indicate that proton radiation damage to the $LiNbO_2$ crystalline lattice is expected and is consistent with the X-ray diffraction results above.

7.4 Conclusions

The effects of radiation on the operation of an $LiNbO_2$ memristor were characterized by I-V hysteresis, EIS, low-frequency AC voltage analysis, and XRD. The $LiNbO_2$ memristor exhibits a change in behavior after a 7.7 Mrad dose of X-ray radiation and a 10^{14} cm^{-2} dose of proton radiation. While this is a relatively high dose level, it is useful in identifying mechanisms that may affect future generations of these devices. X-ray radiation leads to an increase in ionic motion in the bulk and a higher ionic resistance at the metal-$LiNbO_2$ interface whereas proton radiation results in higher ionic motion in the bulk and interface. The increased ionic motion suggests that the radiation-induced defects improve the temporal response of ionic programming. However, with enough crystalline damage, the $LiNbO_2$ memristors may no longer operate as memristors at a fixed operational frequency in a system application unless that system is designed to account for higher operational speed with exposure dose. The effects and location of radiation-induced defects will be crucial as these $LiNbO_2$-based memristors are scaled down in future generations and interfacial changes begin to dominate performance.

CHAPTER 8 : Analog Memristor Finite Element Model

8.1 Introduction

In order to gain a better physical understanding of analog memristors, a finite element simulation has been developed. These simulated analog memristors operate by the gradual doping of a film using ions similar to the WO_3-based memistor [67], the $LiNbO_2$ memristor [7], and the analog organic memristor [63]. The finite element model is implemented as a two dimensional semiconductor in which mobile ions determine the doping profile in the device. While implemented as lithium ions in a p-type material in the present case, modeling the $LiNbO_2$ memristor, the physics represented herein describe any ion doped memristor or memistor.

The effects of changing initial concentration of dopants, hole mobility dependence on acceptor levels, geometry, and boundary conditions are investigated by comparing the transient response of the lithium concentration profile, electric field profile, and device current. Thus the analog memristor simulations are divided into four cases. In the first case, a rectangular analog memristor is simulated and lithium atoms (dopants) are restricted within the device, i.e. no ion extraction. The second case introduces the dependence of hole mobility on the number of acceptors, a well-known phenomenon in semiconducting materials [163]. The third case explores different constrictive flow geometries and their effect on device performance, and the fourth case considers the effects of lithium extraction from the memristor. Key device performance parameters investigated in the simulated memristors include the speed and magnitude of the resistance change exhibited by the analog memristor in response to a DC bias.

8.2 Analog Memristor Model

The memristor model was developed using a commercially available finite element solver (COMSOL Multiphysics™ by Comsol Inc.). Because the relaxation times for holes and electrons is much shorter than that of lithium ions [99], the simulation was implemented using an iterative process where the solving of temporal lithium drift and diffusion was alternated with the solving of steady-state hole and electron movement with Poisson's equation. To ensure convergence in the final solutions, meshing and time steps are chosen to satisfy the Courant condition [164].

Boundary conditions are chosen such that the normal components of electric field on the non-metalized surfaces are zero, and the hole and electron current are zero except at the device contacts. In all simulations other than case 4, lithium ions are confined within the device. That is, the ionic current normal to the device at all edges is zero.

In case 4, a fixed flux of lithium is extracted at the bottom contact of the device, which models intercalating mobile dopants into the device contact. Ohmic contacts are included in the model so infinite minority carrier recombination velocity is implicit at the metal contacts. The applied voltage to the metal contact is equal to the Fermi level in the semiconducting memristor at the contact. Thus, the electrostatic potential at the contact is

$$\varphi_E = V_{Bias} + \frac{kT}{q} ln\left(\frac{\frac{N_A - N_D}{2} + \sqrt{\left(\frac{N_A - N_D}{2}\right)^2 + {n_i}^2}}{n_i}\right) \tag{8.1}$$

where φ_E is the electrostatic potential, V_{Bias} the applied bias, N_A the concentration of acceptors, N_D the concentration of donors, and n_i the intrinsic carrier concentration.

Poisson's equation is solved to obtain the electrostatic potential in the simulated memristor due to holes, electrons and ions:

$$-\nabla \cdot (\varepsilon_r \varepsilon_0 \nabla \varphi_E) = q(p - n + N_D - N_A) \tag{8.2}$$

The current densities of lithium, holes and electrons are determined from

$$J_{Li} = J_{Li_{drift}} + J_{Li_{diffusion}} = q\mu_{Li}[Li]\varepsilon - qD_{Li}\nabla[Li] \tag{8.3}$$

$$J_p = J_{p_{drift}} + J_{p_{diffusion}} = q\mu_p p\varepsilon - qD_p\nabla p \tag{8.4}$$

$$J_n = J_{n_{drift}} + J_{n_{diffusion}} = q\mu_n n\varepsilon + qD_n\nabla n \tag{9.5}$$

where μ_{Li}, μ_p and μ_n represent the mobility of lithium, holes, and electrons respectively, D_{Li}, D_p, and D_n the diffusivities of lithium, holes, and electrons respectively, q the elementary charge, and ε the electric field. In the simulation of case 2, the mobility of holes is a function of the concentration of acceptors. In all cases, the diffusivity of lithium increases for increasing amounts of lithium [159]. This diffusivity increase is achieved by introducing an entropic term that inhibits lithium from reaching unphysical concentrations [159].

$$D^{chem}(c) = D(1 - \frac{2ac}{\rho kT} + \frac{c}{1-c}) \tag{8.6}$$

Finally, The continuity equations for lithium ions, holes and electrons are given by:

$$\frac{\partial Li_{vacancy}}{\partial t} = \frac{\partial N_A}{\partial t} = \frac{1}{q}\nabla \cdot J_{Li} \tag{8.7}$$

$$\frac{\partial p}{\partial t} = \frac{1}{q}\nabla \cdot J_p + \frac{\partial p}{\partial t}|_{Electron-Hole\ Recombination} \tag{8.8}$$

$$\frac{\partial n}{\partial t} = \frac{1}{q}\nabla \cdot J_n + \frac{\partial n}{\partial t}|_{Electron-Hole\ Recombination} \tag{8.9}$$

Since some material constants are unknown for $LiNbO_2$, ion mobilities and diffusivities have been used that describe a similar material with a layered structure, $LiCoO_2$, that reversibly intercalates and deintercalates lithium from $1>x>0.5$ [99]. Likewise, the electronic mobility, diffusivity, and relative permittivity of semiconducting silicon were used making the analog memristor simulation results representative in trend but not quantifiably accurate.

Models have been previously developed to describe memristor operation which include dopant drift due to an applied bias [165-169]. However, these simulations are focused on filamentary memristors and do not investigate the geometry, mobility variation and ion extraction effects demonstrated herein. Additionally, phenomenological memristor models have been implemented [6, 170-174]. Although these phenomenological models, which are mainly implemented in SPICE, are less grounded in the physics of the memristor than a full drift-diffusion model, they are useful in system-level design.

8.3 Case 1: Simple Parallel Electrode Memristor

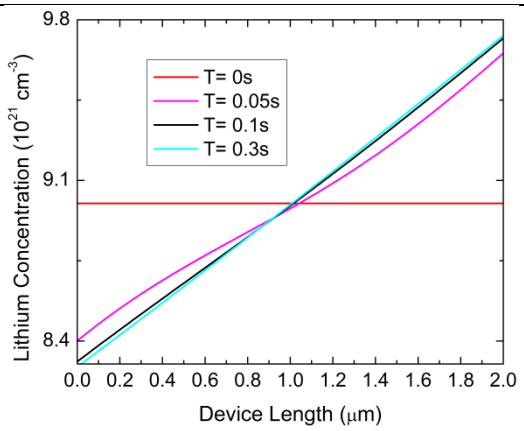

Figure 8.1: Spatiotemporal lithium concentration profile for case 1A. The homogeneous lithium concentration initially changes only at the interfaces, eventually approaching a linear profile.

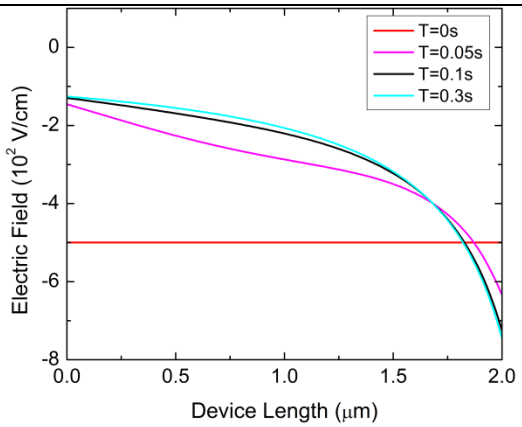

Figure 8.2: Spatiotemporal electric field profile evolution for case 1A. The complex electric field evolution arises from gradients in acceptors, which dominate the interfacial electric field profile at early time steps, and the creation/destruction of acceptors at the anode/cathode.

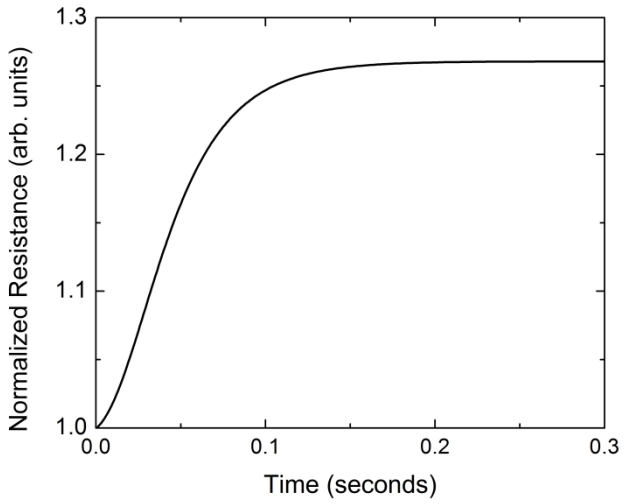

Figure 8.3: Resistance transient response for the case 1A simulated memristor. The increased initial lithium concentration of case 1A leads to a faster and larger resistance change.

The memristors simulated in case 1 are defined by insulating boundaries for lithium in the entire device, constant hole mobility, and a rectangular geometry. Two memristors were simulated with the constraints defined above for case 1 to determine the

effect of initial lithium concentration on device performance. The initial lithium concentrations for case 1A and 1B are 9.0 x 10^{21} $\frac{lithium\ atoms}{cm^3}$ and 7.0 x 10^{21} $\frac{lithium\ atoms}{cm^3}$ respectively. As time increases, lithium is drifted away from the positively biased anode (located at 0 μm) towards the grounded cathode (located at 2.0 μm) as shown in Figures 8.1 and 8.4. In the cathodic region with increased lithium concentration, holes are filled while holes are introduced in the anodic region [134]. Thus the dopant levels in the device change as a function of time. This shift in dopants produces a spatially changing electric field profile with a change in resistance as shown in Figures 8.2 and 8.5.

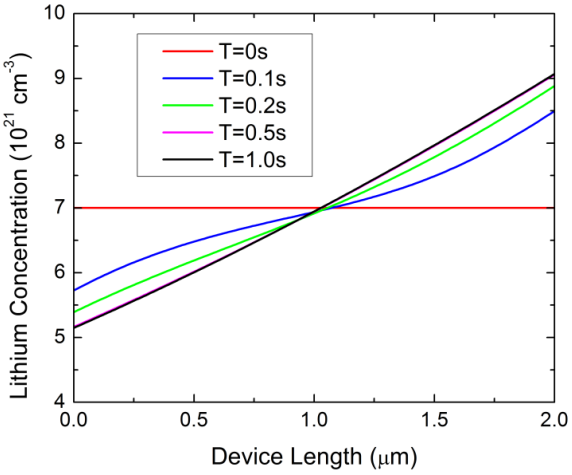

Figure 8.4: Spatiotemporal lithium concentration profile for case 1B. The lower initial lithium concentration compared to case 1A leads to decreased steady-state lithium concentrations.

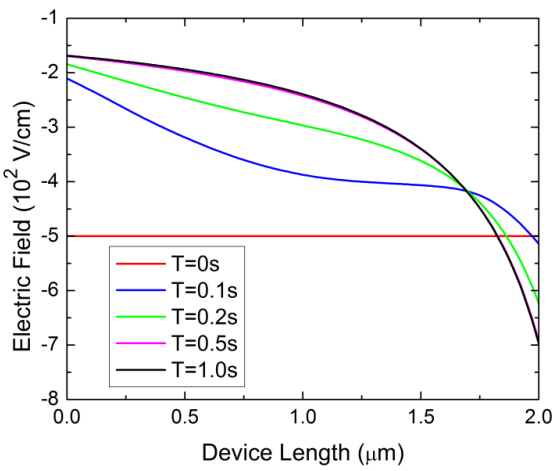

Figure 8.5: Spatiotemporal case 1B electric field profile. Unlike case 1A, a strong non-linearity in the lithium concentration profile does not exist, thus the electric field is dominated by the creation and destruction of acceptors as lithium is drifted in the device.

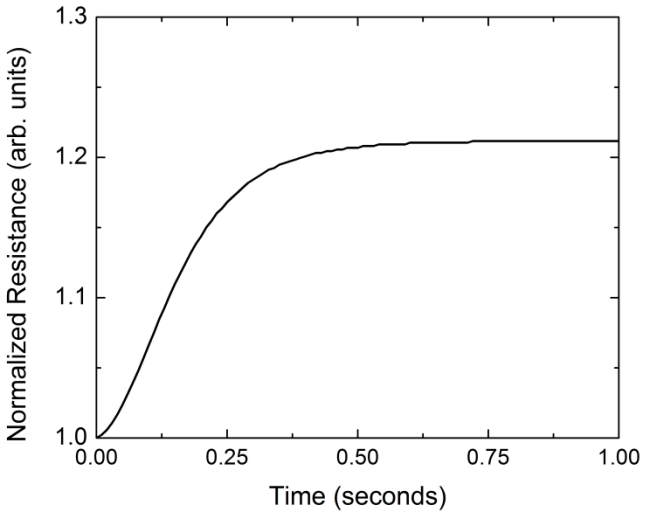

Figure 8.6: Transient resistance response for the Case 1B simulated memristor.

This evolution of lithium concentration in the device modulates the electric field as shown in Figures 8.2 and 8.5. Initially, at t=0 seconds, the hole motion is completely facilitated via drift producing an electric field that is constant throughout the device. At T=0.1s, the change in electric field is dominated by two factors. First, a gradient in acceptors (due to the change in lithium concentration) leads to a changing electric field. Additionally, as lithium approaches its stoichiometric concentration (1×10^{22} cm^{-3}), a resistive area is formed leading to a rapid increase in the magnitude of the electric field near the cathode. Later time steps are almost completely dominated by the latter effect as lithium vacancies and thus acceptors, plummet close to the cathode.

Eventually, the resistance reaches a steady state as demonstrated in Figures 8.3 and 8.6. As the simulation reaches this steady-state, drift and diffusion balance due to two separate phenomena. First, to maintain physical meaning, an entropic term is included which enforces volume constraints. The entropic term is realized by an increase in the diffusion coefficient as the concentration of lithium increases as shown in Equation

8.6 [159]. The lowest level of dopants (highest concentration of lithium) occurs at the cathode of the simulated memristor. The greatest magnitude of electric field and thus the highest level of drift current is partially offset by the entropic magnification of diffusivity (Equation 8.6).

The second phenomenon that balances drift and diffusion is an increase in the electrostatic potential as the acceptor concentration decreases (lithium concentration increases). Thus, as lithium begins to accumulate near the cathode, the applied bias is partially compensated according to the logarithmic dependence of electrostatic potential on dopants as shown in Equation 8.1. Conversely, as the lithium concentration is decreased, the number of acceptors increases and thus the electrostatic potential decreases. Because lithium depletes in the area nearest to the positive bias, the electrostatic potential near the anode decreases while the grounded cathode experiences an increase in the electrostatic potential. Thus there is a decrease in the overall electrostatic potential across the device and a resulting decrease in the drift component of current.

The steady state resistance change due to an applied bias in the case 1A and 1B devices is 27% and 21% respectively. This indicates that by only changing dopant concentrations within an analog memristor, only a modest resistance change is achieved. The main contributions to the increase in resistance are a) opposition of the drift of holes by the diffusion of holes resultant from the dopant concentration gradient and b) the formation of highly resistive areas with low concentrations of dopants as is evident from the electric field profile. However, by increasing the initial lithium concentration in the device, higher steady-state lithium concentrations and thus larger resistance changes

under the application of a DC bias are achievable. Simulations have been limited to the 90% lithium case herein due to model convergence limitations as stoichiometric Li concentrations are approached causing several decades of variation in resistivity along the device length. However, the general trend of increasing resistance change should continue with increasing Li concentrations.

8.4 Case 2: Mobility of Holes Dependent on Acceptor Concentrations

Case 2 differs from case 1B in that the mobility of holes in the device is dependent on the concentration of acceptors. As the concentration of acceptors is increased, impurity scattering increases which is realized by a decrease in hole mobility using the classic empirical Equation 8.10 [163].

$$\mu = \mu_{min} + \frac{\mu_o}{1+\frac{N}{N_{ref}}^{\alpha}} \tag{8.10}$$

where μ_{min}, μ_o, and α are unknown for both $LiCoO_2$ and $LiNbO_2$, so the values μmin=5 $cm^2V^{-1}s^{-1}$, μ_o=9.2 $cm^2V^{-1}s^{-1}$, and α=.88 were used in analogy to silicon and are representative only of the trend and not the magnitude of the effect in the lithium metal oxides. As shown in Figures 8.7 and 8.8, the lithium concentrations and electric field evolutions are similar to those in case 1B. This similarity is not surprising since the mobility of the electronic charge carriers in the device do not change significantly as shown in Figure 8.9 due to the limited concentration ranges simulated as restricted by the convergence limitations outlined above.

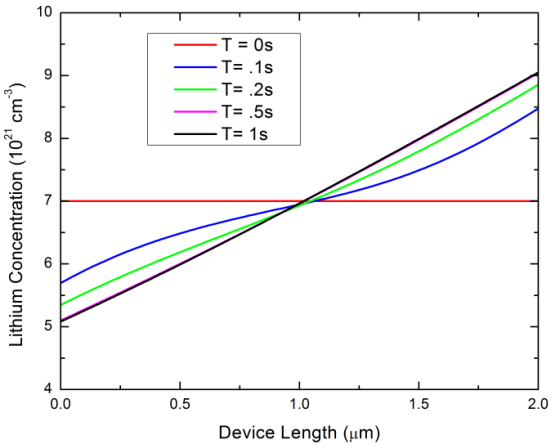

Figure 8.7: Spatiotemporal lithium concentration profile for mobility as a function of acceptor concentration, case 2. Case 1B and case 2 have similar lithium concentration profiles due to minimal hole mobility differences.

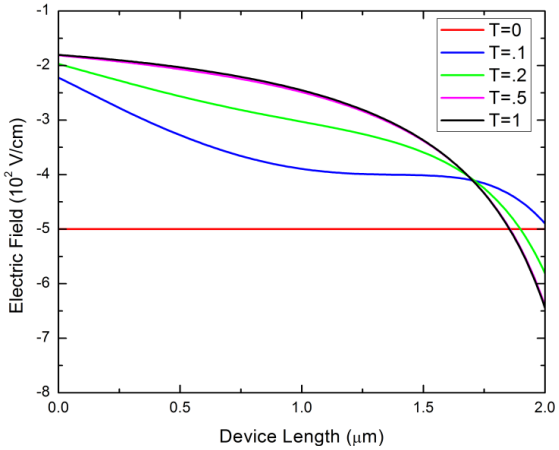

Figure 8.8: Spatiotemporal electric field profile for case 2. The anodic and cathodic regions of the case 2 simulated memristor are less and more conductive than the case 1B memristor, respectively, due to slight increases in cathodic hole mobility and decreases in anodic hole mobility.

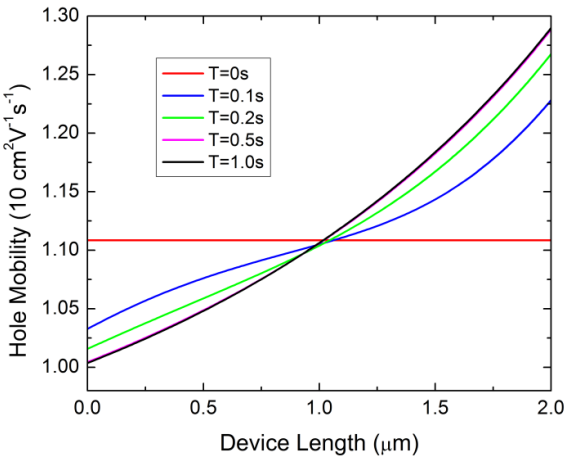

Figure 8.9: Spatiotemporal hole mobility profile for case 2. As lithium is drifted in the analog memristor, the hole mobility is increased (decreased) at the cathode (anode). The average hole mobility in the analog memristor increases as time increases.

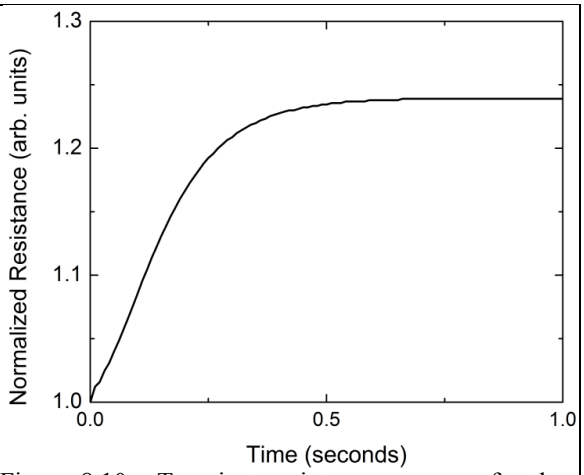

Figure 8.10: Transient resistance response for the Case 2 simulated memristor. The steady-state resistance change has slightly increased from case 1B due to the local anode mobility reduction in spite of the overall spatially integrated increase in hole mobility.

Overall, the effect of the acceptor concentration dependent mobility is minimal. As indicated by the electric field variations in the device shown in Figure 8.8, the conductive anodic region of the case 2 memristor becomes less conductive while the resistive cathodic region becomes slightly more conductive compared to the case 1B

memristor, thus, producing a minimal net effect. The net steady state resistance change from t=0s to t=1s is 24% in case 2 as shown in Figure 8.10, slightly increased from case 1B, both of which had the same initial lithium concentration. This slight increase is attributable to the spatially integrated increase in hole mobility as shown in Figure 8.9 where hole mobility has increased by 16.4% at the cathode and decreased by 9.3% at the anode.

8.5 Case 3: Effects of Geometry on Memristance Response

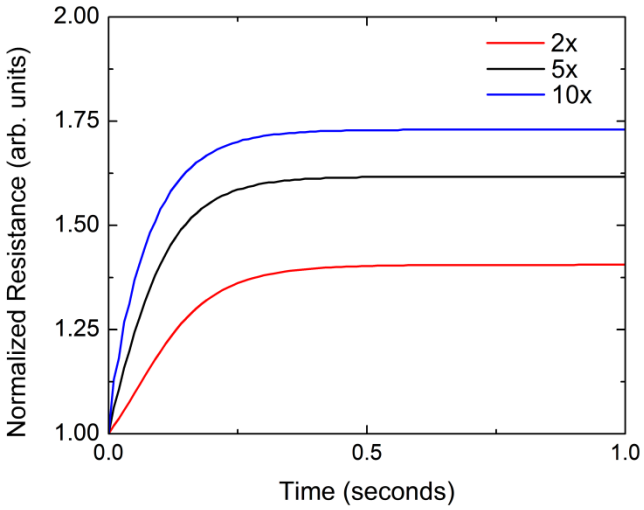

Figure 8.11: Transient resistance response for the Case 3 memristors with varied constrictive flow geometries. Greater resistance changes are achieved as the top to bottom contact width ratio is increased.

Memristor geometry can also affect the analog memristor's performance. Three different constrictive flow geometries were investigated with different ratios of the width of the top of the device vs. the width of the bottom of the device. Memristors with anode

to cathode contact length ratios of 2, 5, and 10 were simulated. In all three geometry configurations, a positive bias is applied to the top anode electrode of the device where the length of the contact is greater and the smaller, bottom cathode electrode is grounded. Thus, the movement of lithium is in the direction of the smaller contact and becomes constricted. The overall effect of the constrictive flow geometry is to facilitate areas of higher lithium concentration. This increased lithium concentration creates areas with higher resistivity compared to those in case 1B which result in a bigger change in steady-state device current as shown in Figure 8.11.

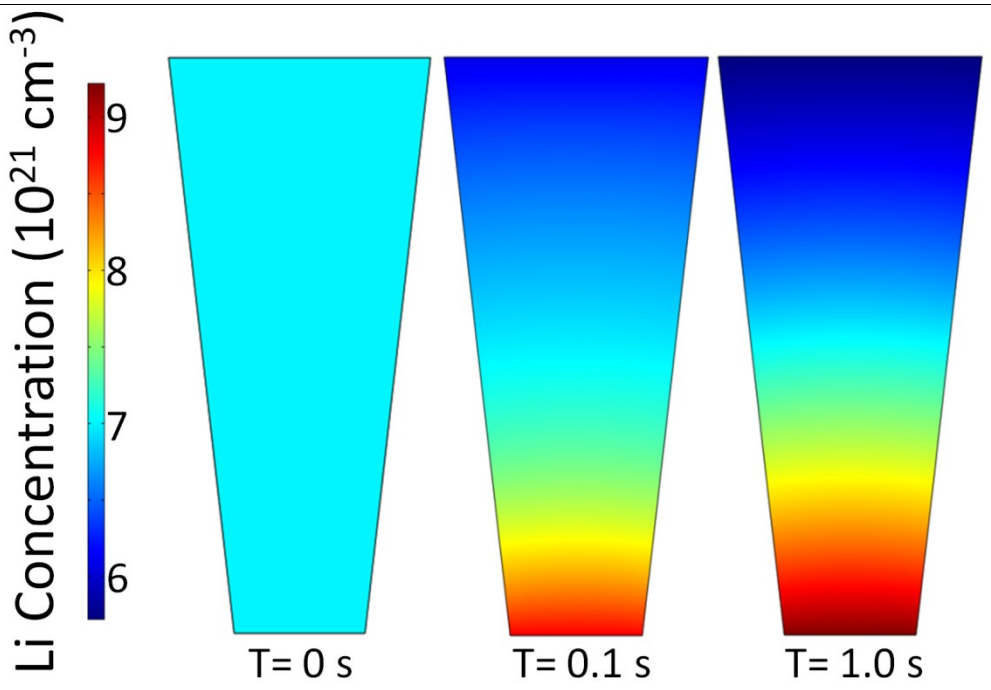

Figure 8.12: : Spatiotemporal lithium concentration for the 2x geometry memristor. The constrictive flow geometry facilitates higher local cathodic steady-state lithium concentrations than the Case 1B simulated memristor.

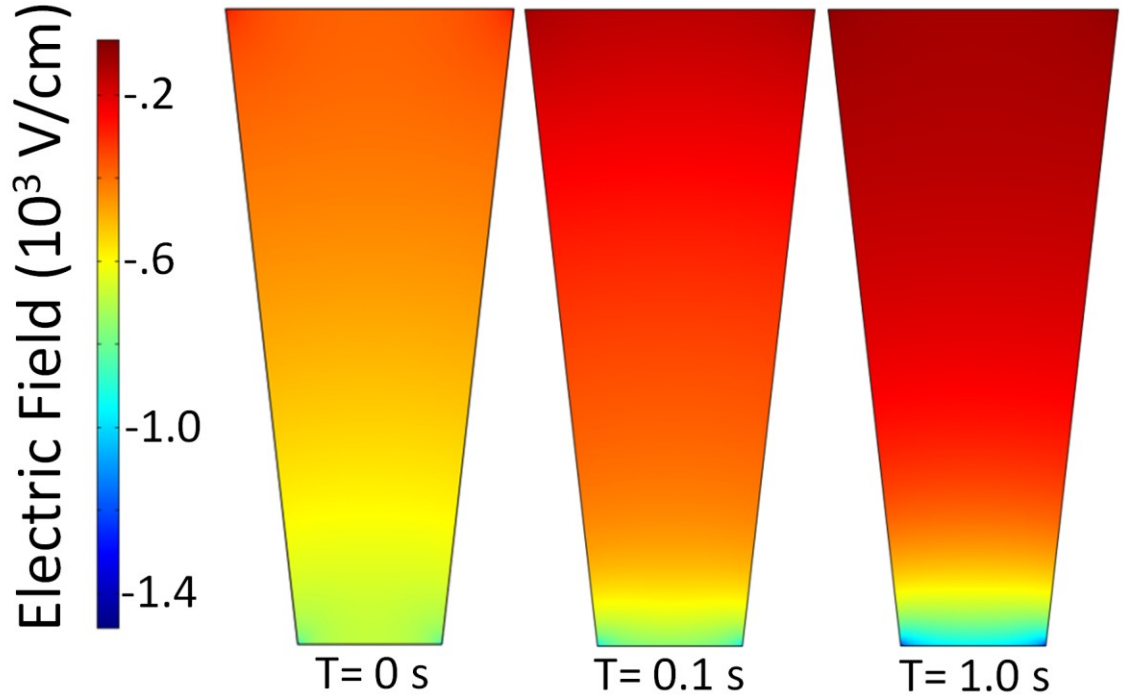

Figure 8.13: 2x geometry memristor spatiotemporal electric field. The inhomogeneous initial electric field profile resulting from current crowding at the cathode magnifies in time as the concentration of lithium vacancies at the cathode decreases.

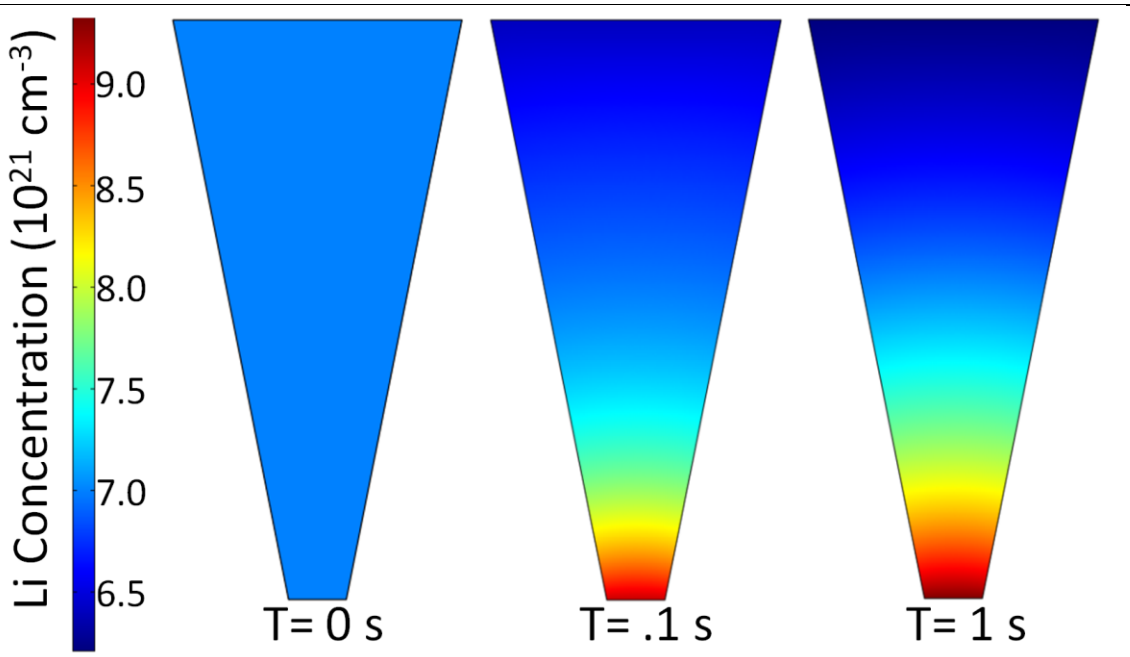

Figure 8.14: Lithium concentration spatiotemporal response for the 5x geometry case. As the contact width ratio is increased to 5x, higher amounts of lithium accumulate at the cathode and deplete from the anode, thus facilitating a greater change in resistance.

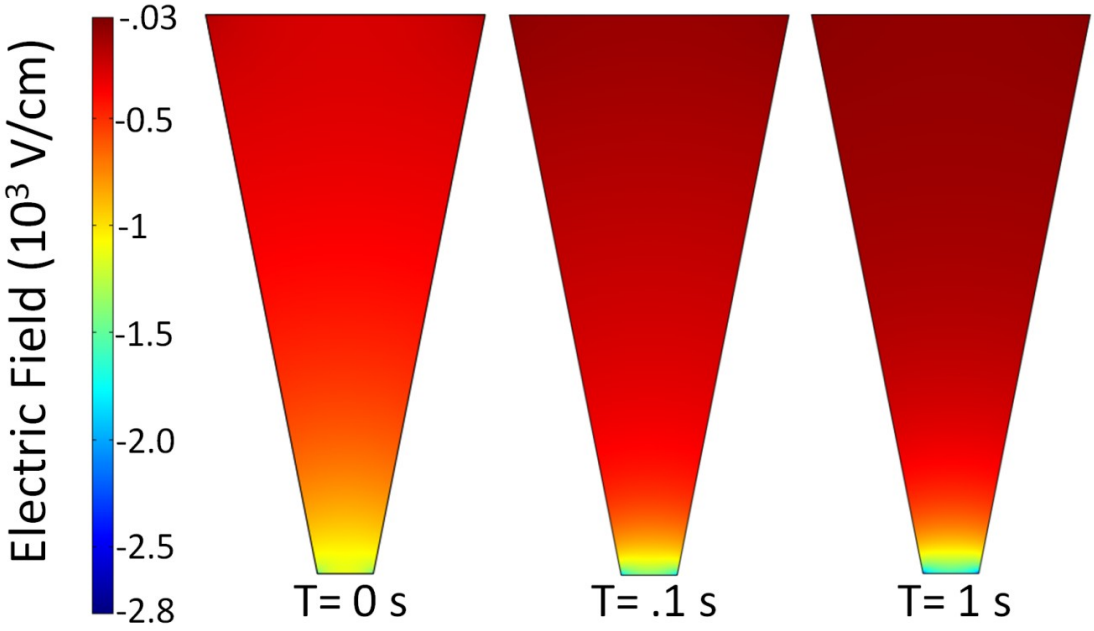

Figure 8.15: Spatiotemporal electric field progression for the 5x geometry case. Compared to the 2x case, higher electric fields are facilitated as the contact width ratio increases due to greater current crowding and lower concentrations of lithium vacancies (acceptors) at the cathode.

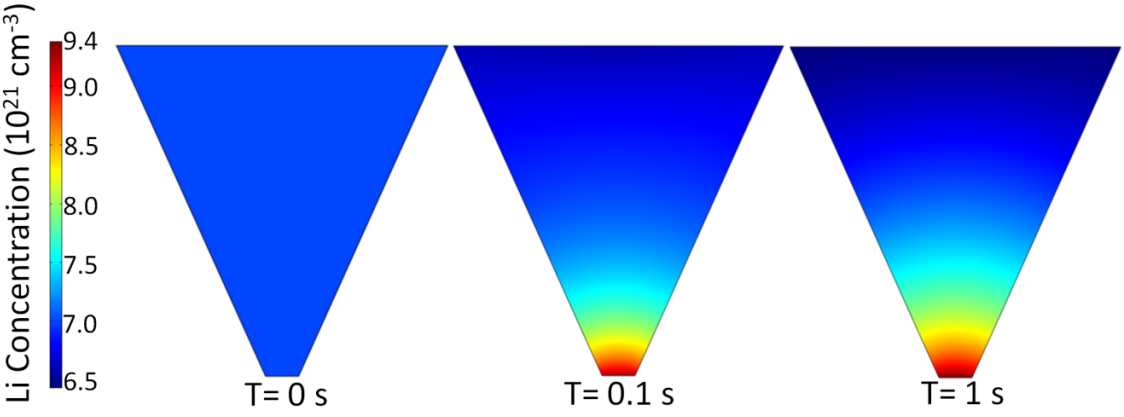

Figure 8.16: Spatiotemporal lithium concentration for the 10x geometry case. As the contact width ratio is increased to 10x, the maximum steady-state cathodic lithium concentration and thus resistance change begins to saturate due to volumetric constraints as stoichiometric lithium levels are approached.

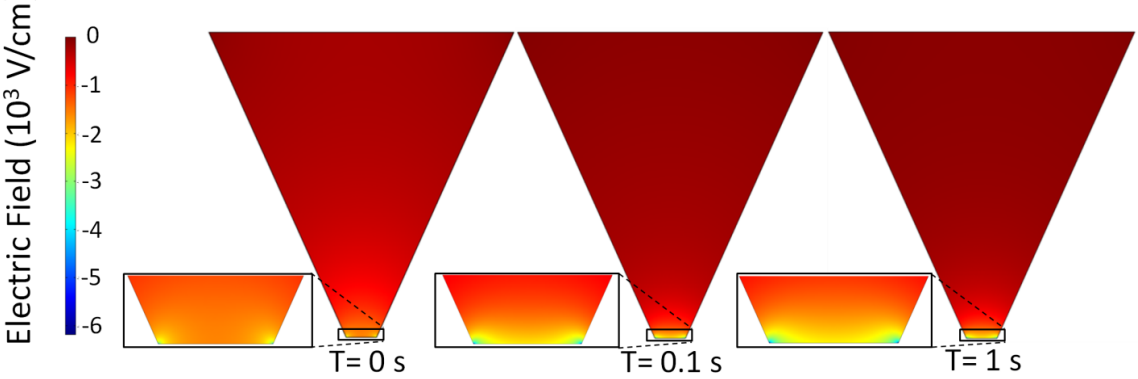

Figure 8.17: Spatiotemporal electric field for the 10x geometry case. As the contact width ratio is increased to 10x, the maximum electric fields in the device increase due to higher lithium concentrations and magnified current crowding facilitated by the constrictive flow geometry.

All constrictive flow devices initially have a homogeneous lithium concentration and an inhomogeneous resultant electric field due to current crowding at the smaller bottom electrode, the cathode. As time progresses, lithium is drifted to the cathode, resulting in a highly resistive cathode region. This highly resistive region in the case 1B, and the 2x, 5x, and 10x constrictive flow geometries have maximum lithium concentrations of 9.07 x 10^{21} atoms/cm^3, 9.22 x 10^{21} atoms/cm^3, 9.33 x 10^{21} atoms/cm^3, and 9.38 x 10^{21} atoms/cm^3 respectively as shown in Figures 8.12, 8.14, and 8.16. As the ratio of the length of the top electrode to the length of the bottom electrode increases, the maximum lithium concentration in the device increases slightly leading to a noticeable steady-state resistance change. The resistance changes for the 1B, 2x, 5x, and 10x geometries are 21%, 41%, 62% and 73% respectively. The difference in the resistance change between the 5x and 10x case is much lower than the case 1B to 2x case resistance change despite both case comparisons doubling in constrictive flow ratios. This saturation in resistance as the geometry ratio increases is due to the amplified diffusivity of lithium as concentrations increase as described in Equation 8.6 resulting in a diffusive

Li current that partially opposes the ion drift current. This saturation suggests that although the constrictive flow geometry is beneficial for obtaining slightly better resistance changes in memristive devices, the benefits of the change in geometry saturate as the contact ratio approaches 10:1.

8.6 Case 4: Effects of Lithium Removal on Memristance Response

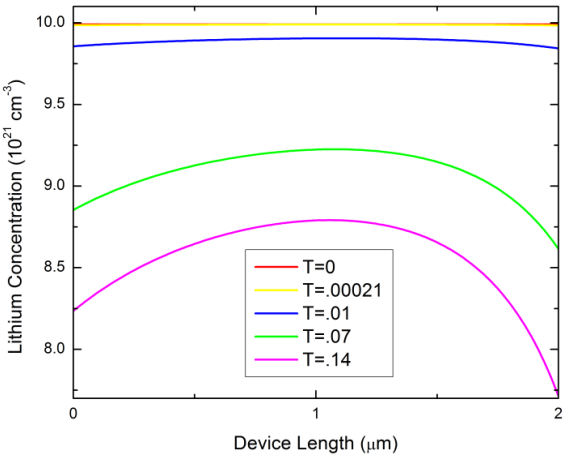

Figure 8.18: Temporal lithium concentration profile evolution for case 4.

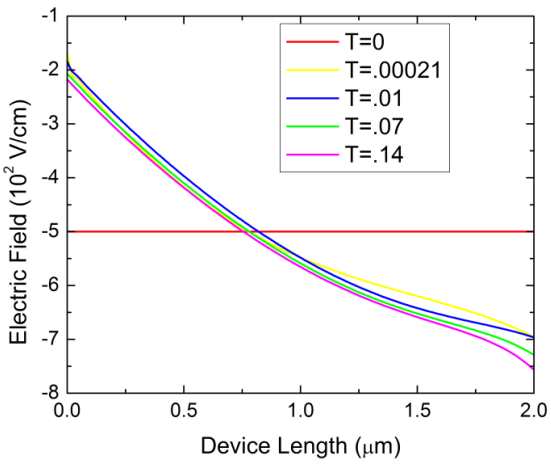

Figure 8.19: Temporal electric field profile evolution for case 4.

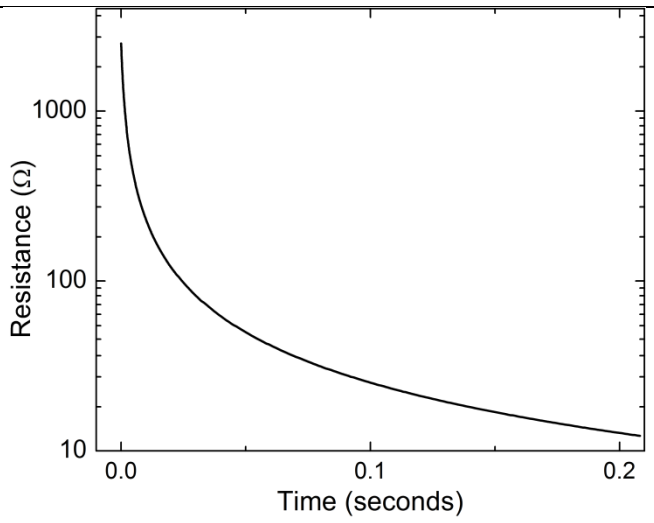

Figure 8.20: Transient resistance response for the Case 4 biased memristor.

The memristors simulated in cases 1-3 are volatile devices. This volatility is applicable in neuromorphic computing where the emulation of short-term synapses is necessary. However, there is still a need for a long-term, non-volatile memristor to approximate all synapses in the brain [175]. This non-volatility can be achieved if the memristive device is designed with sources and sinks for ions, such as an electrolyte, provided these sources and sinks are electrically isolated from the electronic conduction path. One such structure is modeled in case 4. By removing ions (dopants) via Li-soluble metallic contacts [153] or an electrolyte, larger resistance ranges can be achieved. Results of simulations from one such device with a constant lithium flux of 20 x 10^{17} ions $cm^{-2}s^{-1}$ extracted from the bottom electrode are shown in Figures 8.18 and 8.20 and show a significantly higher resistance change of 20,200%. Moreover, the majority of the resistance change occurs for a small amount of Li extraction as shown in Figure 8.20 where the resistance changes by an order of magnitude within 9 ms with 0.9% (9 x 10^{13}) lithium ions extracted. This rapid change suggests that such devices can be operated with

minimal ion motion induced mechanical stress and thus, could be reliable long term memory or neuromorphic computational element [135]. Since both the required voltage and the ionic programming current are small, devices of this type could be low power as well. The initial lithium concentration is homogenous throughout the device at 9.99 x 10^{21} atoms cm^{-3}. At time 0.01 seconds, the lithium concentration begins to decrease both at the grounded side of the device where lithium is being extracted and at the positively-biased edge of the device where lithium ions are being drifted away as shown in Figure 8.18. The depletion of lithium at the edge of the simulated memristor continues at later time steps along with that in the middle portion of the device though this depletion in the middle of the device occurs at a slower rate.

Initially, the electric field in the case 4 analog memristor is constant. The electric field changes rapidly from 0 s to 0.00021 s as shown in Figure 8.19. This rapid change in the electric field is due to the relationship between electrical resistivity and lithium concentration in lithiated metal oxides:

$$Resistivity = \frac{\mathbf{1}}{\mathbf{q\mu_p Li_{Vacancies}}} = \frac{\mathbf{1}}{\mathbf{q\mu_p (10^{22} - [Li])}} \tag{8.11}$$

where [Li] is the concentration of lithium in atoms/cm^3.

As lithium approaches stoichiometric concentrations, there is a rapid reduction in electrical conductivity. This rapid reduction in electrical conductivity near stoichiometric lithium levels has been confirmed and investigated experimentally in lithium transition-metal oxides [119, 122]. Thus, even though the concentration has barely changed from 0s to 0.00021 s, the electric field and resistivity is significantly changed as shown in Figures 8.19 and 8.20.

For times greater than 0s, the electric field is lower in magnitude at the anode than the rest of the device, while the electric field has the highest magnitude at the cathode. This electric field profile is due to the competition of drift and diffusion of holes that result from the gradients in doping created by the movement of lithium ions. Drift and diffusion are competing at the anode making the electric field greater while drift and diffusion coincide at the cathode resulting in a decreased electric field. Overall, the magnitude of the electric field increases as the simulation progresses, reflecting the decrease in overall resistance in the simulated memristor as shown in Figure 8.20.

8.7 Conclusions

A finite element model was introduced to describe the resistance response of a semiconductor analog memristor based on the drift and diffusion of mobile dopants. An analog resistance change in a semiconductor with mobile dopants can be achieved via both dopant extraction and the less obvious dopant redistribution within the device. Minor resistance changes can be achieved by varying initial concentration levels, device geometry, specifically the constrictive flow geometry described herein, and dependence of charge carrier mobility on ion concentration. However, for large resistance changes, ion extraction must be considered. The optimal regime for memristor operation is ion extraction provided that ions can be replaced with minimal loss of capacity or damage to the structure as happens in common thin film battery cathode semiconductors [125].

CHAPTER 9 : Conclusions and Future Directions

9.1 Conclusions

The research disseminated in this thesis focuses on lithiated transition metal oxide material synthesis, characterization, and memristive device simulation and fabrication. Multiple crystal growth methods including Sputtering, Molecular Beam Epitaxy, and high temperature Electrodeposition were employed. Additionally, these materials have been characterized with X-ray diffraction, profilometry, Synchrotron methods (EXAFS, NEXAFS), and electrochemical impedance spectroscopy among other methods. A simulation of the memristive devices has also been developed to determine the effects of different device designs using the finite element method. Finally, memristive devices were fabricated using lithographic techniques and investigated. The contributions from this research are listed below:

1. *First In-situ synchrotron characterization of an Analog Memristor:*

   The memristive mechanism of analog $LiNbO_2$ memristors has been investigated by an *in situ* O K-edge NEXAFS study. The memristance effect in the $LiNbO_2$ film is attributed to the movement of lithium, which is shown to have a concentration gradient in a biased $LiNbO_2$ memristor. This gradual movement and eventual graded concentration profile of lithium is responsible for both the analog and volatile nature of the $LiNbO_2$ memristor as confirmed via NEXAFS.

2. *Improved understanding of the Resistance Modulation Mechanism in $LiNbO_2$ Memristors:*

Although similar to memristors that rely on filamentary conduction in that vacancies are responsible for the resistance modulation, the gradual change in resistance sets the $LiNbO_2$ memristor apart in a new class of analog memristive devices void of conductive filaments which has been investigated with different AC, DC, and spectroscopic techniques. This filament-free mechanism should provide benefits in scaling and manufacturing in addition to being more directly applied to neuromorphic computing in a fashion analogous to mammalian brains.

3. *Development of a Finite Element Model to Describe $LiNbO_2$ Memristor Operation:*

A finite element model was introduced to describe the resistance response of a semiconductor memristor based on the drift and diffusion of dopants. A gradual analog resistance change in a semiconductor with mobile dopants can be achieved with both dopant extraction and the less obvious dopant redistribution in the device. From the proposed memristor model, it has been determined that geometry, dependence of charge carrier mobility on ion concentration, and boundary conditions play a role in the speed and the overall resistance change in the memristor.

4. *Improved understanding of the operation of ionic-electronic devices via EIS:*

The analog resistance change in an $LiNbO_2$ memristor has been characterized by EIS. It was shown that $LiNbO_2$ memristors exhibit analog

behavior and can exhibit memcapacitive and meminductive responses at certain frequency ranges. The PDEIS data suggests that the change in resistance of an analog $LiNbO_2$ memristor under the application of a DC bias is due to the drift of lithium atoms and thus a redistribution of dopants in the device. Additionally, it is shown that with increasing electric fields in the device, there is a larger resistance change and the majority of this resistance change occurs at the metal - semiconductor interface. Larger resistance changes have been shown herein to depend on higher electric fields and the dominance of interfacial properties on the operation of the $LiNbO_2$ analog memristor. The dominance of resistance response on electric field and interfacial properties suggest that the fabrication of analog memristors with negligible bulk dimensions will enhance analog memristor functionality.

5. *Liquid phase electro-epitaxial growth of $LiNbO_2$:*

The repeatability issues in the oxy-halide growth chemistry where a small deviation in precursor availability and a lack of the multiple necessary side-reactions can produce the incorrect phase or a multi-phase thin film. Methods to control and/or reduce variability in the MBE-based growth system are currently being investigated. It is because of these repeatability issues that other growth methods are concurrently being examined to reproducibly produce $LiNbO_2$ crystalline material. Through a molten salt synthesis technique, $LiNbO_2$ crystals have been grown [35].

6. *Investigation of new ionic-electronic device structures:*

An ion gated transistor is shown to have an analog electronic channel resistance that is dependent on the ion concentration in a solid state device. The ionic transistor made from a common battery cathode material, $LiCoO_2$, is investigated for use in devices that exploit the interaction between ions and electrons with applications in low-power neuromorphic computing and non-volatile memory. By exploiting the change in electronic conductivity that occurs when the lithium concentration in lithium metal oxide materials is varied, an ionic-electronic transistor device structure was developed. The ionic-electronic device structure is composed of a thin film of a lithiated transition metal oxide with three aluminum metal contacts on the thin film. Two of the aluminum contacts are be operated at a low voltage to sense the conductivity of the thin film while the third aluminum contact will be operated as part of a battery cell. The battery cell includes lithium reference and counter electrodes and a liquid electrolyte. The majority of the resistance change in $LiCoO_2$ occurs close to the stoichiometric point, and thus nanoscale $LiCoO_2$-based ionic electronic devices are expected to consume minimal power and avoid structural phase changes leading to improved reliability.

7. *Investigation of the radiation hardness of $LiNbO_2$-based memristors:*

The effects of X-ray and proton radiation on an $LiNbO_2$ analog memristor are investigated by I-V hysteresis, Electrochemical Impedance Spectroscopy, low-frequency AC voltage, and X-ray diffraction analysis. Both electrical and structural characterization of an irradiated memristor show that irradiation leads to an increased level of defects in the $LiNbO_2$ crystalline lattice. These radiation-induced defects facilitate faster lithium movement as shown by electrochemical impedance spectroscopy measurements on the as-grown and irradiated memristor. X-ray radiation improves ionic motion in the bulk of the device and increases the ionic resistance at the $LiNbO_2$-metal interface. In the case of proton radiation, the memristance response improves due to an increase in ionic motion in the bulk and at the interfaces. It is also shown by Monte Carlo simulations that proton irradiation of $LiNbO_2$ results in structural damage, which was verified experimentally by an X-ray diffraction study.

9.1 Future Directions

Although the research presented in this thesis has brought us closer to utilizing lithiated transition metal oxides to perform computations similarly to the mammalian brain, several challenges still exist. Future work to continue the research in this thesis may include:

1. *Growth of large, planar $LiNbO_2$ crystals:*

The LPEE growth of $LiNbO_2$ presented in this thesis makes a huge advancement in the repeatable growth of $LiNbO_2$. However, if this material is going to be used in large-scale chips and devices that seek to compute similarly to the mammalian brain, larger crystals of $LiNbO_2$ will need to be synthesized.

2. *Fabrication of Nano-scale $LiNbO_2$ Memristors:*

As theorized from the EIS data presented herein, smaller memristors should have an improved memristance response. If planar $LiNbO_2$ surfaces can be achieved via thin film growth techniques or polishing of bulk materials, nanoscopic (100's of nm) memristors should facilitate improved memristive responses.

3. *Greater temperature control of MBE growth constituents:*

Planar thin films of $LiNbO_2$ can also be grown using the Oxy-halide growth chemistry discussed in Chapter 4 of this dissertation. However, if single phase $LiNbO_2$ is required, greater control of the delivery of growth constituents will be required. A newly designed $NbCl_5$ source should assist in providing this control, and will hopefully improve the repeatability of the oxy-halide MBE growth system.

4. *In-situ Auger probe of MBE growths for real-time chemical information :*

Another option for improving the growth of $LiNbO_2$ is the in-situ Auger probe as detailed in reference [176]. This tool, which has already been installed and calibrated on the oxy-halide Gen II MBE system, has the capability of determining sub-monolayer chemical information. This probe, along with improved growth constituent control, could drastically improve our knowledge of the MBE growth of lithiated transition metal oxides.

5. *A Quantitative Analog Memristor Model :*

The analog memristor model described herein has been instrumental in furthering our understanding of $LiNbO_2$-based memristors, but it is a qualitative model. Qualitative memristance response trends for initial ion concentration, hole mobility dependence on acceptor concentration, geometry, and ion extraction obtained using this qualitative model will guide future optimized implementations of $LiNbO_2$ memristors. However, the resistance changes and timescales in the model are not consistent with $LiNbO_2$ memristive device implementations. A quantitative model would more accurately describe the memristance response of $LiNbO_2$ memristors. In order to create a quantitative model, extensive research into the kinetics of lithium ion motion in $LiNbO_2$ need to be studied including the lithium ion diffusion coefficient for all lithium concentration levels as well as an in depth understanding of lithium ion motion in different $LiNbO_2$ crystalline

defects. Once these experimental parameters are determined, a quantitative model may be implemented, which could further guide the development of optimized $LiNbO_2$ memristors.

Appendix A: MBE System Maintenance and Growth Manual

In order to maintain continuity in MBE growth and maintenance procedures for future students, the growth manual that follows was developed. Before this growth manual was created, many of the procedures for the oxide MBE system were undocumented and passed on orally. Because errors can be extremely costly in both time and money, the documentation of each step is extremely important for continued operation of the oxy-halide MBE system.

A.1 Plasma Supply and Components

Components and cooling water loop explained:

Bath: Distilled Water

Figure A.1: Distilled water bath. This is the water reservoir for the plasma water supply.

Pump: Drip machine oil in back and front holes every couple of months

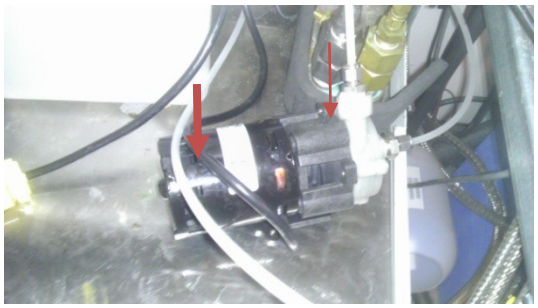

Figure A.2: Plasma cooling water pump. Machine oil needs to be dripped into the back and front holes every couple of months of use.

Figure A.3: Intercooler: water from the chase has brass connectors while water to the plasma has stainless swagelok connectors

Water flow operation:

1) Water is pulled from the bath to the motor.

2) The motor pushes water through the intercooler.

3) Afterwards, water exits the intercooler.

4) Water then goes into bottom water inlet into the cooling coil.

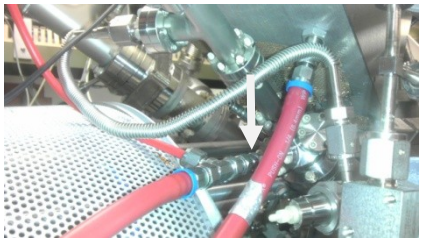

Figure A.4: Water flows into the plasma coil on the bottom swagelok connector.

5) Water comes out of coil and cools the capacitor bank. The plasma cooling water then comes back out of the return.

6) After water leaves the coil, it enters the flowmeter.

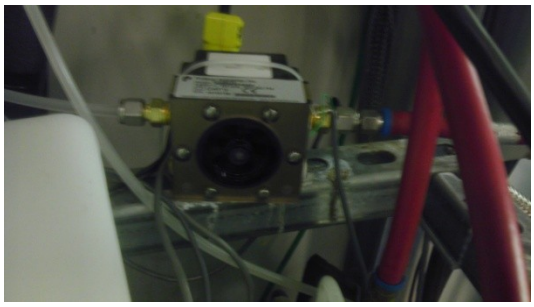

Figure A.5: Plasma cooling water flowmeter.

7) The water exiting the flowmeter dumps back into the distilled water reservoir bath.

To Purge Plasma

1) First, unplug the water pump.

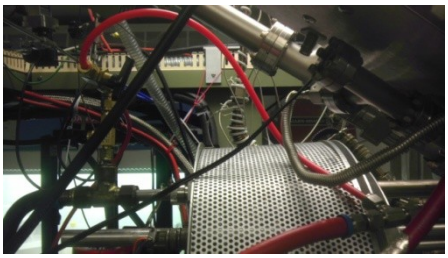

Figure A.6: (Red) Nitrogen purge line for the plasma cooling water.

2) Open the Red N_2 line going into the water input to the plasma source.

3) Close the N_2 valve used to purge the water

To Restart Water flow through plasma

1) Disconnect the pump to intercooler connection and suck on the water line until you see water flowing through the pump.

2) Water will need to be flowing a while before the interlock is tripped on the plasma supply.

A.2 Oxide MBE Current Limits

It is important to operate the oxide MBE cells within the manufacturer's specifications. Sometimes, it may be best to operate the cells at a lower temperature to preserve the life of the tantalum filaments. The current limits for different sources are listed below as a guide and may need to be updated depending on the vendor of the system components:

Substrate: Idle: 1A

Active: 5.5A

Li Tip (Always hotter than the bulk):

Idle: 1.2A (200 degrees C)

Active: 4.2A

Li Bulk Idle: 1A (150C)

Max: 8A

Vapor Source Tip: Idle: 1.5A

Active: ~4A, 12V

High Temp Cell: Idle: 4A (150 C)

Active: refer to manual

Normal Effusion Cell: Idle: 2A (150C)

Active: refer to manual

A.3 Venting and Baking the Oxide MBE System

Venting the System

1) Cool all of the cells and the substrate to room temperature. Set all the power supplies to standby. For the Li Tip, ramp down power at 5-10 degrees/min

2) Warm up the cryopanels and turn off the ion pump. Monitor the substrate temperature to ensure that the system is at room temperature. Expect this to take 8-12 hours.

2a) Close the RHEED isolation manual gate valve.

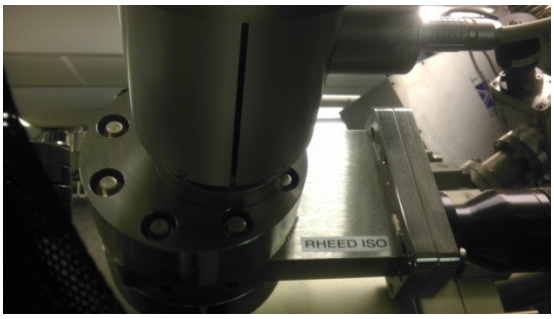

Figure A.7: Rheed isolation valve. Manually close this valve before venting the system

Close the RGA isolation manual gate valve.

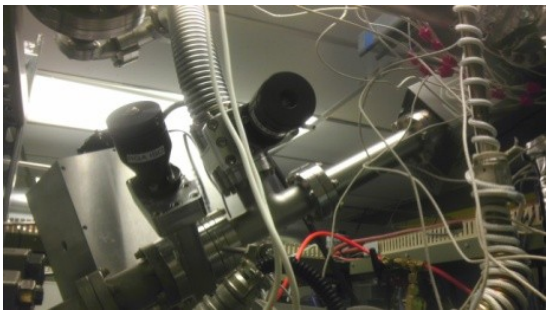

Figure A.8: RGA isolation valve (Left) and RGA pumping valve (Right). Close the RGA isolation valve and open the RGA pumping valve before venting to avoid venting the pumping manifold with the second cryopump.

Open the RGA manual pumping gate valve.

Close the vapor source isolation valve.

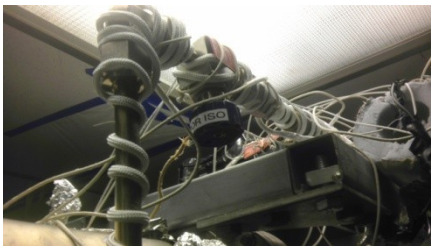

Figure A.9: RGA isolation valve (Left) and RGA pumping valve (Right). Close the RGA isolation valve and open the RGA pumping valve before venting to avoid venting the pumping manifold with the second cryopump.

3) Drain the water in the plasma cooling coil (See plasma section of manual) and drain the water in the wagon wheel.

To drain the water in the wagon wheel:

1) Valve off the water going to the supply and return of the wagon wheel.

Figure A.10: Valves controlling chilled water going to the supply and return of the wagon wheel. *Note: this has changed since the picture was taken and is now on the water manifold

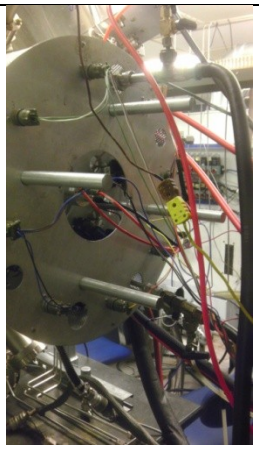

Figure A.11: Valve off the water lines coming off of the wagon wheel.

2) Place the 2 clear drain lines coming off of the wagon wheel supply and return and put them in a bucket to drain.

3) Barely open the red N_2 line to draw some water out of the wagon wheel.

4) Disconnect the top swagelok fitting and let gravity drain the rest of the water out of the wagon wheel.

5) Disconnect the bottom drain swagelok fitting and the small swagelok fitting.

4) Valve off and drain the water from the water cooled cells including the Li Cracker.

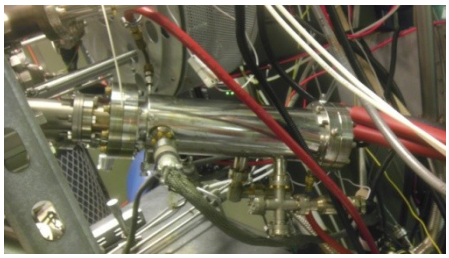

Figure A.12: Li cracker cell. Drain the water from this cell before venting to bake.

5) Once the substrate heater reads room temperature on the thermocouple, vent the chamber by following the steps below:

1) Turn off the cold cathode gauge.

2) Open the N_2 vent and make sure gas is coming out of the check valve.

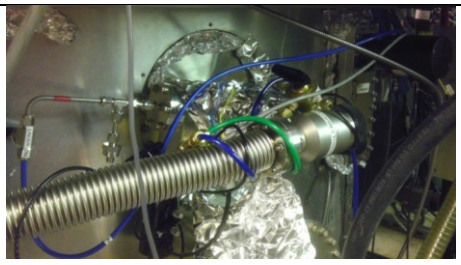

Figure A.13: Valves used to vent the chamber located at the bottom of the system on the side of the fume hood.

3) Open the Growth vent valve. This valve is pneumatically actuated.

Figure A.14: Growth vent valve.

4) You can be sure that the chamber is vented once you hear hissing coming from the check valve.

Plug Ins for Heaters for the Baking of the MBE system

1) Plug in the growth chamber heater into the receptacle on the bakeout panels.

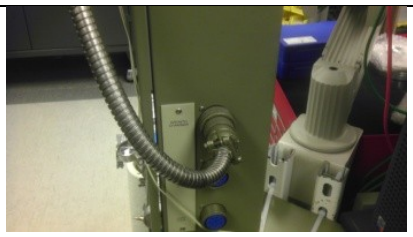

Figure A.15: Plug bakeout boxes into the power receptacle.

2) The sump and under sump heaters should already be in place and plugged in.

After opening maintenance is complete, prepare for baking by following the steps below:

1) Close the growth chamber vent gate valve.

Figure A.16: Plug bakeout boxes into the power receptacle.

2) Close the N_2 Vent valve.

3) Make sure the roughing throttle valve is completely closed.

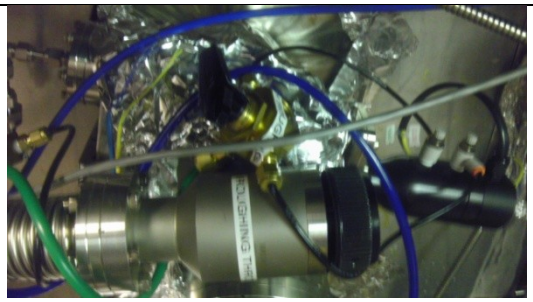

Figure A.17: Growth chamber rough pump throttle valve.

4) Open the growth roughing gate valve.

5) Ensure that the load lock turbo gate valve is closed and the load lock turbo roughing gate is closed (you shouldn't be able to see the red pin poking out).

6) Open the roughing throttle a little and listen for a change in pitch in the mech pump - keep the pressure in the roughing manifold under 300-400 Torr.

7) Perform as many Pump/Purge (steps 8-10) cycles as required.

8) Once the TC roughing gauge flattens out (<200 mTorr) close the growth roughing valve, open the N_2 vent valve, then open the growth vent gate valve.

9) While the growth chamber is venting, close the roughing throttle valve.

10) Once N_2 is flowing from the check valve again, go back to step 1 and repeat pump/purge a few times.

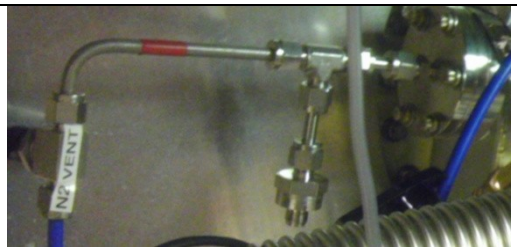

Figure A.18: Photograph of the nitrogen check valve. This should be hissing once the chamber is vented.

11) Close the growth roughing valve.

12) If the cryopump is already cold, open the cryopump gate valve (you may need to push reset on the right of gate valve switch to start it up). If the cryopump is not cold, cool it down and then open the cryopump gate valve.

13) Wait 5 minutes then try to start the cold cathode gauge (CCG).

If the CCG reads less than 800V, the system is not below 10^{-3} Torr, and you probably have a gross leak in the system. If this happens, close the gate valve to the cryopump, open up the growth roughing valve, and watch the foreline pressure while squirting the joints of the growth chamber with methanol.

14) After the system is on the cryopump and the CCG is reading, do another leak check with methanol.

15) Let the system pump on the cryopump overnight.

16) After the system has pumped on the cryopump overnight, it should be in the 10^{-5} Torr range. If it is not in this range, leak check with methanol/He again.

17) Close the RGA pump out port valve.

18) Open the RGA isolation valve (only start RGA if chamber pressure is less than 5e-5 Torr).

19) Do a He leak check by spraying He in the joints of the growth chamber.

20) Once no leaks are present, set up for baking the growth chamber.

Baking Checklist

1) Al foil goes over all windows, ceramic feedthroughs, and shutter manipulators.

2) Remove the overhead light from the growth chamber.

3) Remove the plasma matching network by following the steps outlined below:

A) Take off the outer panel by removing the housing screws first.

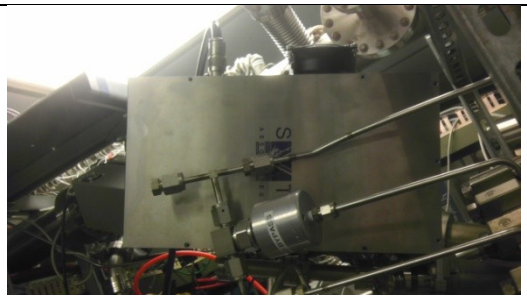

Figure A.19: The plasma supply before removing the outer panel.

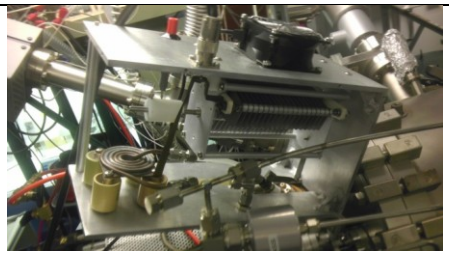

Figure A.20: The plasma supply after removing the outer panel.

B) Disconnect the power cable from the plasma fan.

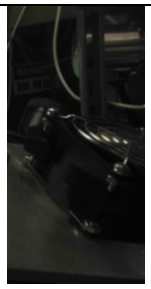

Figure A.21: Disconnect the power from the plasma fan before baking.

C) Disconnect the water supply and return connections.

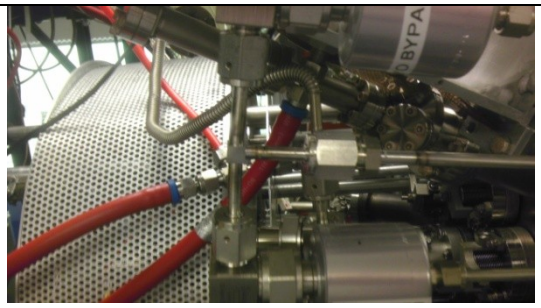

Figure A.22: RF Plasma water supply and return (red water lines).

D) Disconnect the RF Power Cable.

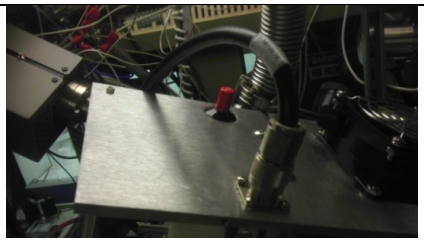

Figure A.23: RF power cable.

E) Disconnect the screw inside of the front hole of the plasma supply.

F) Disconnect the plastic water tube inside of the box that connects the outlet of the plasma coil water to the matching network (this is a Swagelok connection).

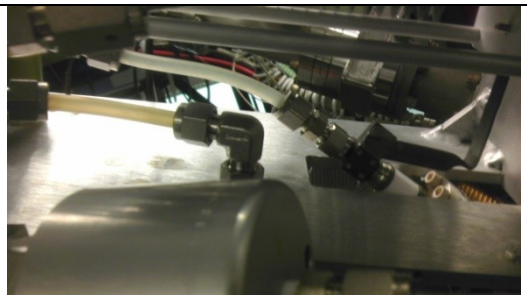

Figure A.24: Disconnect the water tube that connects the plasma coil to the matching network (connected to the ceramic tube in the figure above.

G) Remove the shielding from the plasma supply.

H) Remove the 2 screws in the front bottom and steady the box as these are the only things mechanically holding the supply in position.

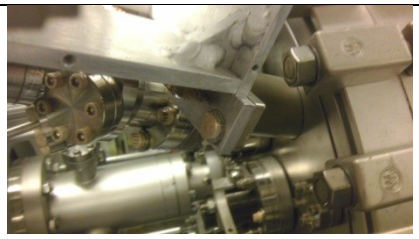

Figure A.25: Remove the two screws in the bottom of the front of the plasma supply.

I) Remove the box from the plasma supply by lifting backwards and upwards.

4) Disconnect the power cable connected to the Auger Probe.

5) Remove the 4 screws on the back of the auger probe and take off the plastic PMT.

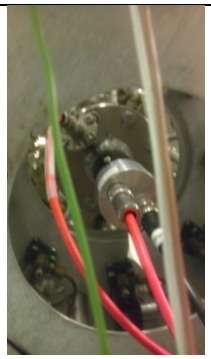

Figure A.26: Remove the four screws from the back of the auger probe and remove power.

6) Reattach the water cooling for the $NbCl_5$ Cell

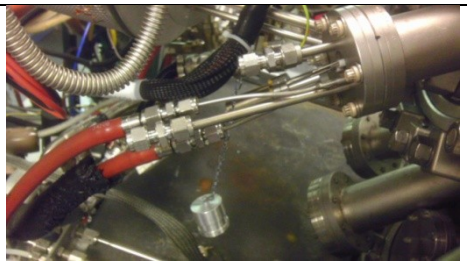

Figure A.27: Attach the cooling water lines to the $NbCl_5$ cell.

7) Reattach the thermocouples and power supplies to all of the cells in the system.

8) Increase the temperature of all of the cells and substrate to 150° C at 10° C/minute.

9) Place the solid block (or a 2" wafer) on the substrate heater.

10) Close the RGA isolation gate valve.

11) Open the RGA pumping manual gate valve.

12) Remove the RGA electronics box by pulling it straight back.

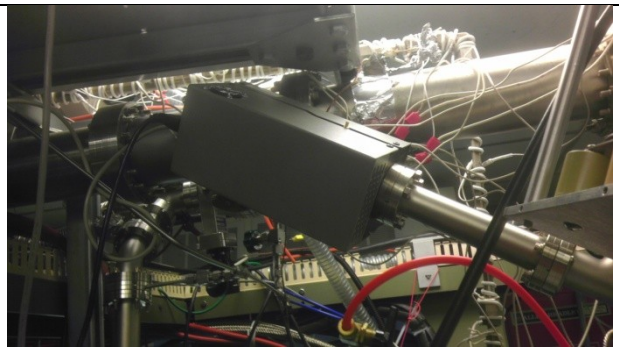

Figure A.28: Pull the RGA electronics box straight off of the system.

13) Remove the steering optics for the x and y axes off of the RHEED gun.

Figure A.29: Remove the steering optics off of the RHEED gun.

14) Disconnect the interlock from the back of the RHEED gun.

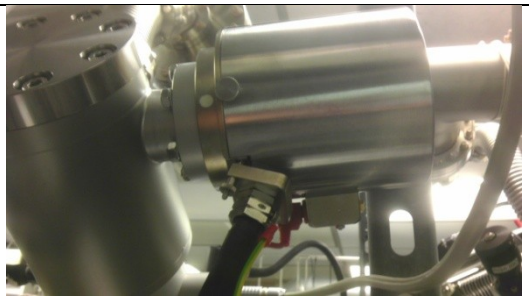

Figure A.30: Remove the interlock from the back of the RHEED gun.

15) Disconnect the plug on the RHEED gun by pulling straight back.

16) Disconnect the high voltage cable (this cable is covered with black mesh) from the RHEED gun.

17) Remove the motor from the substrate rotational feedthrough.

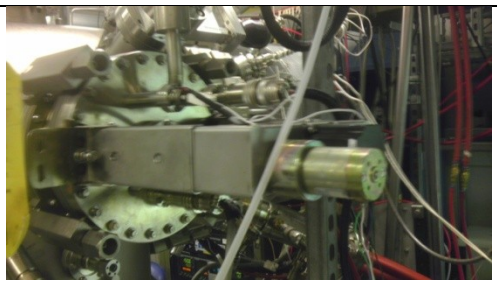

Figure A.31: Remove the interlock from the back of the RHEED gun.

18) Remove the flux gauge cable from the feedthrough on the manipulator.

Figure A.32: Photograph of the flux gauge cable connected to the feedthrough on the manipulator.

19) Clear the area around the growth chamber of any unbakable items.

20) Double check that all windows, ceramics, and rotational feedthroughs have foil covering them.

21) Make certain that the RHEED shutter screen is closed.

22) Put up the bake-out panels in the following order: the 2 front panels first followed by the sides, then top, then back.

23) Once the temperature of the cells and substrate reach 150° C, wait for the system pressure to come down.

24) Set the system bakeout timer above 0 (12 will work) and make sure hold is flipped to the "UP" position.

25) Turn the bake switch to the upward position. Try to get the ion pumps to stay on as quickly as possible and regenerate the cryopump shortly after the ion pumps are able to maintain vacuum by themselves.

26) Turn the growth chamber bakeout switch on.

27) Wait for the pressure in the growth chamber to go back down.

28) Turn the Sump switch to the on position.

29) Wait for the pressure to come back down while keeping the bakeout temperature below 150° C. This is controlled by the thermostat on the bakeout panel.

30) Turn the under sump switch to the on position.

Bringing the Bake Down

1) Set the temperature on the substrate and all of the cells to 0° C.

2) Reattach the shutter controls including the gray pneumatic line.

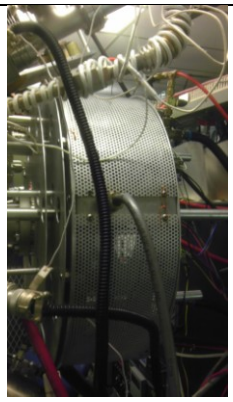

Figure A.33: Gray pneumatic shutter controller hookup for compressed air

3) Reattach cooling water to the system after all cells have reached 0° C.

4) Attach water cooling to the Li cell.

5) Attach the flux gauge cable to the manipulator feedthrough flange.

6) Attach liquid nitrogen to the cryopanel feedthroughs.

7) Attach the manipulator motors.

8) After the cryopanels have cooled down for an hour, outgas the cells and take flux measurements.

9) Reconnect the RHEED and plasma connections removed for the bakeout.

10) Open the vapor isolation valve.

Order Of Maintenance

1) Clean any dirty windows with water and dry with methanol then bake them in the 200° C oven for 30 minutes.

2) Repair any broken shutters.

3) Repair any gate valves or feedthroughs not on the CAR or source flanges.

4) Perform any repairs needed on the CAR.

5) Perform any repairs on the RGA, vapor injector, or plasma.

6) Remove any cells before doing shutter maintenance and load any empty cells.

7) Load cells with growth material in this order:

a) Lithium

b) All chlorides other than NiCl and NbCl

c) NiCl,

d) $NbCl_5$, which must be loaded in a glove bag and purged with nitrogen. If it is contaminated with air, it can oxidize and spoil.

8) Bake out the main chamber.

9) Fire the unloaded cells.

10) Load the cells in the growth chamber with the growth constituents.

11) Perform a final bake on the growth chamber.

Opening Li Cracker

1) Detach the Li cracker from the system by removing the nuts connecting it to the main chamber on the 2 3/4" flange.

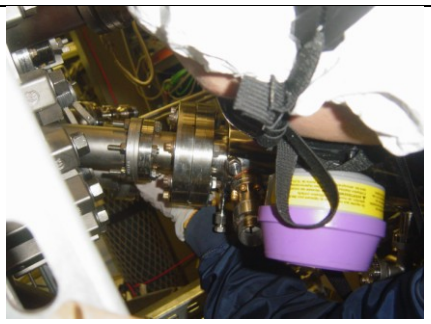

Figure A.34: Remove Li Cracker

2) Attach a blank to the system where the Li was removed to avoid growth chamber contamination.

3) Remove the needle from the cracker.

4) Wrap the fingers of the needle with Tantalum wire.

5) Remove the thermocouple from the cracker.

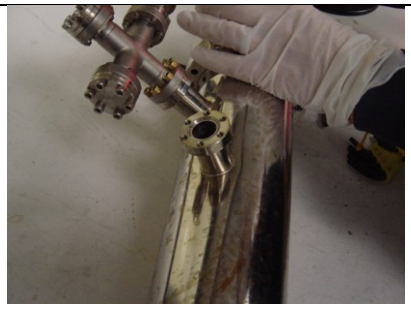

Figure A.35: Photograph of the lithium cracker with thermocouple removed

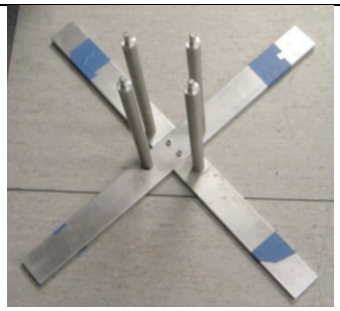

Figure A.36: Fully assembled Li cracker stand

6) Remove enough of the screws on the back of the cracker so that it can rest on the support (remove all but 2 screws).

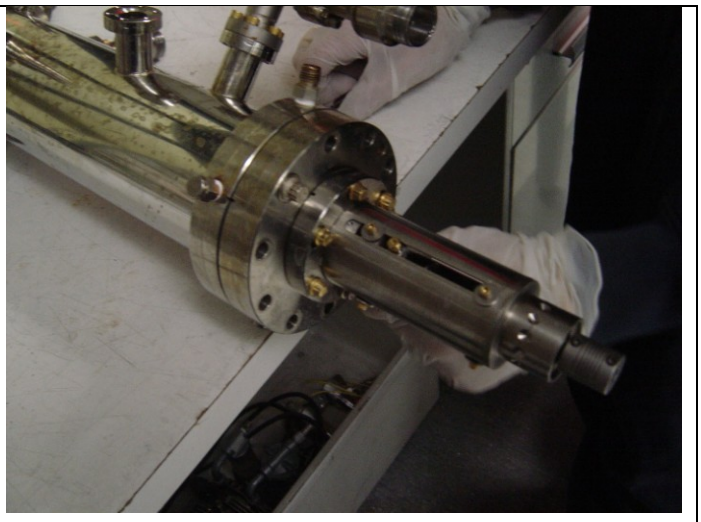

Figure A.37: Remove screws on the bottom of the cracker

7) Assemble the cracker support as shown in Figure A.36

8) Place the Li cracker on the assembled support.

9) Remove the rest of the screws on the back of cracker.

10) Lift the metal Li cracker housing straight off of cracker, being careful not to hit anything. The body filaments can easily be damaged in this process, so exercise extreme caution and do not force anything.

Figure A.38: Remove the base of the cracker

11) Test all of the filaments with an ohmmeter. They should be very low resistance

12) Remove the trombone from the Li cracker.

a) Unscrew the three screws securing the trombone.

b) Remove the trombone from the cracker.

13) Remove the ring beneath the trombone.

14) Reassemble the cracker without loading Li. Notice that larger diameter rods go through the smaller holes on the bottom

15) Test the resistance of the filaments with an ohmmeter.

16) Reassemble the Li source (the smaller gold screws go on bottom closest to the stand)

17) Attach the barrel connectors.

18) Test the filament connections with an ohmmeter. They should read somewhere around 2.5 ohms.

19) Connect the thermocouple.

20) Remove the blank from the growth chamber and attach the Li cracker to the system.

Clean and Rebuild Roughing Gate Valve on the Cryopump

1) Turn off the roughing pump after regenerating the cryopump (keep it warm). Remove the roughing line from back side of gate valve.

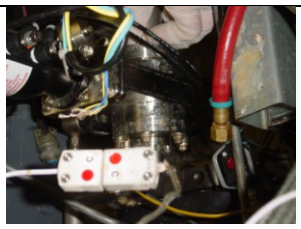

Figure A.39: Remove the roughing lines from the roughing gate valve.

2) Remove the elbow and take off the gate valve.

3) Remove the pneumatic valve and screw in the cap.

4) Look inside of and clean the tee connection.

5) Remove the elbow section of the gate valve.

6) Apply pressure to bottom pressure input to manually actuate the gate valve.

7) Unscrew the screws to open the bonnet.

8) Lift the gate valve out of its housing.

9) Carefully remove the gasket from the gate valve.

10) Clean all sealing surfaces.

11) Reassemble the gate valve.

Clean and Rebuild Gate Valve on Cryopump to Growth Chamber

1) Remove the bonnet by removing the screws on the side of the gate valve.

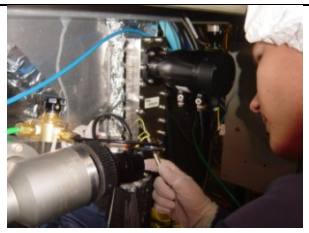

Figure A.40: Remove the bonnet

2) Clean the flapper as shown in Figure A.41.

Figure A.41: Remove the flapper and clean it

3) Clean the surface where the flapper seals (with a long stick with a texwipe).

4) Clean the gasket. If needed, remove the gasket and replace it.

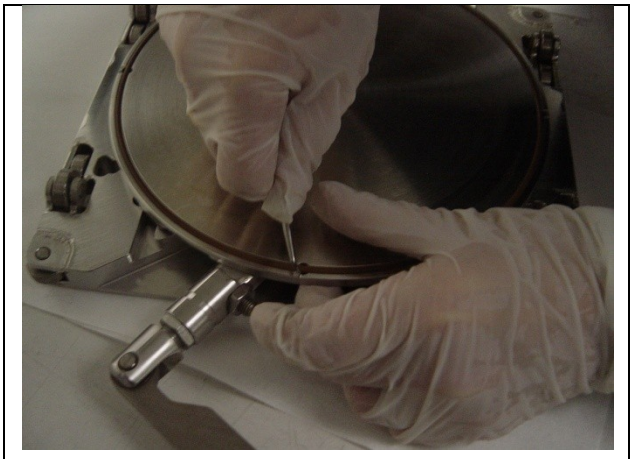

Figure A.42: Remove the gasket and replace it if needed.

Vapor Source Material Charging (Loading $NbCl_5$)

1) Remove the water heater lines from the NbCl5 source.

2) Close the roughing valve.

3) Open the purge valve.

4) Open the vent/pumping valve (blue).

5) Put on a respirator.

6) Close the vent/pumping valve.

7) Remove the NbCl cell from the system.

8) Remove the old $NbCl_5$ from the beaker.

9) Clean any deposits off of the knife edge.

10) Put the copper gasket with the full nipple back on the system.

11) Place the crucible in the full nipple.

12) Wipe down the contact between the full nipple and the sealing surface.

13) Clean a glass cutter and ampoule and ensure $NbCl_5$ is at the bottom of the ampoule.

14) Put the gasket on the fixed side of the cell.

15) Use the glass cutter to open the $NbCl_5$ by applying pressure and rotating the ampoule.

16) Pour $NbCl_5$ from the ampoule into the crucible.

17) Reattach the full nipple.

18) Use the mechanical pump to pull rough vacuum on the $NbCl_5$ chamber by following the steps below:

a) Close the purge valve.

b) Open the vent/pumping valve to equalize pressure.

c) Slowly open the roughing valve, keeping the pressure under 500 mTorr.

19) Hook up water lines from the heater bath to the $NbCl_5$ cell.

20) Use the water lines to actively cool the source.

21) Use the roughing pump until the pressure stabilizes, close the roughing pump, then switch to the cryopump.

22) After pumping with the cryopump for at least 12 hours, put the heating jacket back on and bake out the cell.

Sample Metallization and Oxidation

1) Deposit roughly 2 microns of Cr on the back of the intended growth wafers (DC Sputterer at ~3% power).

2) Make sure the cap is on the tube for the oxidation furnace and there is water flow (ensure using flowmeter on the wall) and N_2 flow (N_2 bypass flowmeter should be reading above 0).

STEPS 3 and 4 are only needed if you are wanting to verify the temp in the furnace. Otherwise, skip to step 5.

3) Insert the thermocouple into the hole in the cap.

Figure A.43: Insert the thermocouple in the hole in the glass cap.

4) Connect the thermocouple to the thermometer box.

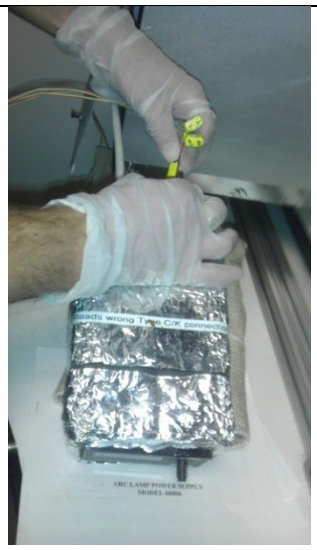

Figure A.44: Connect the thermocouple leads to the thermocouple readout box.

5) Turn on the power on the switches labeled "control" and "element".

Figure A.45: Turn on the power to the control and element portions of the furnace.

6) Increase the temperature setpoints until you see the current outputs go to "5" (zone 2 will peg out at the maximum of the scale until 90C).

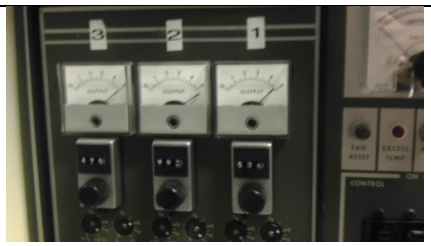

Figure A.46: Temperature controller. Increase the temperature setpoints.

7) Bring all three zones to 1000° C slowly. Approx values for the center zone to be 1000° C:

Zone 1:521

Zone 2:747

Zone 3:965

8) Unplug the thermometers.

9) The thermocouples will be very hot so put on the thermal gloves while removing them

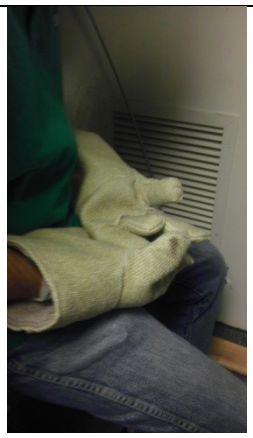

Figure A.47: When removing the thermocouple, put on thermal gloves to avoid burns.

10) Carefully remove the thermocouple tube and place it back in the PVC holder.

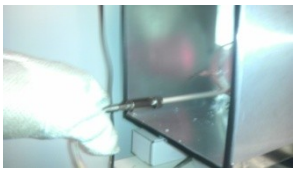

Figure A.48: Carefully remove the thermocouple tube and put it back in the PVC holder.

11) Take a texwipe and place it next to the tube.

12) Take the quartz cap off of the tube and place it on the texwipe.

Figure A.49: Use a texwipe to keep the tube cap clean.

13) Load the boat with the wafers to be oxidized. Maintain spacing between samples to maximize oxidation when loading the boat (3 spaces between wafers).

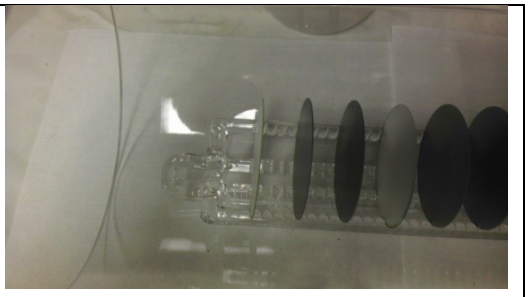

Figure A.50: Boat loaded with wafers to be oxidized. Maintain at least 3 spaces between wafers for equal oxidation.

14) Never plan on oxidizing the first wafer. This should be a placeholder wafer.

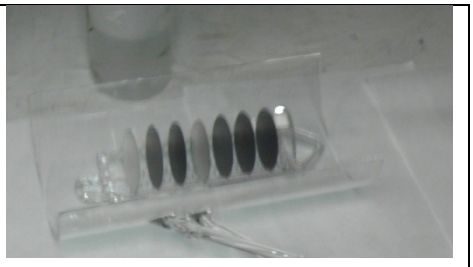

Figure A.51: Load a placeholder wafer in the first position in the boat.

15) Take the boat and holder and level it with the furnace tube

Figure A.52: Level the boat with the furnace tube.

16) Take the hook out of the PVC holder and push the boat into the tube such that the ASQ is aligned with the first dark ring.

Figure A.53: Push the boat into the tube such that the ASQ is aligned with the first dark ring in the tube and allow the boat to soak in the entrance of the tube for 5 minutes.

17) Let the boat soak at the entrance of the tube for 5 minutes.

18) Push the boat into the furnace until the black line on the hook is parallel with the entrance of the furnace and wait 15 minutes to let the temperatures equilibrate.

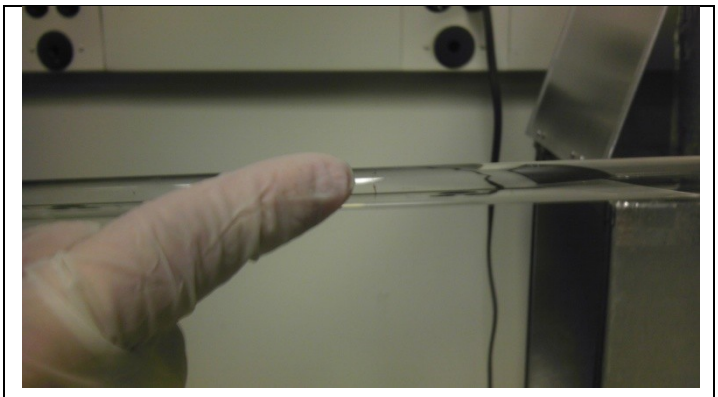

Figure A.54: Black line on the hook. Align this with the entrance of the furnace while oxidizing samples.

19) While waiting 15 minutes, put the cap on the furnace tube (not all the way, leave a little space so the CTE doesn't crack the tube).

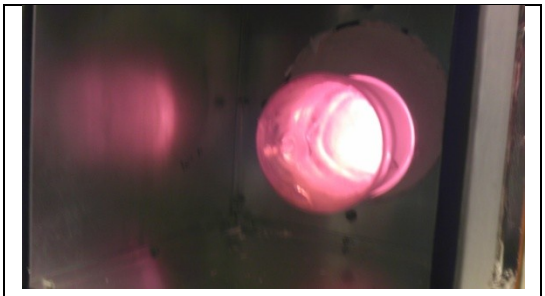

Figure A.55: Place the furnace cap back on the tube.

20) Connect O_2 to the furnace but don't tighten down on the swage.

Figure A.56: Connect oxygen to the furnace gas manifold.

21) Run the O_2 for a few seconds to purge the line, then tighten down on the oxygen connection.

22) After waiting for 15 minutes, switch off the N_2 bypass and switch on the O_2 (look at the flowmeters to confirm flow)

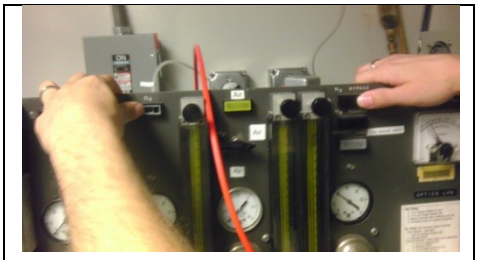

Figure A.57: After 15 minutes, switch the nitrogen off and the oxygen on. The flowmeters on the panel will confirm that you correctly switched the two.

23) Run O_2 for 20 minutes at 1000° C for 2 μm of chrome.

24) O_2 flowmeter should read "12" and N_2 bypass ball should be at the bottom of the flowmeter.

25) After 20 minutes, turn off the O_2 and turn on the N_2 bypass.

26) If you're not going to be using the system again, turn the temp setpoints to "0" and turn off the "element" and "control".

27) If you are going to be oxidizing more wafers, idle the settings to ~400 °C and remove the boat slowly (a few inches every few minutes).

RHEED

1) Turn on the power switch

2) Bring I_f up to 1.2A.

3) Bring voltage to 10kV.

4) Bring I_f to 1.5-1.55 (Max is 1.7A).

5) Switch to emission current and set current to about 10 μA.

Cleaning Samples

1) Fill both stage 1 (dirty) and stage 2 (clean) beakers mostly with water.

2) Fill a little with HF (10%).

3) Dump out both beakers.

4) Clean samples in stage 1 beaker with a 5:1 sufuric:hydrogen peroxide mix for 10 minutes at 120° C.

5) Rinse and repeat step 4 in the stage 2 beaker.

6) Rinse with water and dry with nitrogen.

Loading/Unloading Samples

1) Spin down the loadlock turbo.

2) Turn off the intro chamber cold cathode gauge in the labview software.

3) Unscrew the door of the load lock.

4) Turn on the N_2 valve.

5) Unload and load samples into the load lock.

6) Turn off the N_2 purge.

7) Close the load lock door (you might have to lift up a bit to create a good seal).

8) Open the roughing valve to the load lock.

9) Wait till the pressure in the load lock is below 1 Torr (read on roughing gauge).

10) Close the roughing to the load lock.

12) Open roughing to backside of load lock turbo.

13) Spin up turbo and open the load lock turbo gate valve.

Growth Procedure

1) Heat up the vapor source heater lines by plugging in the variac and slowly raising the Li bulk to 8A. Open the isolation and process valves on the vapor source. Set the temperature on the eurotherm on the Li bulk to attain required flux.

2) Close the cryopump to growth chamber gate valve.

3) Enable the shutter for the oxygen source.

4) Open the process valve for oxygen.

5) Wait until the pressure on the main chamber cryopump stops dropping at less than 180u.

6) Open cryopump to growth chamber gate valve and watch the pressure on the MKS controller- it should drop. If it does not drop, close the cryopump to growth chamber gate valve again and wait longer

7) Once the heater rope has heated the vapor source lines to >100C, start heating up the bath to desired temperature for required flux.

8) After both the NbCl bath and the Li bulk have stabilized (1 hour), take fluxes.

9) Flip the CAR to the growth position, and set the substrate current limit to 5/5.5 A.

10) Enable data logging.

11) Set the substrate to growth temperature (850° C traditionally) and wait until it stabilizes before applying oxygen.

12) To light the plasma if it is the first growth of the day, follow the steps below:

a) Set the power to 500W.

b) Make sure shutter enable is turned off.

c) Turn on the MFC, open the process and the shutter.

d) Turn the RF power on.

e) Tune the reflected power to 0 W.

f) Enable the shutter (should be done about 30 sec after step c).

g) Turn oxygen MFC to off from remote.

h) Wait until the reflective power jumps up.

I) Turn the oxygen MFC back to remote mode.

j) Set the plasma power down to 400 W.

k) Tune down the reflective power.

l) Open the oxygen shutter.

To light the plasma if it is not the first growth of the day:

a) Turn on the plasma at 500 W.

b) Tune down the reflected power.

c) Turn on the isolation valve, MFC, process valve, shutter enable, and shutter.

d) Turn MFC to off from remote.

e) After the plasma lights (reflected power shoots up), turn the MFC back to remote.

f) Tune down the reflected power.

g) Set the power to 400 W.

13) To initiate growth, open oxygen, Li, and vapor source shutters and hold for an hour.

Ending Growth

1) After the substrate temperature is less than 260° C, turn off the plasma.

2) Close the O_2 shutter, isolation, process, turn off MFC, and turn off the shutter enable.

3) Rotate the CAR 180°.

4) Perform a flux measurement and record the fluxes on a spreadsheet.

Regenerate Cryopump While the system is up

1) Close the load lock to turbo pump gate valve.

2) Close the backside of the turbo gate valve (manual valve).

3) Close the cryopump to the main chamber gate valve.

4) Begin a regeneration cycle on the cryopump controller.

Clean Intro Chamber Arm/Bearings - must have 2 standard bore (bigger) 2 3/4" gaskets (SEE PIC BELOW)

Figure A.58: Standard bore gaskets are required for this procedure (left).

1) Vent Intro Chamber

a) Close the load lock to turbo gate valve.

b) Close the back of the turbo pump to the roughing manifold (the red plastic piece should not be showing)

c) Loosen the load lock chamber door.

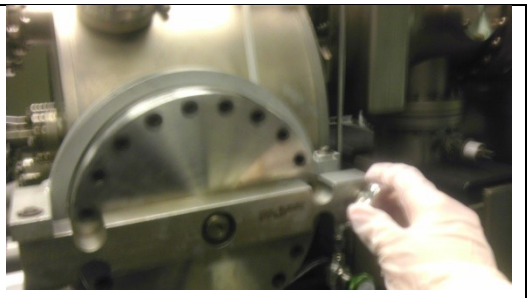

Figure A.59: Loosen loadlock chamber door.

d) Open the intro chamber N_2 Purge Valve Labeled "LL VENT".

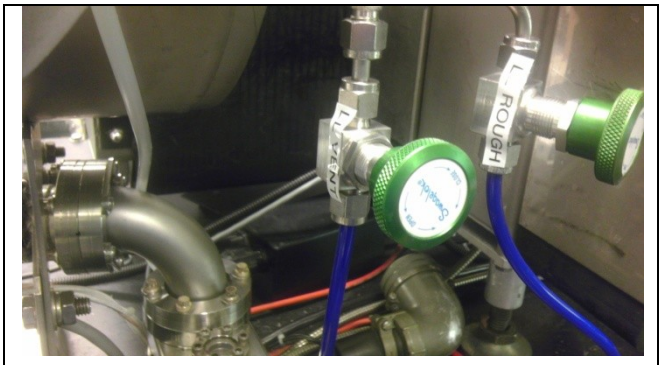

Figure A.60: Vent the loadlock by opening the valve labeled "LL VENT".

2) Remove the load lock claw by loosening 2 screws on the shaft coupler as shown in Figure A.61.

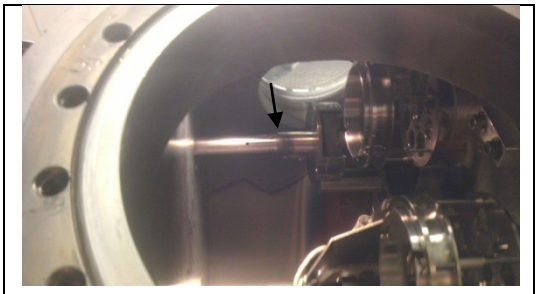

Figure A.61: Remove the claw by loosening the two screws on the shaft coupler in the load lock.

3) Pull the claw off of the arm after removing the two screws.

4) Take off the 2 3/4" flange holding the arm onto the system by removing the bolts on the 2 3/4" flange.

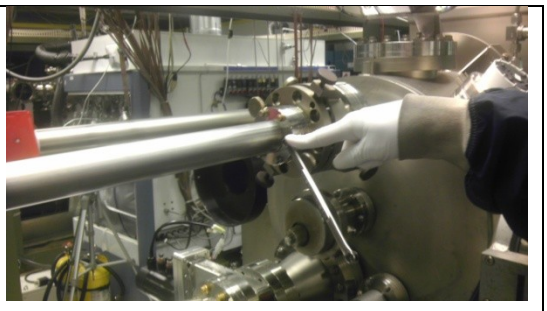

Figure A.62: Loosen the 2 3/4" flange holding the arm onto the system.

5) Remove the arm and place it on texwipes on a clean table. Be sure to keep the back end lower than the front end or the inside of the arm will fall out.

6) Pictures of the load lock arm bearing trapped in between the 2 standard gaskets.

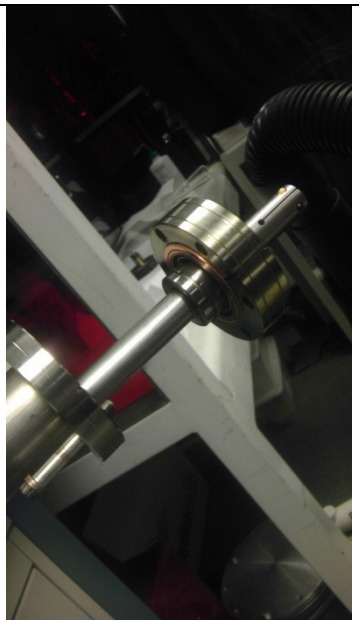

Figure A.63: The load lock bearing is held between two standard 2 3/4" flanges.

7) With a clean glove, remove the inside of the arm.

8) Place the inside of the arm down inside the fume hood.

9) Remove the copper gaskets on the arm (one by going forward, one by going backwards).

10) Test the front bearing for movement and rotation.

11) Test rear bearing (located by the magnet) for movement and rotation along with the smaller bearings in it.

12) Rinse everything with TCE.

13) If there are very rough parts of the inside of the arm, take 600 sandpaper and sand it down

14) Fill the arm holder partially with TCE and rinse it out.

15) Assemble the arm completely by following the steps below:

a) Put a gasket on the outer arm (arm holder).

b) Put the inside of the arm in where magnet goes to the bottom closed part.

16) Put the double sided flange and gasket on the assembly.

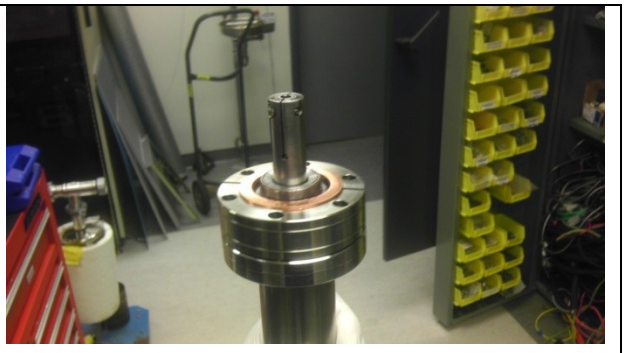

Figure A.64: Reassemble the load lock arm.

17) Install the whole arm back on the system with one bolt at the top while maintaining the gaskets in line (this is easier with multiple people).

18) Slowly tighten down the top 2 bolts.

19) Tighten all bolts and reattach the arm.

References

[1] S. E. Thompson and S. Parthasarathy, "Moore's law: the future of Si microelectronics," *Mater. Today,* vol. 9, no. 6, pp. 20-25, 2006.

[2] S. D. Ha and S. Ramanathan, "Adaptive oxide electronics: A review," *J. Appl. Phys.,* vol. 110, no. 7, p. 071101, 2011.

[3] G. Q. Zhang and A. van Roosmalen, *More than Moore: creating high value micro/nanoelectronics systems*: Springer, 2009.

[4] W. Arden, M. Brillouët, P. Cogez, M. Graef, B. Huizing, and R. Mahnkopf. (2010). *More than Moore*. Available: http://www.itrs.net/Links/2010ITRS/IRC-ITRS-MtM-v2%203.pdf

[5] L. O. Chua, "Memristor-the missing circuit element," *IEEE Trans. Circuit Theory,* vol. 18, no. 5, pp. 507-519, 1971.

[6] D. B. Strukov, G. S. Snider, D. R. Stewart, and R. S. Williams, "The missing memristor found," *Nature,* vol. 453, no. 7191, pp. 80-83, 2008.

[7] J. D. Greenlee, W. L. Calley, W. Henderson, and W. A. Doolittle, "Halide based MBE of crystalline metals and oxides," *Phys. Status Solidi C,* vol. 9, no. 2, pp. 155-160, 2012.

[8] F. Argall, "Switching phenomena in titanium oxide thin films," *Solid-State Electron.,* vol. 11, no. 5, pp. 535-541, 1968.

[9] A. Baikalov, Y. Q. Wang, B. Shen, B. Lorenz, S. Tsui, Y. Y. Sun, Y. Y. Xue, and C. W. Chu, "Field-driven hysteretic and reversible resistive switch at the Ag-$Pr_{0.7}Ca_{0.3}MnO_3$ interface," *Appl. Phys. Lett.,* vol. 83, no. 5, pp. 957-959, 2003.

[10] A. Beck, J. G. Bednorz, C. Gerber, C. Rossel, and D. Widmer, "Reproducible switching effect in thin oxide films for memory applications," *Appl. Phys. Lett.,* vol. 77, no. 1, pp. 139-141, 2000.

[11] W. R. Hiatt and T. W. Hickmott, "Bistable switching in niobium oxide diodes," *Appl. Phys. Lett.,* vol. 6, no. 6, pp. 106-108, 1965.

[12] C. N. Lau, D. R. Stewart, R. S. Williams, and M. Bockrath, "Direct observation of nanoscale switching centers in metal/molecule/metal structures," *Nano Lett.,* vol. 4, no. 4, pp. 569-572, 2004.

[13] S. Q. Liu, N. J. Wu, and A. Ignatiev, "Electric-pulse-induced reversible resistance change effect in magnetoresistive films," *Appl. Phys. Lett.,* vol. 76, no. 19, pp. 2749-2751, 2000.

[14] A. Odagawa, T. Kanno, and H. Adachi, "Transient response during resistance switching in Ag/$Pr_{0.7}Ca_{0.3}MnO_3$/Pt thin films," *J. Appl. Phys.,* vol. 99, no. 1, p. 016101, 2006.

[15] H. Sim, D. Choi, D. Lee, S. Seo, M.-J. Lee, I.-K. Yoo, and H. Hwang, "Resistance-switching characteristics of polycrystalline Nb_2O_5 for nonvolatile memory application," *IEEE Electron Device Lett.,* vol. 26, no. 5, pp. 292-294, 2005.

[16] C. Y. Lin, C. Y. Wu, C. Y. Wu, T. C. Lee, F. L. Yang, C. Hu, and T. Y. Tseng, "Effect of Top Electrode Material on Resistive Switching Properties of ZrO_2 Film Memory Devices," *IEEE Electron Device Lett.,* vol. 28, no. 5, pp. 366-368, 2007.

[17] U. Russo, D. Ielmini, C. Cagli, and A. L. Lacaita, "Filament conduction and reset mechanism in NiO-based resistive-switching memory (RRAM) devices," *IEEE Trans. Electron Devices,* vol. 56, no. 2, pp. 186-192, 2009.

[18] H.-J. Jang, O. A. Kirillov, O. D. Jurchescu, and C. A. Richter, "Spin transport in memristive devices," *Appl. Phys. Lett.,* vol. 100, no. 4, pp. 043510 - 043510-4, 2012.

[19] J. J. Yang, M. D. Pickett, X. Li, D. A. A. Ohlberg, D. R. Stewart, and R. S. Williams, "Memristive switching mechanism for metal/oxide/metal nanodevices," *Nat. Nanotechnol.,* vol. 3, no. 7, pp. 429-433, 2008.

[20] D.-H. Kwon, K. M. Kim, J. H. Jang, J. M. Jeon, M. H. Lee, G. H. Kim, X.-S. Li, G.-S. Park, B. Lee, S. Han, M. Kim, and C. S. Hwang, "Atomic structure of conducting nanofilaments in TiO_2 resistive switching memory," *Nat. Nanotechnol.,* vol. 5, no. 2, pp. 148-153, 2010.

[21] C. Mead, *Analog VLSI And Neural Systems*. New York: Addison-Wesley Publishing Company, 1989.

[22] C. Mead, "Neuromorphic electronic systems," *Proc. IEEE,* vol. 78, no. 10, pp. 1629-1636, 1990.

[23] R. A. Koene, "How to copy a brain," *New Scientist,* vol. 216, no. 2888, pp. 26-27, 2012.

[24] A. L. Hodgkin and A. F. Huxley, "A quantitative description of membrane current and its application to conduction and excitation in nerve," *J Physiol.,* vol. 117, no. 4, pp. 500-544, 1952.

[25] A. L. Hodgkin and A. F. Huxley, "Propagation of Electrical Signals Along Giant Nerve Fibres," *P. Roy. Soc. Lond. B Bio.,* vol. 140, no. 899, pp. 177-183, 1952.

[26] J. Barker, R. Pynenburg, R. Koksbang, and M. Y. Saidi, "An electrochemical investigation into the lithium insertion properties of Li_xCoO_2," *Electrochim. Acta,* vol. 41, no. 15, pp. 2481-2488, 1996.

[27] G. Meyer and R. Hoppe, "The First Oxoniobate (; III) $LiNbO_2$," *Angew. Chem. Int. Ed.,* vol. 13, no. 11, pp. 744-745, 1974.

[28] A. F. McDowell, D. M. Snyderman, M. S. Conradi, B. G. Silbernagel, and A. M. Stacy, "Cross relaxation and atomic motion in $LiNbO_2$," *Phys. Rev. B: Condens. Matter,* vol. 50, no. 21, pp. 15764-15774, 1994.

[29] N. Kumada, S. Muramatu, F. Muto, N. Kinomura, S. Kikkawa, and M. Koizumi, "Topochemical reactions of Li_xNbO_2," *J. Solid State Chem.,* vol. 73, no. 1, pp. 33-39, 1988.

[30] N. Kumada, S. Watauchi, I. Tanaka, and N. Kinomura, "Superconductivity of hydrogen inserted $LiNbO_2$," *Mater. Res. Bull.,* vol. 35, no. 11, pp. 1743-1746, 2000.

[31] M. J. Geselbracht, T. J. Richardson, and A. M. Stacy, "Superconductivity in the layered compound LixNbO2," *Nature,* vol. 345, no. 6273, pp. 324-326, 05/24/print 1990.

[32] H.-F. Roth, G. Meyer, Z. Hu, and G. Kaindl, "Synthesis, structure, and X-ray absorption spectra of Li_xNbO_2 and Na_xNbO_2 ($x \leq 1$)," *Zeitschrift für anorganische und allgemeine Chemie,* vol. 619, no. 8, pp. 1369-1373, 1993.

[33] D. L. Novikov, V. A. Gubanov, V. G. Zubkov, and A. J. Freeman, "Electronic structure and electron-phonon interactions in layered Li_xNbO_2 and Na_xNbO_2," *Phys. Rev. B: Condens. Matter,* vol. 49, no. 22, pp. 15830-15835, 1994.

[34] P. Bordet, E. Moshopoulou, S. Liesert, and J. J. Capponi, "Structure and physical properties of $Li_{1-x}NbO_2$ single crystals," *Physica C,* vol. 235–240, no. 2, pp. 745-746, 1994.

[35] E. G. Moshopoulou, P. Bordet, and J. J. Capponi, "Superstructure and superconductivity in $Li_{1-x}NbO_2$ ($x \approx 0.7$) single crystals," *Phys. Rev. B,* vol. 59, no. 14, pp. 9590-9599, 1999.

[36] E. R. Ylvisaker, K.-W. Lee, and W. E. Pickett, "Comparison of the electronic structures of two non-cuprate layered transition metal oxide superconductors," *Physica B,* vol. 383, no. 1, pp. 63-66, 2006.

[37] G. T. Liu, J. L. Luo, Z. Li, Y. Q. Guo, N. L. Wang, D. Jin, and T. Xiang, "Evidence of s-wave pairing symmetry in the layered superconductor $Li_{0.68}NbO_2$ from specific heat measurements," *Phys. Rev. B,* vol. 74, no. 1, p. 012504, 2006.

[38] Z. Xue, A. Dong, Y. Guo, and G. Che, "Structure and electrical characterization of $Li_{1-x}NbO_2$ superconductor with Tc = 14–17 K," *J. Alloy. Compd.,* vol. 476, no. 1–2, pp. 519-523, 2009.

[39] W. E. Henderson, W. L. Calley, A. G. Carver, H. Chen, and W. A. Doolittle, "A versatile metal-halide vapor chemistry for the epitaxial growth of metallic, insulating and semiconducting films," *J. Cryst. Growth,* vol. 324, no. 1, pp. 131-141, 2011.

[40] S. Singh, M. Tomar, Y. Ishikawa, S. Majumder, and R. Katiyar, "Density-Functional Theoretical Study on the Intercalation Properties of Layered $LiMO_2$ (M= Zr, Nb, Rh, Mo, and Ru)," in *MRS Proceedings*, 2004.

[41] C. Buchal, P. R. Ashley, and B. R. Appleton, "Solid-phase epitaxy of ion-implanted $LiNbO_3$ for optical waveguide fabrication," *J. Mater. Res.,* vol. 2, no. 2, pp. 222-230, 1987.

[42] X. Sun, B. Sun, L. Liu, N. Xu, X. Liu, R. Han, J. Kang, G. Xiong, and T. P. Ma, "Resistive switching in CeO_x films for nonvolatile memory application," *IEEE Electron Device Lett.,* vol. 30, no. 4, pp. 334-336, 2009.

[43] T. W. Hickmott, "Electron emission, electroluminescence, and voltage-controlled negative resistance in Al-Al_2O_3-Au diodes," *J. Appl. Phys.,* vol. 36, no. 6, pp. 1885-1896, 1965.

[44] K. L. Chopra, "Avalanche Induced Negative Resistance in Thin Oxide Films," *J. Appl. Phys.,* vol. 36, no. 1, pp. 184-187, 1965.

[45] D. Choi, D. Lee, H. Sim, M. Chang, and H. Hwang, "Reversible resistive switching of $SrTiO_x$ thin films for nonvolatile memory applications," *Appl. Phys. Lett.,* vol. 88, no. 8, p. 082904, 2006.

[46] L. Liborio and N. Harrison, "Thermodynamics of oxygen defective Magnéli phases in rutile: A first-principles study," *Phys. Rev. B,* vol. 77, no. 10, p. 104104, 2008.

[47] M. H. Lee and C. S. Hwang, "Resistive switching memory: observations with scanning probe microscopy," *Nanoscale,* vol. 3, no. 2, pp. 490-502, 2011.

[48] J. Duchene, "Direct infrared measurements of filament transient temperature during switching in vanadium oxide film devices," *J. Solid State Chem.,* vol. 12, no. 3-4, pp. 303-306, 1975.

[49] M. Noman, A. A. Sharma, Y. M. Lu, M. Skowronski, P. A. Salvador, and J. A. Bain, "Transient characterization of the electroforming process in TiO_2 based resistive switching devices," *Appl. Phys. Lett.,* vol. 102, no. 2, pp. 023507-4, 2013.

[50] J. J. Yang, F. Miao, M. D. Pickett, D. A. A. Ohlberg, D. R. Stewart, C. N. Lau, and R. S. Williams, "The mechanism of electroforming of metal oxide memristive switches," *Nanotechnol.,* vol. 20, no. 21, p. 215201, 2009.

[51] J. P. Strachan, M. D. Pickett, J. J. Yang, S. Aloni, A. L. D. Kilcoyne, G. Medeiros-Ribeiro, and R. S. Williams, "Direct Identification of the Conducting Channels in a Functioning Memristive Device," *Adv. Mater.,* vol. 22, no. 32, pp. 3573-3577, 2010.

[52] B. J. Choi, D. S. Jeong, S. K. Kim, C. Rohde, S. Choi, J. H. Oh, H. J. Kim, C. S. Hwang, K. Szot, R. Waser, B. Reichenberg, and S. Tiedke, "Resistive switching mechanism of TiO thin films grown by atomic-layer deposition," *J. Appl. Phys.,* vol. 98, no. 3, p. 033715, 2005.

[53] H. Zhang, B. Gao, B. Sun, G. Chen, L. Zeng, L. Liu, X. Liu, J. Lu, R. Han, J. Kang, and B. Yu, "Ionic doping effect in ZrO_2 resistive switching memory," *Appl. Phys. Lett.,* vol. 96, no. 12, pp. 123502-3, 2010.

[54] Y.-H. You, B.-S. So, J.-H. Hwang, W. Cho, S. S. Lee, T.-M. Chung, C. G. Kim, and K.-S. An, "Impedance spectroscopy characterization of resistance switching NiO thin films prepared through atomic layer deposition," *Appl. Phys. Lett.,* vol. 89, no. 22, pp. 222105-222105-3, 2006.

[55] E. Lehtonen, J. H. Poikonen, and M. Laiho, "Two memristors suffice to compute all Boolean functions," *Electron. Lett.,* vol. 46, no. 3, pp. 239-240, 2010.

[56] J. Borghetti, G. S. Snider, P. J. Kuekes, J. J. Yang, D. R. Stewart, and R. S. Williams, "'Memristive'switches enable 'stateful'logic operations via material implication," *Nature,* vol. 464, no. 7290, pp. 873-876, 2010.

[57] D. B. Strukov and K. K. Likharev, "Prospects for terabit-scale nanoelectronic memories," *Nanotechnology,* vol. 16, no. 1, p. 137, 2005.

[58] D. B. Strukov and K. K. Likharev, "CMOL FPGA: a reconfigurable architecture for hybrid digital circuits with two-terminal nanodevices," *Nanotechnology,* vol. 16, no. 6, p. 888, 2005.

[59] S. H. Jo, T. Chang, I. Ebong, B. B. Bhadviya, P. Mazumder, and W. Lu, "Nanoscale memristor device as synapse in neuromorphic systems," *Nano Lett.,* vol. 10, no. 4, pp. 1297-1301, 2010.

[60] Y. V. Pershin and M. Di Ventra, "Spin memristive systems: Spin memory effects in semiconductor spintronics," *Phys. Rev. B,* vol. 78, no. 11, p. 113309, 2008.

[61] W. Xiaobin, C. Yiran, X. Haiwen, L. Hai, and D. Dimitrov, "Spintronic Memristor Through Spin-Torque-Induced Magnetization Motion," *IEEE Electron Device Lett.,* vol. 30, no. 3, pp. 294-297, 2009.

[62] V. Erokhin, T. Berzina, and M. P. Fontana, "Hybrid electronic device based on polyaniline-polyethyleneoxide junction," *J. Appl. Phys.,* vol. 97, no. 6, p. 064501, 2005.

[63] T. Berzina, A. Smerieri, M. Bernabò, A. Pucci, G. Ruggeri, V. Erokhin, and M. P. Fontana, "Optimization of an organic memristor as an adaptive memory element," *J. Appl. Phys.,* vol. 105, no. 12, p. 124515, 2009.

[64] T. Berzina, V. Erokhin, and M. P. Fontana, "Spectroscopic investigation of an electrochemically controlled conducting polymer-solid electrolyte junction," *J. Appl. Phys.,* vol. 101, no. 2, p. 024501, 2007.

[65] G. F. Oster, "A note on memristors," *IEEE Trans. Circuits Syst.,* vol. 21, no. 1, p. 152, 1974.

[66] A. N. Dey, "Electrochemical Alloying of Lithium in Organic Electrolytes," *J. Electrochem. Soc.,* vol. 118, no. 10, pp. 1547-1549, 1971.

[67] S. Thakoor, A. Moopenn, T. Daud, and A. P. Thakoor, "Solid-state thin-film memistor for electronic neural networks," *J. Appl. Phys.,* vol. 67, no. 6, pp. 3132-3135, 1990.

[68] J. Von Neumann, *The computer and the brain*: Yale University Press, 2012.

[69] S. B. Jeff Hawkins, *On Intelligence*: Times Books, 2004.

[70] *SYNAPSE program*. Available: http://www.darpa.mil/Our_Work/DSO/Programs/Systems_of_Neuromorphic_Adaptive_Plastic_Scalable_Electronics_(SYNAPSE).aspx

[71] *Qualcomm to build neuro-inspired chips*. Available: http://www.technologyreview.com/news/520211/qualcomm-to-build-neuro-inspired-chips/

[72] P. Merolla, J. Arthur, F. Akopyan, N. Imam, R. Manohar, and D. S. Modha, "A digital neurosynaptic core using embedded crossbar memory with 45pJ per spike in 45nm," in *Custom Integrated Circuits Conference (CICC), 2011 IEEE*, 2011, pp. 1-4.

[73] J. Seo, B. Brezzo, L. Yong, B. D. Parker, S. K. Esser, R. K. Montoye, B. Rajendran, J. A. Tierno, L. Chang, D. S. Modha, and D. J. Friedman, "A 45nm CMOS neuromorphic chip with a scalable architecture for learning in networks of spiking neurons," in *Custom Integrated Circuits Conference (CICC), 2011 IEEE*, 2011, pp. 1-4.

[74] *CSER*. Available: http://cser.org/resources.html

[75] S.-C. Liu and T. Delbruck, "Neuromorphic sensory systems," *Curr. Opin. Neurobiol.,* vol. 20, no. 3, pp. 288-295, 2010.

[76] W. Bo and K. Boahen, "A silicon cochlea with active coupling," *IEEE T. Bio-Med. Circuits Syst.,* vol. 3, no. 6, pp. 444-455, 2009.

[77] C. Toumazou and P. Georgiou, "Bio-inspired semiconductors for early detection and therapy," in *Solid State Circuits Conference (A-SSCC), 2011 IEEE Asian*, 2011, pp. 129-132.

[78] T. G. Constandinou, J. Georgiou, and C. Toumazou, "A fully-integrated semicircular canal processor for an implantable vestibular prosthesis," in *Electronics, Circuits and Systems, 2008. ICECS 2008. 15th IEEE International Conference on*, 2008, pp. 81-84.

[79] T. G. Constandinou, J. Georgiou, and C. Toumazou, "A neural implant ASIC for the restoration of balance in individuals with vestibular dysfunction," in *Circuits and Systems, 2009. ISCAS 2009. IEEE International Symposium on*, 2009, pp. 641-644.

[80] J. M. Carmena, M. A. Lebedev, R. E. Crist, J. E. O'Doherty, D. M. Santucci, D. F. Dimitrov, P. G. Patil, C. S. Henriquez, and M. A. L. Nicolelis, "Learning to Control a Brain–Machine Interface for Reaching and Grasping by Primates," *PLoS Biol.,* vol. 1, no. 2, p. e42, 2003.

[81] J. K. Chapin, K. A. Moxon, R. S. Markowitz, and M. A. L. Nicolelis, "Real-time control of a robot arm using simultaneously recorded neurons in the motor cortex," *Nat. Neurosci.,* vol. 2, no. 7, pp. 664-670, 1999.

[82] M. A. Lebedev and M. A. L. Nicolelis, "Brain–machine interfaces: past, present and future," *Trends Neurosci.,* vol. 29, no. 9, pp. 536-546, 2006.

[83] *Nuclear-Powered Transponder for Cyborg Insect*. Available: http://spectrum.ieee.org/semiconductors/devices/nuclearpowered-transponder-for-cyborg-insect?utm_source=feedburner&utm_medium=feed&utm_campaign=Feed%3A+IeeeSpectrum+%28IEEE+Spectrum%29&utm_content=Google+Reader

[84] G. Snider, "Instar and outstar learning with memristive nanodevices," *Nanotechnol.,* vol. 22, no. 1, p. 015201, 2011.

[85] J. D. Greenlee, C. F. Petersburg, W. L. Calley, C. Jaye, D. A. Fischer, F. M. Alamgir, and W. A. Doolittle, "In-situ oxygen x-ray absorption spectroscopy investigation of the resistance modulation mechanism in $LiNbO_2$ memristors," *Appl. Phys. Lett.,* vol. 100, no. 18, p. 182106, 2012.

[86] R. Mogi, M. Inaba, Y. Iriyama, T. Abe, and Z. Ogumi, "*In Situ* Atomic Force Microscopy study on lithium deposition on nickel substrates at elevated temperatures," *J. Electrochem. Soc.,* vol. 149, no. 4, pp. A385-A390, 2002.

[87] W. S. Yoon, K. B. Kim, M. G. Kim, M. K. Lee, H. J. Shin, J. M. Lee, J. S. Lee, and C. H. Yo, "Oxygen Contribution on Li-Ion Intercalation-Deintercalation in $LiCoO_2$ Investigated by O K-Edge and Co L-Edge X-ray Absorption Spectroscopy," *J. Phys. Chem. B,* vol. 106, no. 10, pp. 2526-2532, 2002.

[88] J. G. Chen, "NEXAFS investigations of transition metal oxides, nitrides, carbides, sulfides and other interstitial compounds," *Surf. Sci. Rep.,* vol. 30, no. 1, pp. 1-152, 1997.

[89] W. Jaegermann and H. Tributsch, "Interfacial properties of semiconducting transition metal chalcogenides," *Prog. Surf. Sci.,* vol. 29, no. 1-2, pp. 1-167, 1988.

[90] J. B. Bates, N. J. Dudney, G. R. Gruzalski, R. A. Zuhr, A. Choudhury, C. F. Luck, and J. D. Robertson, "Fabrication and characterization of amorphous lithium electrolyte thin films and rechargeable thin-film batteries," *J. Power Sources,* vol. 43, no. 1-3, pp. 103-110, 1993.

[91] G. A. Ragoisha and A. S. Bondarenko, "Potentiodynamic electrochemical impedance spectroscopy," *Electrochim. Acta,* vol. 50, no. 7–8, pp. 1553-1563, 2005.

[92] M. Di Ventra, Y. V. Pershin, and L. O. Chua, "Circuit Elements With Memory: Memristors, Memcapacitors, and Meminductors," *Proc. IEEE,* vol. 97, no. 10, pp. 1717-1724, 2009.

[93] J. D. Greenlee, W. L. Calley, M. W. Moseley, and W. A. Doolittle, "Comparison of interfacial and bulk ionic motion in analog memristors," *IEEE Trans. Electron Devices,* vol. 60, no. 1, pp. 427-432, 2013. © 2013 IEEE. Reprinted, with permission, from J. D. Greenlee, W. L. Calley, M. W. Moseley, and W. A. Doolittle 2013.

[94] B. J. Neudecker, N. J. Dudney, and J. B. Bates, "“Lithium-Free” Thin-Film Battery with In Situ Plated Li Anode," *J. Electrochem. Soc.,* vol. 147, no. 2, pp. 517-523, 2000.

[95] S. S. Zhang, K. Xu, and T. R. Jow, "EIS study on the formation of solid electrolyte interface in Li-ion battery," *Electrochim. Acta,* vol. 51, no. 8–9, pp. 1636-1640, 2006.

[96] A. S. Bondarenko and G. A. Ragoisha, "EIS Spectrum Analyser, http://www.abc.chemistry.bsu.by/vi/analyser," 0.1b ed, 2008.

[97] K. Levenberg, "A method for the solution of certain problems in least squares," *Q Appl. Math.,* vol. 2, no. pp. 164-168, 1944.

[98] D. W. Marquardt, "An algorithm for least-squares estimation of nonlinear parameters," *J. Soc. Ind. Appl. Math.,* vol. 11, no. 2, pp. 431-441, 1963.

[99] M. G. S. R. Thomas, P. G. Bruce, and J. B. Goodenough, "Lithium mobility in the layered oxide $Li_{1-x}CoO_2$," *Solid State Ionics,* vol. 17, no. 1, pp. 13-19, 1985.

[100] Y.-M. Choi, S.-I. Pyun, J.-S. Bae, and S.-I. Moon, "Effects of lithium content on the electrochemical lithium intercalation reaction into $LiNiO_2$ and $LiCoO_2$ electrodes," *J. Power Sources,* vol. 56, no. 1, pp. 25-30, 1995.

[101] R. Alcántara, P. Lavela, J. L. Tirado, E. Zhecheva, and R. Stoyanova, "Recent advances in the study of layered lithium transition metal oxides and their application as intercalation electrodes," *J. Solid State Electr.,* vol. 3, no. 3, pp. 121-134, 1999.

[102] J. N. Reimers and J. R. Dahn, "Electrochemical and In Situ X-Ray Diffraction Studies of Lithium Intercalation in Li_xCoO2," *J. Electrochem. Soc.,* vol. 139, no. 8, pp. 2091-2097, 1992.

[103] H. J. Orman and P. J. Wiseman, "Cobalt(III) lithium oxide, $CoLiO_2$: structure refinement by powder neutron diffraction," *Acta Crystallogr. C,* vol. 40, no. 1, pp. 12-14, 1984.

[104] M. J. Geselbracht, A. M. Stacy, A. R. Garcia, B. G. Silbernagel, and G. H. Kwei, "Local environment and lithium ion mobility in lithium niobate ($LiNbO_2$): inferences from structure, physical properties, and NMR," *J. Phys. Chem.- US,* vol. 97, no. 27, pp. 7102-7107, 1993.

[105] Q. Lin, Q. Li, K. E. Gray, and J. F. Mitchell, "Vapor Growth and Chemical Delithiation of Stoichiometric $LiCoO_2$ Crystals," *Cryst. Growth Des.,* vol. 12, no. 3, pp. 1232-1238, 2012.

[106] S. V. Novikov and C. T. Foxon, "Plasma-assisted electroepitaxy of GaN layers from the liquid Ga melt," *J. Cryst. Growth,* vol. 354, no. 1, pp. 44-48, 2012.

[107] J. A. Campá, M. Vélez, C. Cascales, E. Gutiérrez Puebla, M. A. Monge, I. Rasines, and C. Ruíz-Valero, "Crystal growth of superconducting $LiTi_2O_4$," *J. Cryst. Growth,* vol. 142, no. 1–2, pp. 87-92, 1994.

[108] C. Natarajan, M. Sharon, C. Lévy-Clément, and M. Neumann-Spallart, "Electrodeposition of zinc selenide," *Thin Solid Films,* vol. 237, no. 1–2, pp. 118-123, 1994.

[109] G. Meyer and R. Hoppe, "Über Oxoniobate (III). II [1, 2]. Notiz zur Kenntnis von $NaNbO_2$," *Zeitschrift für anorganische und allgemeine Chemie,* vol. 424, no. 2, pp. 128-132, 1976.

[110] D. Elwell and H. Scheel, "Crystal growth from high-temperature solutions," no. 1975.

[111] C. H. Park, B.-H. Cheong, K.-H. Lee, and K. J. Chang, "Structural and electronic properties of cubic, 2H, 4H, and 6H SiC," *Phys. Rev. B,* vol. 49, no. 7, pp. 4485-4493, 1994.

[112] M. D. Pickett, G. Medeiros-Ribeiro, and R. S. Williams, "A scalable neuristor built with Mott memristors," *Nat. Mater.,* vol. 12, no. 2, pp. 114-117, 2013.

[113] J. C. Shank, J. D. Greenlee, M. B. Tellekamp, and W. A. Doolittle, "Volatile Memristive Systems in Neuromorphic Spike-Frequency Adaptation Circuitry," no. submitted for publication, 2013.

[114] J. D. Greenlee, J. C. Shank, M. Brooks Tellekamp, and W. Alan Doolittle, "Spatiotemporal drift-diffusion simulations of analog ionic memristors," *J. Appl. Phys.,* vol. 114, no. 3, pp. 034504-034504-9, 2013.

[115] S. Ramakrishnan, P. E. Hasler, and C. Gordon, "Floating gate synapses with spike-time-dependent plasticity," *IEEE Trans. Biomed. Circuits Syst.,* vol. 5, no. 3, pp. 244-252, 2011.

[116] P. Bergveld, "Development of an ion-sensitive solid-state device for neurophysiological measurements," *IEEE Trans. Biomed. Eng.,* vol. 17, no. 1, pp. 70-71, 1970.

[117] J. Lee, M. J. Panzer, Y. He, T. P. Lodge, and C. D. Frisbie, "Ion gel gated polymer thin-film transistors," *J. Am. Chem. Soc.,* vol. 129, no. 15, pp. 4532-4533, 2007.

[118] M. J. Panzer and C. D. Frisbie, "Exploiting Ionic Coupling in Electronic Devices: Electrolyte-Gated Organic Field-Effect Transistors," *Adv. Mat.,* vol. 20, no. 16, pp. 3177-3180, 2008.

[119] M. Ménétrier, I. Saadoune, S. Levasseur, and C. Delmas, "The insulator-metal transition upon lithium deintercalation from $LiCoO_2$: electronic properties and 7Li NMR study," *J. Mater. Chem.,* vol. 9, no. 5, pp. 1135-1140, 1999.

[120] J. Molenda, A. Stokłosa, and T. Bąk, "Modification in the electronic structure of cobalt bronze LixCoO2 and the resulting electrochemical properties," *Solid State Ionics,* vol. 36, no. 1–2, pp. 53-58, 1989.

[121] K. Mizushima, P. C. Jones, P. J. Wiseman, and J. B. Goodenough, "Li_xCoO_2 ($0<x<-1$): A new cathode material for batteries of high energy density," *Mater. Res. Bull.,* vol. 15, no. 6, pp. 783-789, 1980.

[122] L. Dahéron, R. Dedryvère, H. Martinez, M. Ménétrier, C. Denage, C. Delmas, and D. Gonbeau, "Electron Transfer Mechanisms upon Lithium Deintercalation from $LiCoO_2$ to CoO_2 Investigated by XPS," *Chem. Mater.,* vol. 20, no. 2, pp. 583-590, 2008.

[123] Y. Uchimoto, H. Sawada, and T. Yao, "Changes in electronic structure by Li ion deintercalation in $LiCoO_2$ from cobalt L-edge and oxygen K-edge XANES," *J. Synchrotron Radiat.,* vol. 8, no. 2, pp. 872-873, 2001.

[124] F. M. Alamgir, E. Strauss, M. denBoer, S. Greenbaum, J. F. Whitacre, C.-C. Kao, and S. Neih, "$LiCoO_2$ Thin-Film Batteries: Structural Changes and Charge Compensation," *J. Electrochem. Soc.,* vol. 152, no. 5, pp. A845-A849, 2005.

[125] T. Osaka and M. Datta, *Energy Storage Systems in Electronics* vol. 1. Amsterdam: Gordon and Breach, 2000.

[126] N. J. Dudney, "Solid-state thin-film rechargeable batteries," *Mater. Sci. Eng., B,* vol. 116, no. 3, pp. 245-249, 2005.

[127] B. Wang, J. B. Bates, F. X. Hart, B. C. Sales, R. A. Zuhr, and J. D. Robertson, "Characterization of Thin-Film Rechargeable Lithium Batteries with Lithium Cobalt Oxide Cathodes," *J. Electrochem. Soc.,* vol. 143, no. 10, pp. 3203-3213, 1996.

[128] Y.-I. Jang, N. J. Dudney, D. A. Blom, and L. F. Allard, "High-Voltage Cycling Behavior of Thin-Film $LiCoO_2$ Cathodes," *J. Electrochem. Soc.,* vol. 149, no. 11, pp. A1442-A1447, 2002.

[129] C. F. Petersburg, Z. Li, N. A. Chernova, M. S. Whittingham, and F. M. Alamgir, "Oxygen and transition metal involvement in the charge compensation

mechanism of $LiNi_{1/3}Mn_{1/3}Co_{1/3}O_2$ cathodes," *J. Mater. Chem.,* vol. 22, no. 37, pp. 19993-20000, 2012.

[130] C. F. Petersburg, R. C. Daniel, C. Jaye, D. A. Fischer, and F. M. Alamgir, "Soft X-ray characterization technique for Li batteries under operating conditions," *J. Synchrotron Radiat.,* vol. 16, no. 5, pp. 610-615, 2009.

[131] J. B. Bates, N. J. Dudney, B. Neudecker, A. Ueda, and C. D. Evans, "Thin-film lithium and lithium-ion batteries," *Solid State Ionics,* vol. 135, no. 1-4, pp. 33-45, 2000.

[132] M. Inaba, Y. Iriyama, Z. Ogumi, Y. Todzuka, and A. Tasaka, "Raman study of layered rock salt $LiCoO_2$ and its electrochemical lithium deintercalation," *J. Raman Spectrosc.,* vol. 28, no. 8, pp. 613-617, 1997.

[133] D. Aurbach, Y. Ein-Eli, O. Chusid , Y. Carmeli, M. Babai, and H. Yamin, "The Correlation Between the Surface Chemistry and the Performance of Li-Carbon Intercalation Anodes for Rechargeable 'Rocking-Chair' Type Batteries," *J. Electrochem. Soc.,* vol. 141, no. 3, pp. 603-611, 1994.

[134] E. Antolini, "$LiCoO_2$: formation, structure, lithium and oxygen nonstoichiometry, electrochemical behaviour and transport properties," *Solid State Ionics,* vol. 170, no. 3-4, pp. 159-171, 2004.

[135] G. G. Amatucci, J. M. Tarascon, and L. C. Klein, "CoO_2, The End Member of the Li_xCoO_2 Solid Solution," *J. Electrochem. Soc.,* vol. 143, no. 3, pp. 1114-1123, 1996.

[136] G. Indiveri, "Neuromorphic bistable VLSI synapses with spike-timingdependent plasticity," *Adv. Neur. In.,* vol. 15, no. pp. 1091-1098, 2002.

[137] R. Douglas, M. Mahowald, and C. Mead, "Neuromorphic Analogue VLSI," *Annu. Rev. Neurosci.,* vol. 18, no. 1, pp. 255-281, 1995.

[138] B. Choi, J. Yang, M. X. Zhang, K. Norris, D. Ohlberg, N. Kobayashi, G. Medeiros-Ribeiro, and R. Williams, "Nitride memristors," *Appl. Phys. A-Mater.,* vol. 109, no. 1, pp. 1-4, 2012.

[139] N. Gergel-Hackett, B. Hamadani, B. Dunlap, J. Suehle, C. Richter, C. Hacker, and D. Gundlach, "A flexible solution-processed memristor," *IEEE Electron Device Lett.,* vol. 30, no. 7, pp. 706-708, 2009.

[140] A. S. Zoolfakar, R. Ab Kadir, R. A. Rani, S. Balendhran, X. Liu, E. Kats, S. K. Bhargava, M. Bhaskaran, S. Sriram, S. Zhuiykov, A. P. O'Mullane, and K. Kalantar-zadeh, "Engineering electrodeposited ZnO films and their memristive

switching performance," *Phys. Chem. Chem. Phys.,* vol. 15, no. 25, pp. 10376-10384, 2013.

[141] I. Valov, E. Linn, S. Tappertzhofen, S. Schmelzer, J. van den Hurk, F. Lentz, and R. Waser, "Nanobatteries in redox-based resistive switches require extension of memristor theory," *Nat. Commun.,* vol. 4, no. p. 1771, 2013.

[142] S. John Paul, B. S. Dmitri, B. Julien, J. J. Yang, M.-R. Gilberto, and R. S. Williams, "The switching location of a bipolar memristor: chemical, thermal and structural mapping," *Nanotechnology,* vol. 22, no. 25, p. 254015, 2011.

[143] T.-W. Lee and J. H. Nickel, "Memristor resistance modulation for analog applications," *IEEE Electron Device Lett.,* vol. 33, no. 10, pp. 1456-1458, 2012.

[144] G. S. Snider, "Spike-timing-dependent learning in memristive nanodevices," in *IEEE International Symposium on Nanoscale Architectures*, 2008, pp. 85-92.

[145] N. Marjanović, M. Vujisić, K. Stanković, and P. Osmokrović, "Effects of heavy ion bombardment on TiO_2 memristor operation," *Radiat. Eff. Defect. S.,* vol. 166, no. 1, pp. 1-7, 2010.

[146] M. Vujisic, K. Stankovic, N. Marjanovic, and P. Osmokrovic, "Simulated effects of proton and ion beam irradiation on titanium dioxide memristors," *IEEE Trans. Nucl. Sci.,* vol. 57, no. 4, pp. 1798-1804, 2010.

[147] E. DeIonno, M. D. Looper, J. V. Osborn, and J. W. Palko, "Displacement damage in TiO_2 memristor devices," *IEEE Trans. Nucl. Sci.,* vol. 60, no. 2, pp. 1379-1383, 2013.

[148] B. Butcher, X. He, M. Huang, Y. Wang, Q. Liu, H. Lv, M. Liu, and W. Wang, "Proton-based total-dose irradiation effects on Cu/HfO_2:Cu/Pt ReRAM devices," *Nanotechnology,* vol. 21, no. 47, p. 475206, 2010.

[149] D. Lee, J. Lee, S. Jung, S. Kim, J. Park, K. P. Biju, M. Choe, T. Lee, and H. Hwang, "Proton irradiation effects on resistive random access memory with ZrO_x/HfO_x Stacks," *IEEE Trans. Nucl. Sci.,* vol. 58, no. 6, pp. 3317-3320, 2011.

[150] W. M. Tong, J. J. Yang, P. J. Kuekes, D. R. Stewart, R. S. Williams, E. DeIonno, E. E. King, S. C. Witczak, M. D. Looper, and J. V. Osborn, "Radiation hardness of TiO_2 memristive junctions," *IEEE Trans. Nucl. Sci.,* vol. 57, no. 3, pp. 1640-1643, 2010.

[151] Y. Wang, L. Hangbing, W. Wang, Q. Liu, S. Long, W. Qin, H. Zongliang, Z. Sen, L. Yingtao, Z. Qingyun, L. Wentai, Y. Jianhong, and M. Liu, "Highly stable radiation-hardened resistive-switching memory," *IEEE Electron Device Lett.,* vol. 31, no. 12, pp. 1470-1472, 2010.

[152] Y. Gonzalez-Velo, H. J. Barnaby, A. Chandran, D. R. Oleksy, P. Dandamudi, M. N. Kozicki, K. E. Holbert, M. Mitkova, M. Ailavajhala, and P. Chen, "Effects of cobalt-60 gamma-rays on Ge-Se Chalcogenide glasses and Ag/Ge-Se test structures," *IEEE Trans. Nucl. Sci.,* vol. 59, no. 6, pp. 3093-3100, 2012.

[153] M. Winter and J. O. Besenhard, "Electrochemical lithiation of tin and tin-based intermetallics and composites," *Electrochim. Acta,* vol. 45, no. 1-2, pp. 31-50, 1999.

[154] L. O. Chua and S. M. Kang, "Memristive devices and systems," *Proc. IEEE,* vol. 64, no. 2, pp. 209-223, 1976.

[155] J. D. Greenlee, J. C. Shank, M. B. Tellekamp, E. X. Zhang, J. Bi, D. M. Fleetwood, M. L. Alles, R. D. Schrimpf, and W. A. Doolittle, "Radiation Effects on $LiNbO_2$ Memristors for Neuromorphic Computing Applications," *IEEE Trans. Nucl. Sci.,* vol. 60, no. 6, pp. 1-8, 2013. © 2013 IEEE. Reprinted, with permission, from J. D. Greenlee, J. C. Shank, M. B. Tellekamp, E. X. Zhang, J. Bi, D. M. Fleetwood, M. L. Alles, R. D. Schrimpf, and W. A. Doolittle 2013.

[156] N. Balke, S. Jesse, A. Morozovska, E. Eliseev, D. Chung, Y. Kim, L. Adamczyk, R. Garcia, N. Dudney, and S. Kalinin, "Nanoscale mapping of ion diffusion in a lithium-ion battery cathode," *Nat. Nanotechnol.,* vol. 5, no. 10, pp. 749-754, 2010.

[157] M. E. Orazem and B. Tribollet, *Electrochemical impedance spectroscopy* vol. 48: Wiley-Interscience, 2008.

[158] X. Guo and R. Waser, "Electrical properties of the grain boundaries of oxygen ion conductors: Acceptor-doped zirconia and ceria," *Prog. Mater. Sci.,* vol. 51, no. 2, pp. 151-210, 2006.

[159] G. K. Singh, G. Ceder, and M. Z. Bazant, "Intercalation dynamics in rechargeable battery materials: General theory and phase-transformation waves in $LiFePO_4$," *Electrochim. Acta,* vol. 53, no. 26, pp. 7599-7613, 2008.

[160] S. Bhandaru, E. X. Zhang, D. M. Fleetwood, R. A. Reed, R. A. Weller, R. R. Harl, B. R. Rogers, and S. M. Weiss, "Accelerated oxidation of silicon due to X-ray irradiation," *IEEE Trans. Nucl. Sci.,* vol. 59, no. 4, pp. 781-785, 2012.

[161] A. Yariv, S. S. Orlov, and G. A. Rakuljic, "Holographic storage dynamics in lithium niobate: theory and experiment," *J. Opt. Soc. Am. B,* vol. 13, no. 11, pp. 2513-2523, 1996.

[162] X. Gu, J.-l. Liu, J.-h. Yang, H.-j. Xiang, X.-g. Gong, and Y.-y. Xia, "First-principles study of H^+ intercalation in layer-structured $LiCoO_2$," *J. Phys. Chem. C,* vol. 115, no. 25, pp. 12672-12676, 2011.

[163] S. M. Sze and K. K. Ng, *Physics of semiconductor devices*: Wiley-interscience, 2006.

[164] R. Courant, K. O. Friedrichs, and H. Lewy, "On the partial difference equations of mathematical physics," *IBM J. Res. Dev.,* vol. 11, no. 2, pp. 215-234, 1967.

[165] D. B. Strukov, J. L. Borghetti, and R. S. Williams, "Coupled ionic and electronic transport model of thin-film semiconductor memristive behavior," *small,* vol. 5, no. 9, pp. 1058-1063, 2009.

[166] D. B. Strukov and R. S. Williams, "Exponential ionic drift: fast switching and low volatility of thin-film memristors," *Appl. Phys. A,* vol. 94, no. 3, pp. 515-519, 2009.

[167] S. E. Savel'ev, A. S. Alexandrov, A. M. Bratkovsky, and R. S. Williams, "Molecular dynamics simulations of oxide memory resistors (memristors)," *Nanotechnology,* vol. 22, no. 25, p. 254011, 2011.

[168] S. E. Savel'ev, A. S. Alexandrov, A. M. Bratkovsky, and R. S. Williams, "Molecular dynamics simulations of oxide memristors: Crystal field effects," *Appl. Phys. Lett.,* vol. 99, no. 5, pp. 053108-3, 2011.

[169] D. Li, M. Li, F. Zahid, J. Wang, and H. Guo, "Oxygen vacancy filament formation in TiO_2: A kinetic Monte Carlo study," *J. Appl. Phys.,* vol. 112, no. 7, pp. 073512-7, 2012.

[170] D. Batas and H. Fiedler, "A Memristor SPICE Implementation and a New Approach for Magnetic Flux-Controlled Memristor Modeling," *IEEE Trans. Nanotechnol.,* vol. 10, no. 2, pp. 250-255, 2011.

[171] S. Benderli and T. A. Wey, "On SPICE macromodelling of TiO_2 memristors," *Electron. Lett.,* vol. 45, no. 7, pp. 377-379, 2009.

[172] Z. Biolek, D. Biolek, and V. Biolková, "SPICE model of memristor with nonlinear dopant drift," *Radioengineering,* vol. 18, no. 2, pp. 210-214, 2009.

[173] T. Prodromakis, B. P. Peh, C. Papavassiliou, and C. Toumazou, "A Versatile Memristor Model With Nonlinear Dopant Kinetics," *IEEE Trans. Electron Devices,* vol. 58, no. 9, pp. 3099-3105, 2011.

[174] A. Rak and G. Cserey, "Macromodeling of the Memristor in SPICE," *IEEE Trans. Comput. Aided Des. Integr. Circuits Syst.,* vol. 29, no. 4, pp. 632-636, 2010.

[175] C. Zamarreño-Ramos, L. A. Camuñas-Mesa, J. A. Perez-Carrasco, T. Masquelier, T. Serrano-Gotarredona, and B. Linares-Barranco, "On Spike-Timing-Dependent-Plasticity, Memristive Devices, and building a Self-Learning Visual Cortex," *Front. Neurosci.,* vol. 5, no. 26, pp. 1-22, 2011.

[176] W. Laws Calley, J. D. Greenlee, W. E. Henderson, J. Lowder, M. W. Moseley, W. Alan Doolittle, and P. G. Staib, "In situ Auger probe enabling epitaxy composition control of alloys by elemental surface analysis," *J. Vac. Sci. Technol. B,* vol. 31, no. 3, 2013.

Vita

Jordan Greenlee was born in Oak Ridge, Tennessee where he graduated from Oak Ridge High School. He attended the University of Arkansas, where he graduated Summa Cum Laude and received Bachelor's degrees in Electrical Engineering and Applied Mathematics in 2009. In 2011, he was awarded a Master's Degree in Electrical and Computer Engineering at the Georgia Institute of Technology in 2011. He plans to receive his Ph.D. in December of 2013 under the supervision of Dr. W. Alan Doolittle. During his PhD tenure, his principle interest has been the development of ionic-electronic devices through innovative growth, characterization, and modeling techniques.

Publications and Conference Proceedings

The following is a list of publications and presentations resulting from this work.

First Author Publications

[1] **J. D. Greenlee**, J. C. Shank, M. B. Tellekamp, J. Bi, D. M. Fleetwood, M. L. Alles, R. D. Schrimpf, and W. A. Doolittle, "Radiation Effects on $LiNbO_2$ Memristors for Neuromorphic Computing Applications," IEEE Trans. Nucl. Sci., vol. 60, no. 6, pp 1-8, 2013.

[2] **J. D. Greenlee**, J. C. Shank, M. B. Tellekamp, W. A. Doolittle, "Spatiotemporal drift-diffusion simulations of analog memristors," J. Appl. Phys., vol. 114, no. 4, pp. 034504 - 034504-9, 2013.

[3] **J. D. Greenlee**, C. F. Petersburg, W. G. Daly, F. M. Alamgir, W. A. Doolittle, "In-situ investigation of the channel conductance of a $Li_{1-x}CoO_2$ ($0 < x < 0.5$) ionic-electronic transistor," Appl. Phys. Lett., vol. 102, no. 21, pp. 213502 - 201502-4, 2013.

[4] **J. D. Greenlee**, W. L. Calley, M. W. Moseley, and W. A. Doolittle, "Comparison of Interfacial and Bulk Ionic Motion in Analog Memristors," IEEE Trans. Electron Dev., vol. 60, no. 1, pp 427-432, 2013.

[5] **J. D. Greenlee**, C. F. Petersburg, W. L. Calley, C. Jaye, D. A. Fischer, F. M. Alamgir, and W. A. Doolittle, "In-situ oxygen x-ray absorption spectroscopy investigation of the resistance modulation mechanism in $LiNbO_2$ memristors," Appl. Phys. Lett., vol. 100, no. 18, pp. 182106 - 182106-4, 2012

[6] **J. D. Greenlee**, W. L. Calley, W. Henderson, and W. A. Doolittle, "Halide based MBE of Crystalline Metals and Oxides," Phys. Status Solidi C, vol. 9, no. 2, pp. 155-160, 2011.

5.2.2 Contributing Author Publications

[1] J. C. Shank, **J. D. Greenlee**, M. B. Tellekamp, and W. A. Doolittle, "Volatile Memristors in Neuromorphic Spike-Frequency Adaptation Circuitry," IEEE Trans. Electron Dev., **submitted 10/16/2013**.

[2] W. L. Calley, **J. Greenlee** , W. E. Henderson , J. Lowder , M. W. Moseley , P. G. Staib , W. A. Doolittle, "In Situ Auger Probe Enabling Epitaxy Composition Control of Alloys," J. Vac. Sci. Technol., B., vol. 31, no. 3, pp. 03C126 - 03C126-5, 2013.

[3] M. Moseley, B. Gunning, **J. Greenlee**, J. Lowder, G. Namkoong, and W. Alan Doolittle, "Observation and control of the surface kinetics of InGaN for the elimination of phase separation," J. of Appl. Phys., vol. 112, no. 1, pp. 014909-014909-9, 2012.

5.2.3 First Author Presentations

[1] **J. D. Greenlee**, J. C. Shank, J. L. Compagnoni, B. Tellekamp, E. Zhang, J. Bi, M. L. Alles, R. D. Schrimpf, and W. A. Doolittle. "Radiation Effects on Lithium Metal Oxide Analog Memristors for Neuromorphic Computing," GOMACTech 13, Las Vegas, NV 2013.

[2] **J. D. Greenlee**, J. C. Shank, J. L. Compagnoni, B. Tellekamp, and W. A. Doolittle. "New Ways to Make a Synthetic Brain: Material Synthesis Pathways Toward Neuromorphic Computing," Workshop on Compound Semiconductor Materials and Devices, New Orleans, LA 2013.

[3] **J. D. Greenlee**, W. L. Calley, J. L. Compagnoni, J. C. Shank, and W. A. Doolittle. "MBE-Grown Analog Memristor Characterization by Electrochemical Impedance Spectroscopy," 29th North American Molecular Beam Epitaxy Conference, Atlanta, GA 2012.

[4] **J. D. Greenlee**, W. L. Calley, C. F. Petersburg, C. Jaye, D. A. Fischer, F. M. Alamgir, and W. A. Doolittle. "Advances in the Growth of Metal Oxides for Neuromorphic Computing Applications," AVS 58th International Symposium and Exhibition, Nashville, TN 2011.

[5] **J. D. Greenlee**, W. L. Calley, and W. A. Doolittle. "MBE Growth of Metal Oxides for Complementary Memristive Applications," 27th North American Molecular Beam Epitaxy Conference, Breckenridge, CO 2010.

5.2.4 Contributing Author Presentations

[1] W. L. Calley, P. Staib, W. Henderson, **J. Greenlee**, and W. A. Doolittle. "An In situ Auger Electron Analyzer System for Harsh Environment MBE," 29th North American Molecular Beam Epitaxy Conference, Atlanta, GA 2012.

[2] J.C. Shank, **J.D. Greenlee**, J.L. Compagnoni, and W.A. Doolittle. "Neuromorphic Computing Applications of $LiNbO_2$ Grown by Molecular Beam Epitaxy," 29th North American Molecular Beam Epitaxy Conference, Atlanta, GA 2012.

[3] J.L. Compagnoni, W. Laws Calley, **J.D. Greenlee**, J.C. Shank, and W.A. Doolittle. "Molecular Beam Epitaxy of Complex Transition-Metal Oxides by a Versatile Metal-Chloride Growth Chemistry," 29th North American Molecular Beam Epitaxy Conference, Atlanta, GA 2012.

[4] W. L. Calley, **J. D. Greenlee**, W. Henderson, W. A. Doolittle. "Halide Based MBE of Epitaxial Metals and Epitaxial Oxides," 38th International Symposium on Compound Semiconductors, Berlin, Germany 2011.

[5] W. L. Calley, P. Staib, J. Lowder, **J. D. Greenlee**, M. Moseley, W. E. Henderson, and W. A. Doolittle. "An Auger Electron Analyzer System for In situ MBE Growth Monitoring," AVS 58th International Symposium and Exhibition, Nashville, TN 2011.

[6] W. L. Calley, P. Staib, **J. D. Greenlee**, W. Henderson, and W. A. Doolittle. “An Auger Electron Analyzer System for In-situ MBE Stoichiometry Control,” 27th North American Molecular Beam Epitaxy Conference, Breckenridge, CO 2010.

[7] W. L. Calley, **J. D. Greenlee**, W. Henderson, and W. A. Doolittle. “Advances in Metal-Halide MBE Thin Film Growth,” 27th North American Molecular Beam Epitaxy Conference, Breckenridge, CO 2010.